High-Contrast Observations with an Integral Field Spectrograph

Neil Thomas Zimmerman

Submitted in partial fulfillment of the
requirements for the degree
of Doctor of Philosophy
in the Graduate School of Arts and Sciences

COLUMBIA UNIVERSITY

2011

This page intentionally left blank

ABSTRACT

High-Contrast Observations with an Integral Field Spectrograph

Neil Thomas Zimmerman

This thesis is comprised of work carried out during the commissioning phase of Project 1640, a combined coronagraph–integral field spectrograph for Palomar Observatory's adaptive optics-equipped 200" Hale Telescope. I have divided my investigations into three chapters. First, I describe the data reduction pipeline software, which solves a number of data extraction and calibration challenges unique to this kind of instrument. In the second chapter, I demonstrate a novel method for faint companion discovery which takes advantage of the high-precision relative astrometry enabled by a pupil plane reticle grid. This tool, in combination with the spectrophotometric capability of the integral field spectrograph, reveal that the A5V star Alcor has a heretofore unknown M-dwarf companion. In my third chapter, I explore the suitability of combining the non-redundant aperture mask interferometry technique with an integral field spectrograph. In the proof-of-concept observation of the spectroscopic binary star β CrB, I retrieve the first near-infrared spectrum of its F-dwarf companion.

This page intentionally left blank

Contents

This page intentionally left blank

List of Figures

List of Tables

This page intentionally left blank

ACKNOWLEDGMENTS

My parents Tom and Cathy, and my sister Erica all encouraged my fascination with astronomy from an early age, and gave me the love and support I needed to pursue this challenging career path.

I will always be grateful to Ben for the confidence he placed in me from the beginning, when I was still hanging on the edge of my seat for an acceptance letter. He trusted me to handle awesome responsibilities with nearly total independence. At the same time, from him I've learned how to carry out good science in technologically uncharted territories, how to lead a research collaboration spread out across a continent and abroad, all while having a fun life outside of work.

Throughout my time at the museum, I counted on Doug for a unique perspective on any problem. I will always admire his healthy disrespect for the "herd mentality" in both science and everyday life.

Anand has been an uncanny fountain of wisdom to me, on everything from Fourier optics to lentil recipes.

Sasha is the role model who showed me how to start from square one and break into this field. I'm grateful for all his generous advice along the way.

The faculty and staff of Columbia's astronomy department deserve much credit for creating an exceptional environment for grad students. Professors David Helfand, Jacqueline van Gorkom, David Schiminovich, and Jules Halpern each had tremendous impact on me as teachers and mentors during my early stages in the program. I also cannot forget

Millie Garcia, who I am indebted to for the numerous occasions she tenaciously sheltered me from the pitfalls of university bureaucracy.

Entering Columbia's astronomy department, I had no idea my classmates would become such a big part of my life. I will never forget the pleasure of working side-by-side with people who loved what they were doing so much, that after a week of research and coursework, chose to spend their Friday nights sharing the excitement of the universe with the public. I will also fondly recall the other good times we shared outside of work over the years: the house parties, the dome parties, the happy hours, etc.

The AMNH Astrophysics Department has also been a home of sorts over the last four years of my work. Of the many memorable people there, I must single out Gwendolyn King. Gwen worked tirelessly to smooth out adminstrative odds and edds. Thanks to her, I knew my paychecks would arrive on time, and I had no trouble participating in over a dozen observing runs and conference trips spread far and wide.

Over these years I've also had the companionship of such wonderful friends outside of astronomy. No one named, no one forgotten. Thanks to them, I made the most of living in this city, and kept the broader scope of the world in my sights.

This page intentionally left blank

This page intentionally left blank

Chapter 1

Introduction

Thanks to advances in numerous detection techniques, we are moving rapidly towards a census of the menagerie of worlds beyond the Solar System. Our current portrait of the exoplanet population already spans a wide range of physical properties. High-contrast imaging has a particularly crucial role to play in the expansion of exoplanet knowledge over the next decade. This approach will uniquely enable astronomers to build a large ensemble of detections of outer planets (at orbital separation 5 AU and greater), at the same time as probing their atmospheric composition. To reach this stage, integral field spectroscopy techniques must be adapted to extreme specifications in angular resolution and contrast.

Figure 1.1 illustrates the distinct regions of exoplanet parameter space available to several different survey methods, plotted in terms of mass and orbital separation.

Before concentrating on the method that is the subject of this thesis, it is worthwhile to briefly examine the handful of other exoplanet discovery methods which have earned the greatest share of support from the astronomical community. To show how they fit

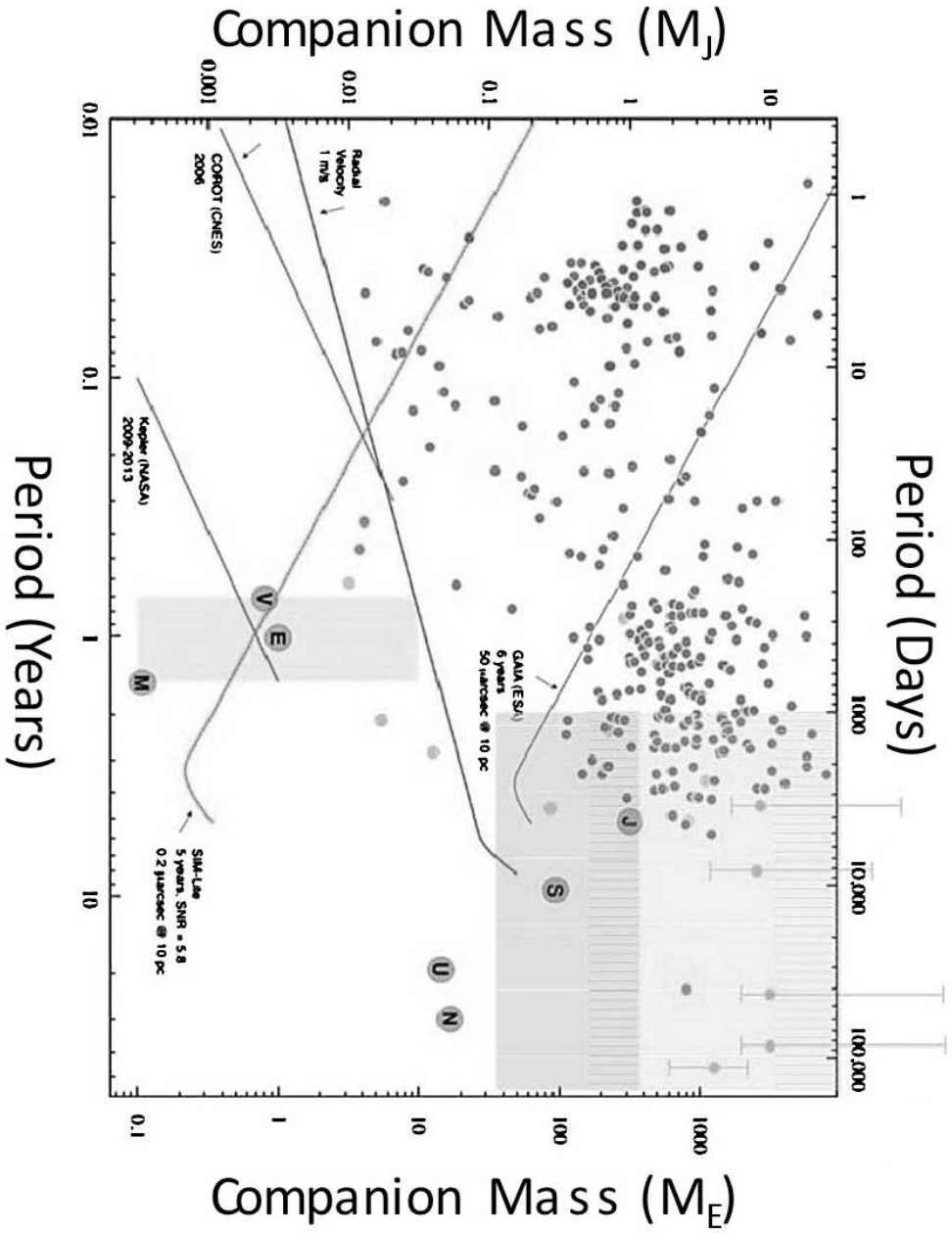

Figure 1.1 The known population of exoplanets plotted alongside the sensitivity envelopes of several detection techniques, reproduced from Beichman et al. (2010). Sensitivity curves are plotted for ground-based radial velocity surveys; Corot and Kepler (transit missions); Gaia and SIM (space astrometry missions, the latter canceled). The shaded region in the upper right corner highlights the discovery space of ground-based high-contrast imaging in the next decade, with the darker extension below representing *JWST*'s estimated range of sensitivity.

into the broader picture of the comparative exoplanetary science field, we summarize their strengths, weaknesses, achievements to date, and future prospects. Scharf (2009) gives an excellent review of some of the technical principles behind these methods, which we merely allude to here.

We also note that in our discussion here of exoplanets, we implicitly include substellar companions extending into the brown dwarf mass regime (by convention established by Oppenheimer et al. (2000), the lower mass limit of Deuterium burning, typically 13 M_J). One reason for this is the strong body of theoretical evidence suggesting that the formation mechanisms of brown dwarf companions are closely linked to that of giant planets (e.g., Stamatellos et al. 2007; Thies et al. 2010). Furthermore, the Deuterium burning process which separates brown dwarfs from planets is not a simple transition fixed for all conditions. For example, a body as small as 11.3 M_J will eventually burn 10% of its Deuterium, provided its helium fraction is as high as 0.32 (Spiegel et al. 2011). Our understanding of the internal physics of these bodies is modest, and it is very challenging to disentangle the effects of mass, metallicity, and age in observational data. Therefore, it is wisest to consider all sub-stellar companions over one continuous space of physical parameters, rather than allowing terminology restrict us.

1.1 Indirect Exoplanet Detection Methods

Of all the exoplanet detection methods, gravitational microlenses probe the widest range of masses and orbital separations. This is due to the extreme sensitivity of the lensed light curve to properties of the mass distribution of the the lensing bodies—in this case,

the planetary system itself (Gould & Loeb 1992). However, the very low probability of seeing a microlens event for a given star means that detections tend to occur for stars at prohibitively large distances for any kind of follow-up observations (to date, the shortest published distance estimate to a microlens exoplanet is 1.5 kpc; Gaudi 2010). Because of this, the strategy of these planet hunters has been to carry out wide-field surveys for microlens events, each intensively followed up by multiple optical telescopes to piece together as much continuous time coverage as possible over their duration (on the order of days; Udalski 2003). Microlensing surveys are not confined to studying objects gravitationally bound to stars: recently, results from a two-year campaign revealed that "free-floating" planetary mass objects are probably more common than main-sequence stars in the Milky Way (Sumi et al. 2011).

While the precisions of the inferred mass and orbital separation of an individual planet are usually low, microlens surveys are steadily accumulating statistical constraints on planetary system architectures. There is little doubt that the large accessible distance scales will enable gravitational microlens studies to lead our understanding of how planet properties vary for different stellar populations within the Milky Way, and even beyond. If the recommendations of the National Academy of Sciences Astro2010 Committee are followed, NASA's next flagship astrophysics mission will be a wide-field near-infrared observatory partially dedicated to surveying the galactic bulge for exoplanet signatures in microlens events (Blandford 2010).

The transit technique also has a relatively low detection probability per star. Again, as in the case of microlenses, the low per-star event rate can be beaten through large-area

sky surveys. Exoplanet transit studies have entered a true golden age since the Kepler spacecraft launched in 2009, due to the awesome precision of its differential photometry (40 ppm median precision; Caldwell et al. (2010)). The first four months of data alone contain 1235 planetary-like transit signatures (Borucki et al. 2011). However, picking out the transit signal from long term systematic photometric noise is just the start of the challenges for this detection technique: the path from candidate to confirmed planet is not a simple one. Dedicated follow-up observations for each candidate are necessary to eliminate false alarms, which can result from a number of bedeviling configurations, such as grazing eclipses by stellar companions, and background eclipsing binary stars in the line of sight of the candidate host star. In addition, the transiting planet's mass can only be determined in fortuitous circumstances, such as when a radial velocity signal is detectable, or when there are measurable perturbations in transit timing caused by additional planets in the same system (Holman et al. 2010; Nesvorný & Morbidelli 2008). The happy upshot of those cases, however, is the constraint on planet density that comes along with knowledge of both mass and transit depth (ergo radius).

Since the likelihood of catching a transit for a given star-planet pair is inversely proportional to the orbital separation, transit detections are heavily biased towards close-in planets. Therefore, it is unsurprising that all exoplanets discovered so far through transits have semi-major axes below 0.5 AU. Nevertheless, important conclusions have been drawn about this part of the exoplanet population from Kepler data: the planet size distribution peaks around 2–3 $R_\oplus$, and multiple-planet systems are common, making up at least 17% of candidate planet systems. When overall geometric biases have been taken into account, the

Kepler team estimates planet occurrence frequencies of 19% for Neptune-sized planets (2–6 $R_\oplus$) and 7% for super-Earth sized planets within an orbital separation of 0.5 AU(1.25–2 $R_\oplus$; Borucki et al. 2011).

Ground-based transit surveys, including TreS, WASP, and HATNet, have also made major contributions to exoplanet discoveries (Alonso et al. 2004; Collier Cameron et al. 2009; Bakos et al. 2009). By monitoring bright stars with relatively small telescopes, they tend to discover massive "hot Jupiters" which are often amenable to follow-up and individual study. In some cases, this has involved spectroscopic studies of the transmission of the host star's light through the planet atmospheres, or the thermal emission from the planet itself. HD 209458 b is one of the classic examples of exoplanets for which both of those kinds of measurements have been possible (Charbonneau et al. 2002; Knutson et al. 2008). Emission spectroscopy is also possible with these "hot Jupiters": HD 189733 b is the first exoplanet shown to possess Methane, based on the near-infrared spectrum acquired with the Hubble Space Telescope (Swain et al. 2008). In this way, the first investigations on the dynamics and chemical compositions of exoplanet atmospheres have begun, although restricted to a sample with very small orbital radii and high temperature.

Until the Kepler mission began releasing data, the vast majority of exoplanet candidates were discovered through yet another indirect technique: radial velocity. As of the time of writing, this category has just reached a tally of 500. High-precision Doppler shift instrumentation has paved the way for this flood of exoplanet discoveries (e.g., Pepe et al. 2002). Spectrographs designed for planet hunting such as HIRES and HARPS routinely reach internal Doppler shift precision near 1 m/s, bringing super-Earth-mass planets within

reach (Vogt et al. 2010). Crucially, the most sensitive radial velocity results confirm the rise in the planet occurrence with *decreasing* mass from 1 M_J towards $\sim 2M_\oplus$ that the Kepler team uncovered (Howard et al. 2010).

Since radial velocity surveys operate by accumulating data over long time baselines, they are also gradually expanding their discovery envelope into greater orbital separations. Within the last year, six new radial velocity exoplanet candidates have been announced with semi-major axis beyond 5 AU (e.g., HD 99492 c by Meschiari et al. 2011). To the extent to which radial velocity surveys are complete in orbital period, they find that planet frequency increases with distance from the host star, and furthermore that more massive planets exist at greater separations. Finally, another surprise, uncovered by radial velocity surveys is the broad distribution of eccentricities of long-period exoplanets. The eccentricity distribution is populated all the way up to unity, and is strikingly similar to that of binary stars (Udry & Santos 2007). However, one has to keep in mind that radial velocity signals only indicate *minimum* mass, and so all of these derived relationships rest on statistical arguments. As a cautionary tale, Santos et al. (2010) reported a radial velocity planet candidate with minimum mass 1.96 M_J orbiting HD 5833. By analyzing the Hipparcos satellite astrometry data on this star, Sahlmann et al. (2011) determined that this radial velocity signal was actually due to a 69 M_J brown dwarf at an orbital inclination of 178°. Orthogonal observation techniques are required to constrain the inclination angle of the orbit and therefore the true mass of radial velocity candidates.

One of the main limitations of radial velocity is noise from the target stars themselves. Acoustic oscillations and spot activity conspire to add jitter to radial velocity measure-

ments (Saar & Donahue 1997). Such contamination is particularly problematic for young stars, other rapidly rotating stars, and evolved stars (Huerta et al. 2008; Prato et al. 2008). Even for relatively quiet main-sequence stars, the lack of long-term stability in Doppler measurements prevents surveys from detecting low-mass, long-period planets. To what extent this barrier can be overcome, through complementing Doppler measurements with careful monitoring of target star activity, remains to be seen. Even if the confusion from stellar activity is counteracted, however, the length of time required to monitor the star before a detection emerges would still scale with the orbital period. As a result, radial velocity is an inherently inefficient method to search for long-period planets of any mass.

Similar to the way that stars reveal planetary mass companions through the Doppler shift of their photospheric emission, pulsars too can broadcast the existence of unseen companions, through the timing of their radio pulses. In fact, Wolszczan & Frail (1992) made the first secure discovery of an exoplanet–a system of two planets, no less, both confined to orbits within 0.5 AU—based on analyzing the millisecond-scale perturbations in radio pulse arrivals from PSR B1257+12. The exquisite sensitivity of the pulse period variation to orbital motion soon enabled Wolszczan to uncover a third planet of mass lower limit 0.015 $M_{\oplus}$, comparable to the mass of Earth's moon (Wolszczan 1994). A number of theoretical models for the origins of the pulsar planets have been investigated, with results favoring formation in a disk of matter accreted by the neutron star (Podsiadlowski 1993; Phinney & Hansen 1993). There remains no clear consensus on the exact physical mechanism, however (Hansen et al. 2009). In any case, the unexpected discovery of the pulsar planets dramatically underscored the immense range of environments that exoplanets can

occupy.

The last indirect detection method we describe, astrometry, is one of the oldest of all in astronomy. Yet, ironically, it has been the slowest of all mentioned so far to mature in the exoplanet field. This is due to the extremely small reflex amplitude generated by a planet, in conjunction with the turbulent atmosphere spoiling the angular resolution of telescopes at optical wavelengths. However, developments in long baseline optical interferometry instrumentation (Shao & Colavita 1992) have recently brought differential astrometry precision into the regime of exoplanet sensitivity (< 50 μas at the Palomar Testbed Interferometer as reported by Muterspaugh et al. (2006)). The VLTI PRIMA (Phase-Referenced Imaging and Micro-arcsecond Astrometry) project is one of the new facilities expected to make major contributions in this area, surveying bright nearby stars from the Southern hemisphere (Launhardt et al. 2008).

Farther along into the future, space missions with astrometry capability, unhindered by the atmosphere, will uncover avalanches of planets in the solar neighborhood. ESA's Gaia satellite will survey the full sky and record 8 μas-precision astrometric tracks for all stars with magnitude $6 < V < 13$ (Lindegren 2010). Such measurements are sufficient to detect the reflex motion of G-type stars hosting giant planets of order 2-3 M_J within 50 pc. However, although the Gaia satellite will be launched in 2013, the astrometric results will not be fully processed and released until three years past the end of science operations, after 2020.

Astrometry is biased in a manner similar to radial velocity, towards large, short-period planets. To detect planets with wide separation requires monitoring on a time scale com-

parable to the orbit period, and consequently a strong handle on long-term systematic error sources. Stellar activity is also a concern, though much less so than in the case of radial velocity (Makarov et al. 2009). Therefore, astrometry surveys can more evenly sample host stars across age and spectral type than radial velocity surveys can, constraining models describing how young planetary systems evolve from the time of formation.

1.2 High-Contrast Imaging

High-contrast imaging differs from all the above approaches in that it is a *direct* detection technique. Rather than inferring the presence of the planet from the properties of the host star's light (or in the case of gravitational microlens, usually a background star), high-contrast imaging seeks to isolate the light either reflecting off of or emitted by the planet. The technical challenges to accomplishing this are tremendous. As in the case of astrometry, the angular resolution requirement puts ground-based efforts at the mercy of the atmosphere. The extreme contrast between the star and the planet compounds this difficulty, since the atmosphere degrades the the star's image so that its light is spread over the very region where one would search for an exoplanet point sources. Even from space, where the stellar image formed by a telescope approaches the theoretical limits of sharpness and stability, potential planet signals are overwhelmed by the structure in the diffraction pattern. The reflected light from a Jupiter analog around a solar twin, for example, is a factor of 10^8 dimmer than the star at near-infrared wavelengths. Therefore, the residual starlight at the planet's separation must be suppressed below this level in order to detect it and measure its spectrum (Oppenheimer & Hinkley 2009).

Before forging ahead into such a challenging, and expensive observational problem, we need to justify the efforts on scientific grounds. The case is straightforward: high-contrast imaging is the only exoplanet detection approach that can efficiently detect outer planets (beyond ~ 5 AU) without many years of repeat observations of the star's position or Doppler shift. It is also the only method which allows us to isolate the spectrum of a long-period planet, to investigate its composition. Eventually, with further technology development, high-contrast imaging will enable spectroscopy of terrestrial exoplanet atmospheres, setting the stage for astrobiological investigations to answer profound questions about Earth's place in the universe.

Wave front control is the most important aspect of high-contrast instrumentation. Advanced adaptive optics systems, by compensating for most of the distortions introduced by the atmosphere, concentrate a target star's light from the fuzzy seeing-limited disk into a tight point spread function (PSF) resembling the ideal diffraction-limited telescope response (Hardy 1978). Once the starlight has been corrected to a sharp (high Strehl-ratio) PSF, it then becomes feasible to subtract almost all of it from the image. This is the function of a stellar coronagraph, a train of masks that operate on the light exiting a telescope, before the image is brought to a final focus.

In the regime of high wave front correction (< 200 nm root-mean-square residual wave front error) that is achieved by the adaptive optics systems of a few observatories around the world, a modified version of the classical Lyot coronagraph (Lyot 1939) has been shown to be an effective design for removing the core of the star's PSF and attenuating its extended diffraction structure (Sivaramakrishnan et al. 2001). A diagram of this concept,

illustrated for the case of an ideal wave front and a telescope with no secondary obstruction, is shown in Figure 1.2. The first mask, in the focal plane, is of width several diffraction widths. In the following pupil plane, whatever energy was not occulted by the focal plane mask is localized near the pupil boundary. Therefore, a second mask blocking a ring around the perimeter of the pupil functions to attenuate the PSF at locations outside the original occulting spot in the final image. Further improvement to the overall contrast is realized by smoothing hard edges in the pupil with an apodizing mask (not shown) (Soummer 2005).

The Lyot coronagraph is only one among many coronagraph designs (for a recent review, see Guyon 2009). However, it has several advantageous over its cousins: the concept is the most thoroughly proven on real telescopes, and the cost of implementation is relatively low, since it does not demand exceptional procedures in optical fabrication or alignment. Outside of the family of conventional coronagraph designs, there also exist interferometric *nulling* techniques to cancel the light of a star (e.g., Angel & Woolf 1997; Hinz et al. 1998). However, their more stringent wave front requirements preclude the possibility of ground-based implementations (the Keck Interferometer, for example; Colavita et al. 1998, 2009) from delivering starlight suppression on par with Lyot coronagraphs. Yet, future space-based missions may take advantage of an interferometric nulling concept to characterize terrestrial exoplanets (e.g. Léger et al. 1996; Angel & Woolf 1997; Wallace et al. 2000; Lawson et al. 2007; Lyon et al. 2010).

The efficacy of combining adaptive optics (AO) with a coronagraph to reach a high dynamic range was demonstrated by the first discovery of a brown dwarf, Gliese 229B, using the 60-inch (1.5 m) telescope at Palomar Observatory (Nakajima et al. 1995; Oppen-

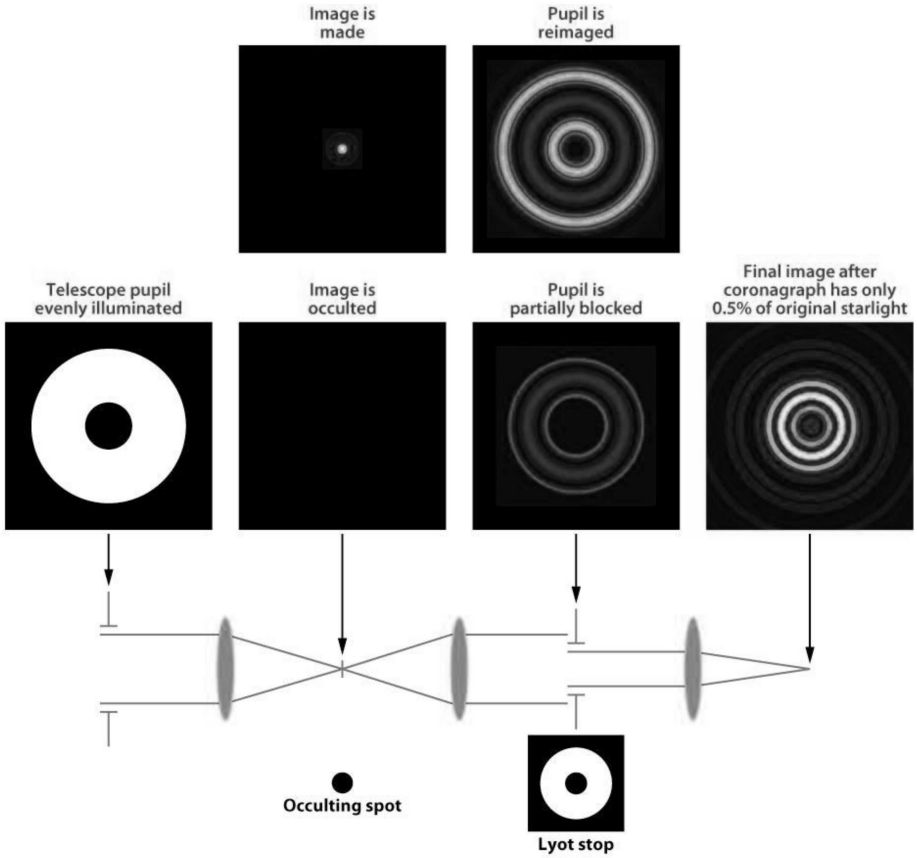

Figure 1.2 Diagram of the concept of a Lyot coronagraph for stellar occultation, reproduced from Oppenheimer & Hinkley (2009). The occulting spot, in the focal plane, occults the core of the target star PSF. In the re-imaged pupil plane, light from the spatially extended diffraction rings of the PSF is concentrated near the perimeter of the pupil. By adding a "Lyot stop" in this pupil plane, the diffraction rings are attenuated in the final image, thus boosting the overall dynamic range.

heimer et al. 1995). The contrast and separation regime this object occupied, $\sim 10^5$ at $8''$ separation, was beyond the reach of conventional ground-based telescope imaging. At the 5.7 pc distance of the Gliese 229 system, this angular separation corresponds to a projected physical distance of 46 AU, comparable to the scale of the orbits of the outermost planets in the Solar System (the semi-major axis of Neptune's orbit is 30 AU). Therefore, to probe stellar environments within the scale of the Solar System—even for the closest stars

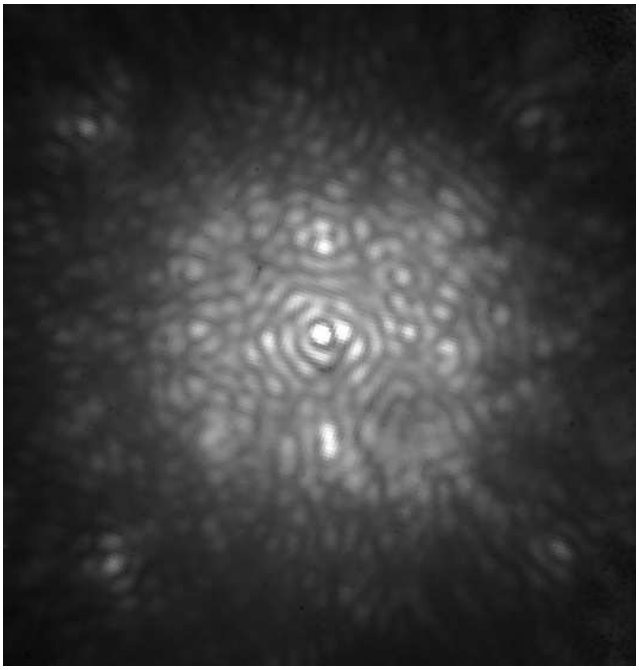

Figure 1.3 Image of a coronagraphically occulted star by Project 1640. In this regime of adaptive optics correction, the dominant remaining starlight contamination appears in the form of speckles, point source-like artifacts due to wave front errors originating inside the telescope and instrument optics.

in the solar neighborhood—requires us to peer yet closer to the star, where reaching 10^5 and higher dynamic range is ever more challenging. To reach a dynamic range of 10^6, for example, the residual wave front error of the AO coronagraph must be on the order of 20 nm in the H band, as compared to the $\sim$200 nm RMS error that is routinely achieved with several current AO systems in the near-infrared (Stapelfeldt 2006).

At angular separations of several tens of diffraction widths from the target star, inside the *control radius* (Oppenheimer et al. 2003) provided by the adaptive optics system, the residual starlight limiting the dynamic range takes on the form of *speckles* (see the image in Figure 1.3 for an example; for an early description of the phenomenon see Racine et al. (1999)). Speckles originate from aberrations in the wave front beyond the control of the

adaptive optics system, either because the errors are below the sensitivity of the wave front sensor, or because they originate downstream of the AO system. In practice, when AO performance is excellent, it is the latter that dominate. Since these are aberrations caused by minute imperfections on optical surfaces, such speckles are long-lived *quasi-static* artifacts which evolve slowly and do not average out over long exposures like photon noise (Marois et al. 2005; Hinkley et al. 2007).

There are a few ways to surmount the speckle barrier. One is angular differential imaging, which takes advantage of the fact that the quasi-static speckle pattern is fixed with respect to the optics rather than the light source. By combining many images where the sky is rotated at different angles with respect to the camera, the speckles can be partially eliminated by a form of PSF subtraction (Marois et al. 2006a). This method was in fact used to achieve one of the first direct images of an exoplanet system, discovering three young, self-luminous giant planets orbiting HR 8799 (Marois et al. 2008a). One of the limitations to angular differential imaging, however, is the fact that the images must be acquired over a long enough time interval for significant sky rotation (in the case of an alt-azimuth telescope). Therefore, the effectiveness of the subtraction is limited by the subtle evolution of the speckle pattern over the course of the exposures.

Another method of reducing the influence of speckles is to take advantage of their chromatic properties (Racine et al. 1999; Sparks & Ford 2002). To first order, speckles scale radially from the target star, by an angle proportional to wavelength. This chromatic speckle expansion may be understood in the framework of Fraunhofer diffraction, in which the image intensity is the square of the Fourier transform of the complex telescope

pupil amplitude function (Goodman 1996). The solution of the Fraunhofer integral scales linearly in the spatial dimensions with wavelength. Consider a case where the pupil amplitude function, including an on-axis plane wave and the speckle-generating aberrations, is constant for all wavelengths. The telescope image, including the speckles caused by the aberrations, will appear identical across those wavelengths, apart from a spatial scale factor. A true off-axis point source, on the other hand, cannot result in a pupil with fixed complex amplitude over wavelength. That is because the plane wave from the off-axis point source introduces a wavelength-dependent slope in the phase of the pupil. This phase slope perfectly cancels the chromatic scaling that the rest of the image experiences, and so the off-axis point source remains fixed in the image.

Therefore, if an instrument behind an AO coronagraph can record simultaneous images over roughly an octave of wavelengths, it is then possible to discriminate speckles from true astrophysical sources. The implementation again comes down to a form of PSF subtraction, but beforehand scaling the different wavelength images appropriately. In practice, this is complicated by deviations from linear scaling, and the variations in the relative amplitudes of the speckles across wavelength. Nonetheless, it has been demonstrated with real data to offer over a factor of ten improvement in dynamic range (Crepp et al. 2011). On top of this, there is the tremendous scientific benefit of acquiring the spectrum of the planet, once detected (Pueyo 2011).

Project 1640 (P1640), the instrument used for all observations in this thesis, is the first instrument to implement the chromatic approach to high-contrast imaging (Hinkley et al. 2011a). The wavelength diversity is introduced by an integral field spectrograph, shown in

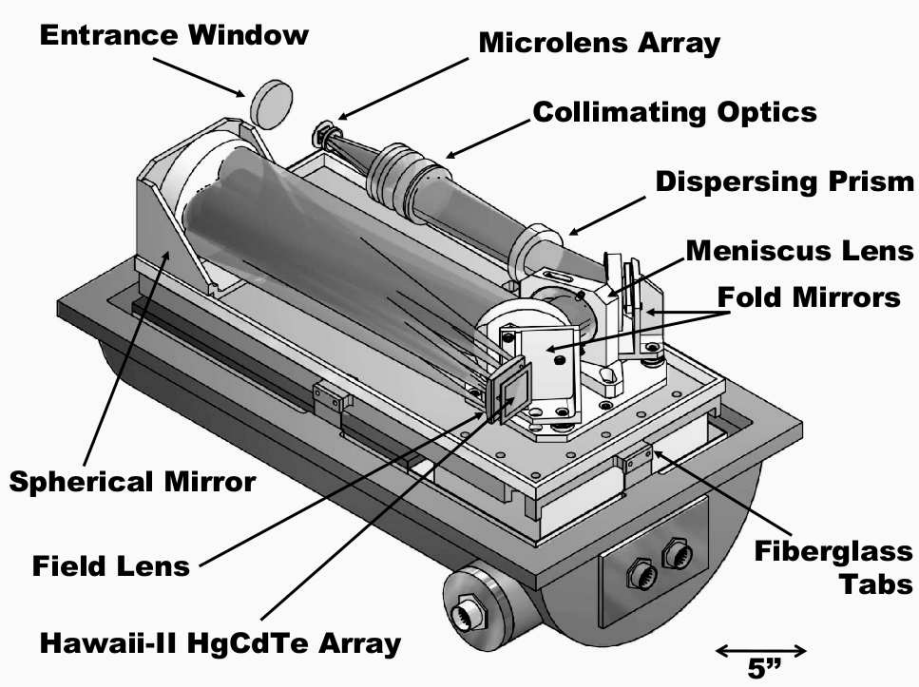

Figure 1.4 Diagram of the Project 1640 Integral Field Spectrograph, reproduced from Hinkley et al. (2011a). The coronagraphically-occulted image is formed on the microlens array. Each microlens separates the light from a small spatial element of the field of view, which is then collimated and dispersed by a prism. The resulting spectrum is focused on a near-infrared detector array.

Figure 1.4. Although integral field spectrographs have been used in astronomy for decades, P1640 operates in a unique regime of spatial and spectral resolution optimized for its purpose. It uses a microlens array to break the image up into optically isolated spatial elements. A prism disperses the light from each microlens, forming spectra which are focused on a near-infrared detector. The integral field spectrograph was designed to match an apodized Lyot coronagraph situated behind the 200-inch Hale Telescope's PALAO system (Dekany et al. 1997). We note that two other high-contrast instruments with similar design to P1640 will begin operation in the next year: Gemini Planet Imager (Macintosh et al. 2008), and Spectro-Polarimetric High contrast Exoplanet REsearch (SPHERE) project (Beuzit et al.

2008).

In the next chapter, we explore the methods needed to treat the data produced by the integral field spectrograph. Before speckle suppression can work, it is necessary to extract a data cube from each spectrograph focal plane. The spectrum produced for each spatial element is coarsely-sampled, and confined to a tiny fraction of the detector area, so that even small distortions in the geometric pattern of the focal plane will corrupt the data extraction unless those effects are accounted for. The solution comes down to building an accurate empirical model of the response of the spectrograph, taking into account long-term systematic effects.

The third chapter of the thesis answers the question: when a new source shows up in a high-contrast image, what should we do next? Two stars in the same line of sight may not be physically related. We must demonstrate through astrometric analysis of at least two epochs of data that the source is gravitationally bound to the star, and not merely a background star. This chapter also shows how the low-resolution spectrum from an integral field spectrograph like P1640 can be used to characterize faint companions.

The final chapter explores an alternative, non-coronagraph high-contrast operating mode for an integral field spectrograph behind an AO system: non-redundant aperture mask (NRM) interferometry. The main advantage of NRM interferometry is the that the inner working angle is the same as that of a Michelson interferometer, $\lambda/(2D)$, if D is telescope aperture versus $5\lambda/(2D)$ for coronagraphs optimized for high contrast work. This allows NRM observations to complement the physical scales probed by coronagraph images. As we show in this chapter, by adding the wavelength dimension of an integral field spectro-

graph to NRM interferometry, it is also possible to retrieve accurate low resolution spectra at these close angular separations.

Chapter 2

A Data-Cube Extraction Pipeline for a Coronagraphic Integral Field Spectrograph[†]

Neil Zimmerman, Douglas Brenner, Ben R. Oppenheimer, Ian R. Parry, Sasha Hinkley,

Stephanie Hunt & Robin Roberts

ABSTRACT

Project 1640 is a high-contrast near-infrared instrument probing the vicinities of nearby stars through the unique combination of an integral field spectrograph with a Lyot coronagraph and a high-order adaptive optics system. The extraordinary data-reduction demands, similar to those that several new exoplanet imaging instruments will face in the near future,

[†]Published in PASP, Vol. 123, Issue 904, pp. 746-763 (2011)

have been met by the novel software algorithms described herein. The Project 1640 Data Cube Extraction Pipeline (PCXP) automates the translation of 3.8×10^4 closely packed, coarsely sampled spectra to a data cube. We implement a robust empirical model of the spectrograph focal-plane geometry to register the detector image at subpixel precision, and we map the cube extraction. We demonstrate our ability to accurately retrieve source spectra based on an observation of Saturns moon Titan.

2.1 Introduction

In recent years an assortment of new astronomical techniques have evolved to address the challenges of imaging faint objects and disk structure at close angular separations to nearby stars. A major scientific motivation for these efforts is the direct detection and characterization of low-mass companion bodies orbiting at separations between ~ 5 and 100 AU. These objects are beyond the reach of conventional optical imaging due to the extreme contrast in brightness with respect to the primary star. In such cases, even under ideal observing conditions the diffracted light of the primary star overwhelms the neighboring source of interest. The various methods of manipulating a star's light to enable investigation of its immediate environment are collectively referred to as high-contrast imaging. For a recent review of this field, see Oppenheimer & Hinkley (2009). The acquisition of spectra of young, sub-stellar mass objects in this newly opened parameter space will ultimately lead to a breakthrough in our understanding of exoplanet populations (Beichman et al. 2010).

Project 1640 (P1640) is the first of several instruments to approach the high contrast imaging problem through a combination of high-order adaptive optics, a Lyot coronagraph,

and an integral field spectrograph (Hinkley et al. 2011b). Forthcoming instruments using a similar design include the Gemini Planet Imager (GPI) (Macintosh et al. 2006), the Very Large Telescope Spectro-Polarimetric High-contrast Exoplanet REsearch (VLT-SPHERE) project (Beuzit et al. 2008), and the Subaru Telescope Planetary Origins Imaging Spectrograph (POISE) (McElwain 2008). While previous efforts have used integral field spectrographs for high contrast imaging (e.g. Thatte et al. 2007; McElwain et al. 2007; Janson et al. 2008), and Lyot coronagraphs have also been employed for surveys of nearby stars (e.g. Chauvin et al. 2010a; Leconte et al. 2010), P1640 is the first instrument to combine these two technologies. The coronagraph component, based on the Fourier optics concept described in Sivaramakrishnan et al. (2001), rejects the core of the target star's point spread function (PSF) and attenuates the surrounding diffraction rings. Provided that the adaptive optics (AO) system upstream of the coronagraph has corrected the star's PSF to near the diffraction limit, then the dominant source of noise in the image exiting the coronagraph takes the form of a halo of speckles surrounding the occulted star, as in Figure 2.1 (Racine et al. 1999; Perrin et al. 2003). These relatively long-lived, point source-like artifacts are caused by uncorrected wave front aberrations, and limit the dynamic range of the data unless further processing is carried out (Hinkley et al. 2007).

The integral field spectrograph, also referred to as the integral field unit (IFU), is situated after the coronagraph and provides spatially resolved spectra for a grid of points across the field of view (Bacon et al. 1988). The reduced form of data acquired with an IFU is a stack of simultaneous narrowband images spanning the instrument's wavelength range, often called a data cube. An example of part of a P1640 data cube is shown in

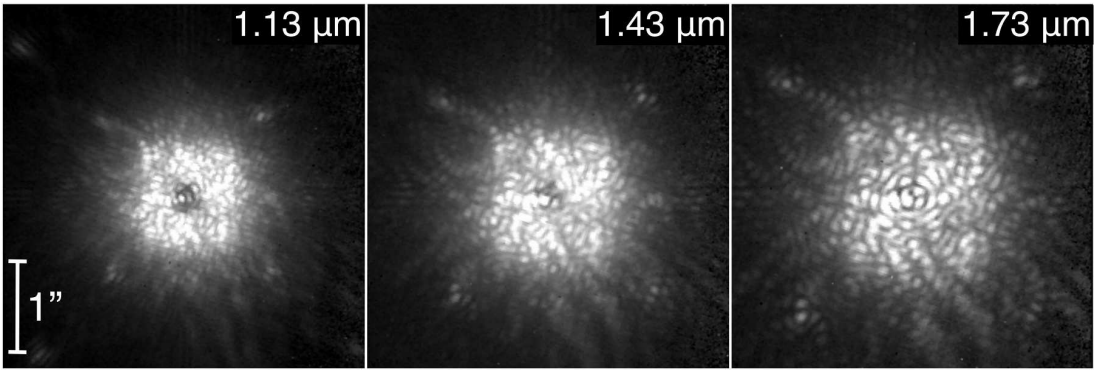

Figure 2.1 Three of the 23 channels making up an example P1640 data cube, formed from a 154 s exposure of the coronagraphically occulted star HD 27946 (V = 5.3). The three channel images shown here, each consisting of 200 $\times$ 200 *spaxels*, are displayed with a square root stretch. A halo of well-defined speckles surround the focal plane mask, expanding with wavelength. The cube configuration of the data enables post-processing algorithms to take advantage of the chromaticity of speckles to reduce their influence on detection limits.

Figure 2.1. One benefit the IFU provides is enabling the observer to measure the spectrum of any source at any position in the field of view. This is not possible with a conventional spectrograph, which can only use one spatial dimension at a time to discriminate against other sources in the field of view. The second purpose of the IFU is to exploit the chromatic behavior of the speckles (Sparks & Ford 2002). Speckles are optical in origin and their separation from the target star is linearly proportional to wavelength, at least to a first-order approximation (see Figure 2.1). By comparing the images in different channels of the data cube, the observer can discriminate the speckles from a true point source, whose position should remain constant with wavelength. Furthermore, automated post-processing software can use the chromaticity of the speckles to subtract a large component of them from the data, taking a reduced data cube as input and generating a speckle-suppressed version (Crepp et al. 2011; Pueyo 2011).

The complex properties of data generated by the P1640 IFU necessitate novel reduc-

tion techniques to reach the point where inspection, spectrophotometry, astrometry, and advanced post-processing techniques like speckle suppression can begin. In the scope of this article, we describe the software created to translate rapidly the raw data from the IFU camera to a set of data cubes ready for further analysis.

2.2 Project 1640 Design and Data Acquisition

During operation at Palomar Observatory, P1640 receives a wave front-corrected beam of the target star's light from the 200" Hale Telescope AO system. The current AO system, the 241-actuator PALAO (Dekany et al. 1997), will soon be upgraded to the 3388-actuator PALM-3000 (Bouchez et al. 2009). Upon entering the instrument, the light passes through an apodized Lyot coronagraph, followed by an integral field spectrograph, which contains a near-infrared camera.

In addition to the focal plane mask and Lyot stop of a traditional Lyot coronagraph, P1640 uses a pupil plane apodization mask to optimize the starlight suppression based on the telescope pupil shape (Soummer 2005). The beam exiting the coronagraph comes to a focus on a 200×200 square microlens array at the entrance of the spectrograph. Immediately after the microlens array, the light is collimated to form a pupil on a wedge-shaped prism, which disperses the light over the 1.1-1.8 μm wavelength range of operation spanning the J and H bands. Additional optics focus the 4×10^4 resulting spectra onto a Teledyne HAWAII-2 2048×2048 pixel, HgCdTe, near-infrared detector. The field of view of the final image, designed to match the control radius of the PALM-3000 AO system, is $4'' \times 4''$. For further details on the optical and mechanical design, see Hinkley et al. (2011b).

For each exposure, the camera controller performs a sequence of non-destructive reads on the detector array. In other words, the digitized value of each pixel is periodically sampled while its voltage escalates. This technique, known as up-the-ramp sampling, can result in the read noise being reduced by a factor of $\sqrt{N/12}$ in a reduced image when the counts versus read slope is fit for the N samples of each pixel (Offenberg et al. 2001). Up-the-ramp sampling also adds an advantageous temporal dimension to our data. Speckle suppression algorithms work best when the positions of the speckles are well-defined. For bright stars with high signal-to-noise in individual read differences, it may be helpful to "freeze" the speckle pattern with the higher time resolution enabled in a read-by-read data reduction. Our pipeline reduces the detector data with both approaches: the non-destructive read (NDR) slope fit and consecutive read differences.

The read sample interval is fixed at 7.7 seconds by the camera controller. The sequence of reads are stored in a binary file containing the arrays of 16-bit unsigned integer samples, which we refer to as a *dat* file. The camera controller also generates a separate FITS file with a header containing the information about the telescope and instrument status, the target (coordinates, magnitude, parallax, etc.), and the name of the *dat* file corresponding to the exposure. A typical observation of a Project 1640 science target is made up of 15 exposures, each containing 20 reads, giving a cumulative exposure time of 38.6 minutes. The resulting volume of raw data is 160 Mbytes for each exposure's *dat* file and 2.4 Gbytes in total.

The structure of the P1640 IFU focal plane, illuminated by Moonlight, is depicted in Figure 2.2. The microlens array, represented by the dotted grid superimposed on the left

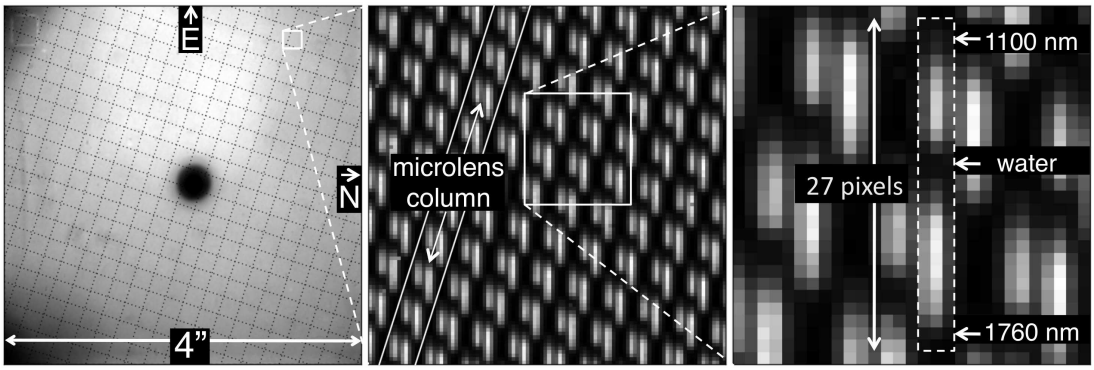

Figure 2.2 A hierarchical diagram of the P1640 integral field spectrograph focal plane. **Left**: an average of ten calibration Moon exposures, recorded by the near-infrared detector at the spectrograph focal plane. The projection of the IFU microlens array onto the detector is represented by a superimposed dotted grid, with each gap spanning ten microlenses. **Middle**: expanding a 100×100 pixel section reveals the underlying pattern of microlens spectra. The tilt of the square microlens array with respect to the detector (-18.5°) interleaves the adjacent rows of spectra for an efficient use of detector area. **Right**: each spectrum, spanning *J* and *H* band (1.1 μm to 1.8 μm), displays the prominent telluric water absorption trough centered near 1.4 μm.

panel, is rotated with respect to the detector. This configuration interleaves the adjacent rows of microlens spectra, thereby maximizing the efficiency of focal plane area usage. Along a given column of microlenses, the mean interval between neighboring spectra is 3.3 pixels in the horizontal direction and 10.0 pixels in the vertical direction. Each spectrum takes up a length of approximately 27 pixels in the dispersion direction.

2.3 Spectrograph Focal Plane Model

Rather than relying purely on design predictions, we have written procedures to empirically determine the IFU response, capturing the minute optical distortions and alignment changes unique to each observing run. Two forms of calibration data are used as input for the focal plane model. The first kind are the spectrograph images formed by illuminating the

instrument pupil with a tunable laser source. These allow us to characterize the response at fixed wavelengths across the passband. Secondly, during each observing run we observe a broadband source of nearly uniform brightness across our field of view—either the Moon or the twilight sky. In the case of the Moon calibration images, the telescope AO correction loop was turned off, and several exposures with different pointings were averaged. These images constrain the geometry of the focal plane, including the positions and shapes of the individual spectra formed on the detector, as well as large-scale variations in sensitivity across the field of view due to vignetting.

2.3.1 Spectrograph Point Spread Function Model

An accurate model of the monochromatic spectrograph point spread function (PSF) is at the core of the IFU focal plane model. We emphasize the distinction here from the coronagraph PSF, which is formed on the microlens array at the entrance of the IFU. The spectrograph PSF, on the contrary, is the signal formed on the IFU focal plane from monochromatic light incident on an individual microlens. In a laboratory environment before the first scientific observing run, we illuminated the IFU with a tunable laser source and recorded narrowband emission (bandwidth < 4 nm) images at wavelengths in 0.01 μm increments spanning the 0.7 μm operating band of the instrument. Any given laser image shows a grid of 3.8×10^4 point spread functions, each corresponding to a microlens illuminated by the beam entering the spectrograph. From these images, we derived an analytic model of the spectrograph PSF specific to the recorded wavelength, as follows: First, a script looped through all of the PSFs in the spectrograph image, forming a 9×9 pixel *mean* PSF based on the subset

having centroids within 0.05 pixels of a detector pixel center. Next, we experimented with a variety of two-dimensional functional forms to represent the PSF, progressively adding parameters until finding one with a good match to the data. Since in our case the detector pixel width is comparable to the PSF full-width half maximum value, it was necessary to take into account not only the effect of the finite detector pixel area in sampling the function, but also intra-pixel sensitivity variations.

Charge diffusion is the largest contribution to non-uniform sensitivity within any given pixel. During the technology development phase of a space mission to survey extragalactic supernovae, Brown (2007) measured the effect of charge diffusion on the intra-pixel sensitivity of a HAWAII-2 detector. He found a good empirical fit to a typical pixel's response by convolving a tophat function (with width equal to that of the detector pixel) with a hyperbolic secant diffusion term, $\mathrm{sech}(\frac{r}{l_d})$, where r is radius from origin and l_d is the diffusion length. With the established diffusion length of 1.9 μm (compared to the 18 μm full pixel width), the response falls to about 50% of the peak at the middle of each pixel edge. For lack of similar measurements of our own HAWAII-2 detector, we assumed the same charge diffusion behavior.

We discretized the two-dimensional functions representing the PSF, $\mathcal{P}_M(u,v)$, and intra-pixel response, $\mathcal{R}_M(i,j)$, at a resolution of M times that of the detector, where M is an odd number ≥ 3. In other words, the image model has $M \times M$ samples contained within each detector pixel, one always aligned with the center of a pixel. The intra-pixel response function, $\mathcal{R}_M$, is only defined over an area of one pixel, so that $i,j \in \{0,1,\ldots,M-1\}$, whereas $\mathcal{P}_M$ is defined over the entire $9M \times 9M$ area of the mean PSF cutout, correspond-

ing to $u,v \in \{0,1,\ldots,9M-1\}$. In this notation, the detector-downsampled PSF, $\mathbb{P}(x,y)$ is determined by

$$\mathbb{P}(x,y) = \sum_{i=0}^{M-1}\sum_{j=0}^{M-1} \mathcal{P}_M(i+Mx, j+My)\mathcal{R}_M(i,j) \tag{2.1}$$

where $x,y \in \{0,1,\ldots,8\}$ are independent variables representing detector samples over the 9×9 pixel mean PSF cutout.

We found a satisfactory functional form to match the monochromatic PSF by taking the sum of two piecewise, two-dimensional Gaussian profiles, defined as follows:

$$\mathcal{P}_M(u,v) = \begin{cases} Ae^{-\left(\frac{r(u,v)^2}{2\sigma_{A,r}^2}+\frac{s(u,v)^2}{2\sigma_{A,s+}^2}\right)} + Be^{-\left(\frac{r(u,v)^2}{2\sigma_{B,r}^2}+\frac{s(u,v)^2}{2\sigma_{B,s+}^2}\right)} & s>0 \\ Ae^{-\left(\frac{r(u,v)^2}{2\sigma_{A,r}^2}+\frac{s(u,v)^2}{2\sigma_{A,s-}^2}\right)} + Be^{-\left(\frac{r(u,v)^2}{2\sigma_{B,r}^2}+\frac{s(u,v)^2}{2\sigma_{B,s-}^2}\right)} & s\leq 0 \end{cases} \tag{2.2}$$

where

$$\begin{bmatrix} r \\ s \end{bmatrix} = \begin{bmatrix} \cos\theta & \sin\theta \\ -\sin\theta & \cos\theta \end{bmatrix} \begin{bmatrix} \frac{1}{M}\left(u-\frac{9M-1}{2}\right) \\ \frac{1}{M}\left(v-\frac{9M-1}{2}\right) \end{bmatrix} \tag{2.3}$$

Nine parameters fully describe the PSF in this formulation: two amplitudes, six characteristic widths, and one rotation. The piecewise definition allows freedom from reflective symmetry across the r axis. Hence there is a pair of characteristic widths for each side of the s axis—one for $s>0$ ($\sigma_{A,s+}$ and $\sigma_{B,s+}$) the other for $s\leq 0$ ($\sigma_{A,s-}$ and $\sigma_{B,s-}$). Also note the coordinate transformation built into the definition (Equation 2.3). The operations in the right hand column vector serve two purposes. First, they shift the effective origin from the lower left corner of the 9×9 cutout array—its original position for the purpose of simplified indexing in Equation 2.1—to its center. At the same time, the $\frac{1}{M}$ factor scales both

Table 2.1. Parameters describing the P1640 IFU PSF at two wavelengths, as defined in Equation 2.2.

Wavelength (μm)	A	B	$\sigma_{A,u}$	$\sigma_{B,u}$	$\sigma_{A,v+}$	$\sigma_{A,v-}$	$\sigma_{B,v+}$	$\sigma_{B,v-}$	θ
1.25	1.31	0.33	0.52	0.85	0.38	1.22	0.91	1.85	18.2°
1.58	1.32	0.27	0.55	0.81	0.44	1.14	0.90	1.87	14.6°

coordinates to units of detector pixel width. Finally, the 2×2 matrix facilitates a rotation of the overall surface by angle θ in the counterclockwise sense.

Using MPFIT, the non-linear least squares fitting program written by Markwardt (2009), we determined the function parameters for the mean PSF cutouts at wavelengths 1.25 μm and 1.58 μm. The results, based on a model spatial sampling rate of $M = 11$ times that of the detector, are listed in Table 2.1. In each case, the amplitudes were scaled so as to give unity peak intensity in the detector-downsampled PSF. As in Equation 2.2, the characteristic widths are in units of detector pixel widths. In Figure 2.3 we have plotted orthogonal cross sections of the best-fit PSF functions. In the same figure we drew bars to represent the corresponding detector-downsampled PSF cross sections. Note that the peak of each model function is significantly higher than that of the detector-downsampled version, due to the sensitivity roll-off away from the pixel center. At both wavelengths, the mean residual disparity between the downsampled best-fit model and the original mean laser PSF cutout (not shown in the plot) is the less than 1% of the peak intensity.

2.3.2 Spectrum Image Model

We built upon knowledge of the spectrograph PSF to characterize the coarse near-infrared spectra distributed across the IFU focal plane. Here we turned to our Moon and twilight sky

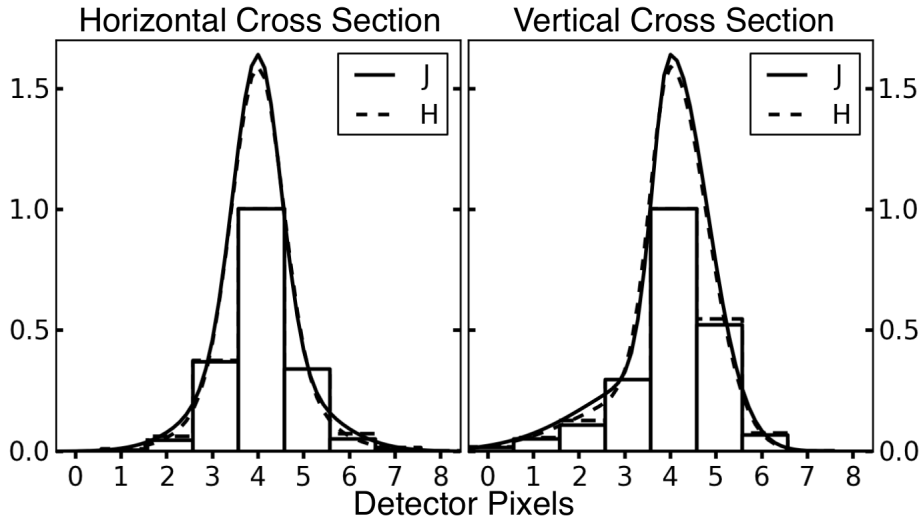

Figure 2.3 Orthogonal cross sections through the center of the IFU PSF fit for wavelengths 1.25 μm (J) and 1.58 μm (H). The curves illustrate the function given in Equation 2.2 with the parameters given in Table 2.1. The bars represent the same models after being downsampled to the detector resolution using the assumed intra-pixel response.

Table 2.2. Definitions of parameters describing the geometry of an individual spectrum image. The mean, range, and standard deviation values of the parameters, as determined for the September 2009 focal plane, are also listed.

Parameter	Definition	Mean	Range	Std. Dev.
Position (X_0, Y_0)	$(X_{1.37\mu m}, Y_{1.37\mu m})$	N/A	(0.0–2047.0, 0.0–2047.0)	N/A
Height (h)	$Y_{1.10\mu m} - Y_{1.76\mu m}$	23.9 pixels	23.5–24.7 pixels	0.2 pixels
Tilt (t)	$(X_{1.10\mu m} - X_{1.76\mu m}) / (Y_{1.10\mu m} - Y_{1.76\mu m})$	0.044	0.0090–0.080	0.021

calibration exposures, during which each microlens was illuminated with a strong, uniform, broad spectrum of light. An example image of this kind was illustrated in Figure 2.2. By isolating the small detector area containing an individual microlens signal, we can fit a set of parameters encoding the spectrum geometry.

In Table 2.2 we have listed the parameters needed to describe the spectrum image of an individual microlens. The (X_0, Y_0) position coordinates are the most fundamental of these. They are referenced to the λ = 1.37 μm point, which coincides with the sharp (blue) edge

of the telluric water absorption trough between the J and H bands. The X,Y coordinates index the full detector array from an origin at the pixel in the lower left (SW) corner of the image; all integral values align with a pixel center. Using similar notation, we defined the spectrum height and tilt based on the relative positions of the λ = 1.10 μm and 1.76 μm points, which roughly correspond to the edges of our passband. From the position, height, and tilt, the coordinates of an arbitrary wavelength in the spectrum can be calculated by the following parameterized equations:

$$\begin{aligned} X(w) &= X_0 + th\left(\tfrac{9-w}{22}\right) \\ Y(w) &= Y_0 + h\left(\tfrac{9-w}{22}\right) \end{aligned} \tag{2.4}$$

where h is height, t is tilt, and $w = (\lambda - 1.1\,\mu\text{m})/0.03\,\mu\text{m}$. By this definition, each integral step in w corresponds to 0.03 μm, so there is a total of 22 such increments from 1.10 μm and 1.76 μm. Using the same wavelength parameter, we can specify the intrinsic spectrum incident on the focal plane by some function $s(w)$ for $0 \leq w \leq 22$.

We introduce the concept of spectrum *trace* to model the layout of the spectrum by an ideal "skeleton" image formed by a train of impulse functions, unencumbered by diffraction and focus effects. The trace is discretized in the same manner as the PSF model, at a resolution M times higher than that of the detector. In this case, however, we use a lower spatial sampling rate factor of $M = 7$ to balance reasonable execution speed and performance. By convolving the trace with the reverse of the PSF (rotated 180°), and downsampling the result, we can synthesize a spectrum image as measured by the detector (Figure 2.4). The position, height, and tilt parameters, along with the intrinsic spectrum can then be adjusted by a least squares fitting algorithm until the downsampled result matches the data cutout.

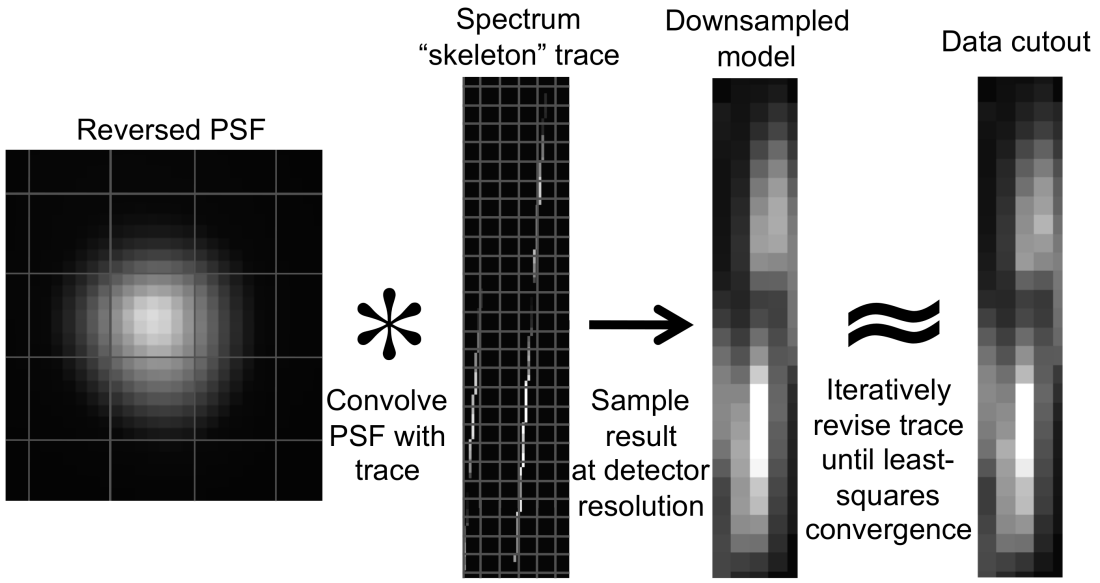

Figure 2.4 Diagram summarizing the microlens spectrum modeling procedure. On the far left, the IFU PSF model (reflected about the center) is shown with a spatial sampling factor 7 times that of the detector, with an overlaid grid of gray lines representing pixel boundaries. We convolve this with the spectrum model trace shown in the next panel (again shown with a gray grid to illustrate the scale of detector pixels) in order to simulate the true light distribution. To test the accuracy of the trace, we downsample the convolution result to the detector resolution, and compare it to the data cutout being fit. The fitting algorithm switches between adjusting the trace parameters and repeating the convolution and downsampling procedure until the model converges.

A cutout spanning an area of 9×29 detector pixels is sufficient to enclose an individual spectrum as well as major portions of the two nearest neighbors. At the start of the fitting procedure, the cutout is aligned such that the (X_0, Y_0) reference point of the spectrum nearly corresponds to pixel position (4, 16) in the detector-downsampled trace array. Two free parameters in the model, ΔX and ΔY, allow the algorithm to refine the initial position guess alongside the other geometrical properties. For a given microlens spectrum, the following equations define the conversion between X, Y detector indices and u, v trace array indices:

$$\begin{aligned} u &= \left(X - X_0 + \tfrac{9}{2} + \Delta X\right) M \\ v &= \left(Y - Y_0 + \tfrac{33}{2} + \Delta Y\right) M \end{aligned} \tag{2.5}$$

from which it follows that the trace indices of the 1.37 μm reference point are $(u_0, v_0) = \left(M\left(\frac{9}{2} + \Delta X\right), M\left(\frac{33}{2} + \Delta Y\right)\right)$. Based on the typical interval between spectra along a microlens, we set the 1.37 μm reference points of the neighboring spectra by $(u_{0\uparrow}, v_{0\uparrow}) = (u_0 + 3.3M, v_0 + 10.0M)$ and $(u_{0\downarrow}, v_{0\downarrow}) = (u_0 - 3.3M, v_0 - 10.0M)$.

The trace signal is dispersed over the same line segment defined in Equation set 2.4, with intrinsic spectrum function $s(w)$. The neighboring spectra are parameterized by the same shape with respect to their own reference points, $(u_{0\uparrow}, v_{0\uparrow})$ and $(u_{0\downarrow}, v_{0\downarrow})$. We form separate trace arrays for the J- and H-band halves of the spectra, designated $\mathcal{T}_{J,M}(u,v)$ and $\mathcal{T}_{H,M}(u,v)$. We do this in anticipation of separate convolution operations with the J- and H-band PSFs (Figure 2.3). The two respective trace arrays are defined as follows:

$$\mathcal{T}_{J,M}(u,v) = \begin{cases} s(w) & -\frac{1}{2} < u - u_0 - t(v - v_0) \leq \frac{1}{2} \text{ and } 0 \leq w < 10 \\ s(w_\uparrow) & -\frac{1}{2} < u - u_{0\uparrow} - t(v - v_{0\uparrow}) \leq \frac{1}{2} \text{ and } 0 \leq w_\uparrow < 10 \\ s(w_\downarrow) & -\frac{1}{2} < u - u_{0\downarrow} - t(v - v_{0\downarrow}) \leq \frac{1}{2} \text{ and } 0 \leq w_\downarrow < 10 \\ 0 & \text{otherwise} \end{cases}$$

$$\mathcal{T}_{H,M}(u,v) = \begin{cases} s(w) & -\frac{1}{2} < u - u_0 - t(v - v_0) \leq \frac{1}{2} \text{ and } 10 \leq w \leq 22 \\ s(w_\uparrow) & -\frac{1}{2} < u - u_{0\uparrow} - t(v - v_{0\uparrow}) \leq \frac{1}{2} \text{ and } 10 \leq w_\uparrow \leq 22 \\ s(w_\downarrow) & -\frac{1}{2} < u - u_{0\downarrow} - t(v - v_{0\downarrow}) \leq \frac{1}{2} \text{ and } 10 \leq w_\downarrow \leq 22 \\ 0 & \text{otherwise} \end{cases} \tag{2.6}$$

where $w = 9 - \frac{22}{Mh}(v - v_0)$, $w_\uparrow = 9 - \frac{22}{Mh}\left(v - v_{0\uparrow}\right)$, and $w_\downarrow = 9 - \frac{22}{Mh}\left(v - v_{0\downarrow}\right)$.

To test a given set of spectrum model parameters, we convolve the J and H trace arrays with the reverse of the PSF model (such that $\mathcal{P}'_M(i,j) = \mathcal{P}_M(-i,-j)$), giving a high-resolution model of the light distribution on the focal plane, $\mathcal{S}_M(u,v)$:

$$\mathcal{S}_M = \mathcal{T}_{J,M} * \mathcal{P}'_{J,M} + \mathcal{T}_{H,M} * \mathcal{P}'_{H,M} \tag{2.7}$$

Implicitly, we have zero-padded the trace arrays before the convolution, and trimmed the result to the original $9M \times 29M$ array size. The detector-downsampling operation is similar to that used earlier for the PSF model:

$$\mathbb{S}(x,y) = b + \sum_{i=0}^{M-1}\sum_{j=0}^{M-1} \mathcal{S}_M(i+Mx, j+My)\mathcal{R}_M(i,j) \tag{2.8}$$

However, one new variable has been introduced in Equation 2.8: b, a constant offset added to each pixel in the downsampled image model. This is one more parameter open to adjustment by the fitting procedure, which takes into account any background level of scattered light present in the data cutout. For a point source, in some focal plane locations this background reaches up to 3% of the 99.5 percentile-level count rate, considering all detector pixels. Therefore, it becomes especially significant for an exposure of a source as bright as the Moon. The resulting synthetic spectrum image $\mathbb{S}$ can be directly compared with the data cutout (Figure 2.4). In principle, the least squares fitting algorithm (the MPFIT program in our case) converges on the data cutout over many loops, switching between revising the trace model parameters and comparing the downsampled result to the data.

The combination of unknown position, shape, and intrinsic spectrum $s(w)$ presents too many free parameters for a fitting algorithm to accurately solve for at once. In practice, we need to iteratively build up constraints, starting from as few assumptions as possible. One aspect of the Moon/sky calibration exposure we can take advantage of is the fact that the intrinsic spectrum, $s(w)$, is identical across the image, apart from scale factors due to large-scale variations in sensitivity over the field of view. In addition, by referring to the laser calibration images, we can make very good initial guesses of the height and tilt for a given region of the focal plane. Still, we found these constraints alone were insufficient to reach consistent solutions. The exact vertical position of the spectrum (encoded by ΔY in Equation Set 2.5) proved especially difficult to determine with only limited information about the light source and the instrument response. To get over this barrier, we chose to use prior knowledge of the atmosphere's transmission function—in particular, the shape imposed on the spectrum by the deep water absorption trough in the middle of the P1640 passband.

Figure 2.5 shows the expected transmission function of the atmosphere from 1.28 μm to 1.52 μm. The data points are based on the measurements made by Manduca & Bell (1979) from Kitt Peak (at altitude 6875 ft, comparable to the 5618 ft altitude of the Palomar Observatory Hale Telescope), here averaged over 0.01 μm bins. Instead of allowing the points inside the water trough ($6 < w < 14$) to vary freely, we impose the condition

$$s(w) = \begin{cases} T_{\text{atm}}(w)s(6) & 6 < w < 10 \\ T_{\text{atm}}(w)s(14) & 10 \leq w < 14 \end{cases} \tag{2.9}$$

where $T_{\text{atm}}(w)$ is the peak-normalized atmospheric transmission function plotted in Fig-

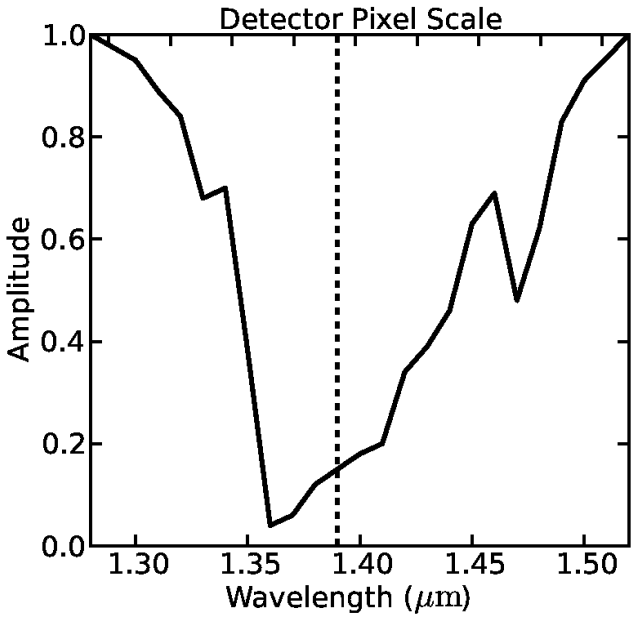

Figure 2.5 The atmospheric transmission function around the water absorption trough between the *J* and *H* bands, binned to 0.01 μm resolution, based on the measurements by Manduca & Bell (1979). The tick marks on the top axis indicate the scale of vertical detector pixels along the dispersion axis of the spectrum. During the spectrum fitting procedure, when the exact position and shape have not yet been established, the model trace spectrum $s(w)$ is forced to follow this profile in the range $\lambda = 1.30$–$1.50\,\mu$m. The dotted line separates those points of $s(w)$ that are fixed relative to the free spectrum value at $\lambda = 1.28\,\mu$m ($6 < w < 10$) versus $\lambda = 1.52\,\mu$m ($10 \leq w < 14$).

ure 2.5. Inside the water trough, $s(w)$ is discretized in 0.01 μm bins; outside, in 0.03 μm bins (integral values of w). Once the above assertion is in place, the fitting algorithm could at last reliably determine both the position and shape of the spectrum, as achieved in the example shown in Figure 2.4.

2.3.3 Global Spectrograph Focal Plane Solution

We repeated the spectrum fitting procedure across the entire spectrograph image to form a global solution unique to the specific epoch of the Moon/sky calibration exposure. To

minimize the number of free parameters before executing this, we first determined a mean intrinsic spectrum $\overline{s}(w)$ based on average of the $s(w)$ fit results from a sub-area of about 100 spectra near the center of the field of view. With the spectrum shape fixed, however, there needs to be a parameter that captures variations in overall signal strength across the focal plane. We designated an amplitude parameter a to acts as a multiplicative constant, applied to $\overline{s}(w)$, and freely adjusted alongside X_0, Y_0, h, t, and d.

In Figure 2.6 we have displayed maps of the height, tilt, and amplitude parameters for one epoch. These maps proved essential to the challenging process of debugging the fitting routines. They also enable easy visual comparisons between focal plane properties at different times, and can serve as diagnostic tools during periods of modifications and upgrades to instrument optics. The maps in Figure 2.6 appear as rotated squares because the microlens array is by design rotated with respect to the detector (as shown previously in Figure 2.2). We index the microlenses using Cartesian coordinates i and j relative to an origin at the lower left corner. With these coordinates, a range of $0 \leq i, j < 250$ is sufficient to enclose the 3.8×10^4 microlens spectra on the detector.

The ability to analyze the *spatial* distribution of the IFU spectra is also of great interest. A vector field, like those depicted in Figure 2.7, is an effective way to illustrate the evolution of the global spectrograph focal plane geometry. To make these plots, we first partitioned the calibration image into an array of 8×8 boxes, each of width 256 detector pixels. For any two comparison epochs, each with spectrum position arrays $X_0(i, j)$ and $Y_0(i, j)$, we calculated the median of the differences $\Delta X_0(i, j)$ and $\Delta Y_0(i, j)$ inside each box, resulting in an 8×8 array of vectors. Before plotting those vectors, we subtracted the me-

dian difference vector at the image center. In this way, we removed the effect of a trivial bulk shift between the focal plane patterns.

Depending on the duration of time between the pair of calibration images under consideration, the quivers representing the vectors need to be scaled up by different factors to reveal the subtle evolution. Once this is done, it becomes clear that the overall scale and orientation of the spectrograph focal plane pattern vary with time. More complicated, non-uniform distortions also play a role. In all cases, the magnitude of these changes are small enough that they would never be obvious from a mere "blinking" comparison of the source images. For example, the transformation from March 2009 to June 2009 can mostly be attributed to a rotation of the microlens array with respect to the detector (or vice versa) by an angle of merely $14''$. Likewise, between 28 June 2009 and 29 June 2009, the focal plane was magnified by about 0.003%. It is a fair guess that the changes we observe in global focal plane geometry are due to minute variations of environmental conditions inside the IFU dewar. However, it remains unclear what the relative contributions are from the various optics and the mechanical support structures. To an extent, the origin of these changes is not an issue, so long as each science data set can be attached to a solution that accurately reflects its particular geometry.

Another important product of our global fitting procedure is a synthetic image of the entire spectrograph focal plane. Using the established geometric parameters, we can inject an arbitrary source spectrum $s_\star(w)$ to simulate the distribution of light incident on the detector. The synthetic focal plane image is useful for inspecting the results of the global fit, and is also an essential ingredient in the algorithm used by the cube extraction pipeline

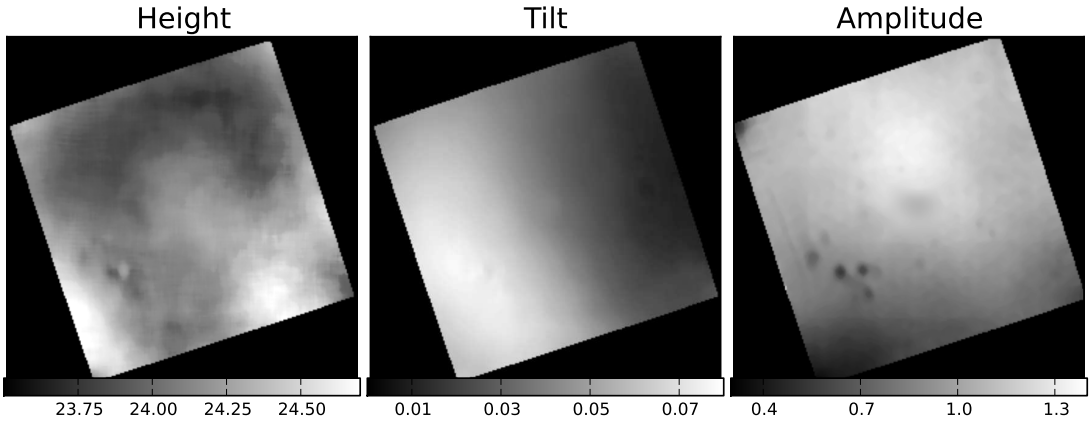

Figure 2.6 Maps of spectrum parameters making up one global spectrograph focal plane solution. This particular solution is based on the fit to the Moon calibration image acquired on 28 June 2009. The maps appear rotated due to the orientation of the microlens array with respect to the detector (see Figure 2.2). Height is shown in units of detector pixels, tilt is an inverse slope (unitless), and amplitude is mean-normalized.

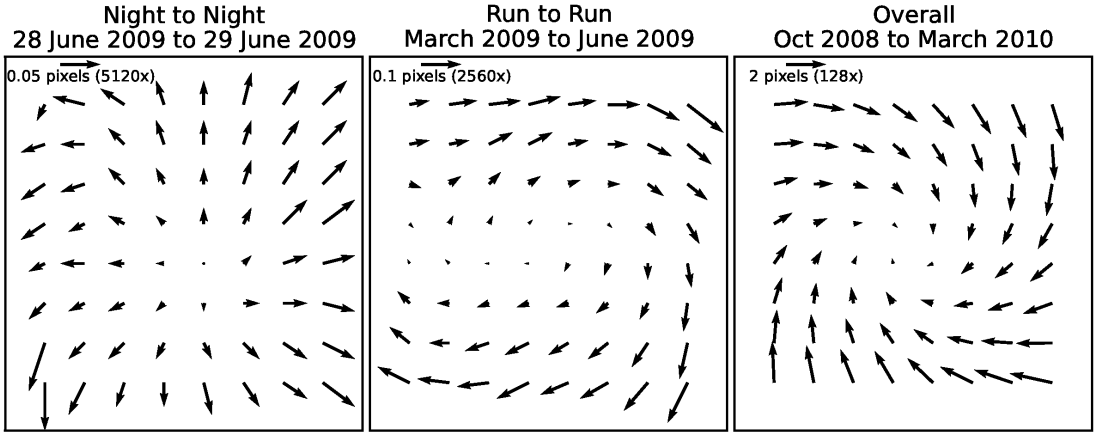

Figure 2.7 Vector field plots illustrating examples of the evolution of the spectrograph focal plane geometry over three time intervals: 1 day, 3 months, and 17 months. Each quiver represents the median change in spectrum position inside a box $1/8^{\text{th}}$ of the full image width. In the top left corner of each plot, a small legend indicates the relative scale of the quiver in terms of detector pixel widths. For each comparison, we customized the quiver scale factor to clearly reveal the transformation.

to register the spectrograph image of an individual science exposure at sub-pixel precision (described in § 2.4.1.5). The formalism is analogous to that described for the individual spectrum cutout model in Equations 2.5–2.8. We designate $\mathcal{F}_J(p,q)$ and $\mathcal{F}_H(p,q)$ to represent the J- and H-band model trace arrays of the full spectrograph focal plane image, discretized at a spatial sampling rate M times that of the detector. Since the HAWAII-2 detector array size is 2048×2048, the trace arrays are defined over $p,q \in \{0,1,\ldots,2048M-1\}$. Here we again settled on a sampling factor of $M = 7$. Since as before, we require M to be an odd integer ≥ 3, there is always a pair of trace array indices p,q aligned with the center of a given detector pixel X,Y:

$$\begin{aligned} p &= MX + \tfrac{M-1}{2} \\ q &= MY + \tfrac{M-1}{2}. \end{aligned} \tag{2.10}$$

The trace array is determined by the position, height, and tilt solutions, now indexed by microlens coordinates i, j:

$$\begin{aligned} \mathcal{F}_{J,M}(p,q) &= \sum_{i=0}^{249}\sum_{j=0}^{249} \mathcal{S}_{J,M,i,j}(p,q) \\ \mathcal{F}_{H,M}(p,q) &= \sum_{i=0}^{249}\sum_{j=0}^{249} \mathcal{S}_{H,M,i,j}(p,q) \end{aligned} \tag{2.11}$$

where

$$\mathcal{S}_{J,M,i,j}(p,q) = \begin{cases} s_\star(w_{ij}) & -\frac{1}{2} < p - p_{0_{ij}} - t_{ij}(q - q_{0_{ij}}) \leq \frac{1}{2} \quad \text{and} \quad 0 \leq w_{ij} < 10 \\ 0 & \text{otherwise} \end{cases}$$

$$\mathcal{S}_{H,M,i,j}(u,v) = \begin{cases} s_\star(w_{ij}) & -\frac{1}{2} < p - p_{0_{ij}} - t_{ij}(q - q_{0_{ij}}) \leq \frac{1}{2} \quad \text{and} \quad 10 \leq w_{ij} \leq 22 \\ 0 & \text{otherwise} \end{cases}$$

$$p_{0_{ij}} = MX_{0_{ij}} + \tfrac{M-1}{2}, \quad q_{0_{ij}} = MY_{0_{ij}} + \tfrac{M-1}{2}, \quad \text{and}\, w_{ij} = 9 - \tfrac{22}{Mh_{ij}}\left(q - q_{0_{ij}}\right). \tag{2.12}$$

From the trace arrays, we obtain the spectrograph focal plane image model $I_M(p,q)$ in the same manner as in § 2.3.2, by convolving them with their corresponding reversed PSF models:

$$I_M = \mathcal{F}_{J,M} * \mathcal{P}'_{J,M} + \mathcal{F}_{H,M} * \mathcal{P}'_{H,M} \tag{2.13}$$

We implement these convolution operations in the Fourier domain to save computational time, which is otherwise a nuisance for the large dimensions of our arrays (Bracewell 2006, chap. 6). With a spatial sampling factor of $M = 7$, we obtain a factor of ~ 50 using FFT-based convolution over direct convolution. In our experience, this cuts the execution time needed to form the synthetic image down from a few hours to a few minutes (assuming the global solution is already done).

Finally, we can obtain the detector-downsampled synthetic focal plane image, $\mathbb{I}(X,Y)$, by binning I_M to the detector resolution using the assumed intra-pixel response:

$$\mathbb{I}(X,Y) = \sum_{i=0}^{M-1}\sum_{j=0}^{M-1} I_M(i+MX, j+MY)\mathcal{R}_M(i,j) \tag{2.14}$$

Note that this synthetic detector image is idealized in the sense that we have left out the amplitude modulations across the image (a_{ij}) as well as background light parameters (d_{ij}). For the purpose of registering a science spectrograph image, this is preferred, since we are only concerned with matching the shapes and positions of the spectra.

2.4 Data Cube Extraction Pipeline

The Project 1640 Data Cube Extraction Pipeline (PCXP), written in the GNU C programming language, automates the processing of raw P1640 detector images and their translation to reduced data cubes. A block diagram summarizing the steps applied to each image is shown in Figure 2.8. By design, the program is fast enough to use while observing, so that newly acquired images can be inspected in real time to monitor instrument performance and check for unknown objects. The data pipeline can also be used to process an arbitrarily large set of raw data at a later date. For post-processing, we feed the output of the PCXP into the Project 1640 Speckle Suppression Pipeline (PSSP), described by Crepp et al. (2011).

Two outer loops comprise the PCXP execution. First, the program steps through the detector data in the input directory specified by the user at the start time, processing each non-destructive read (NDR) sequence to form a reduced, registered spectrograph image. The second stage of the pipeline loops through the finished spectrograph images and ex-

tracts data cubes from each of them. Throughout these steps, the pipeline relies on the empirical model of the spectrograph focal plane described in § 2.3.

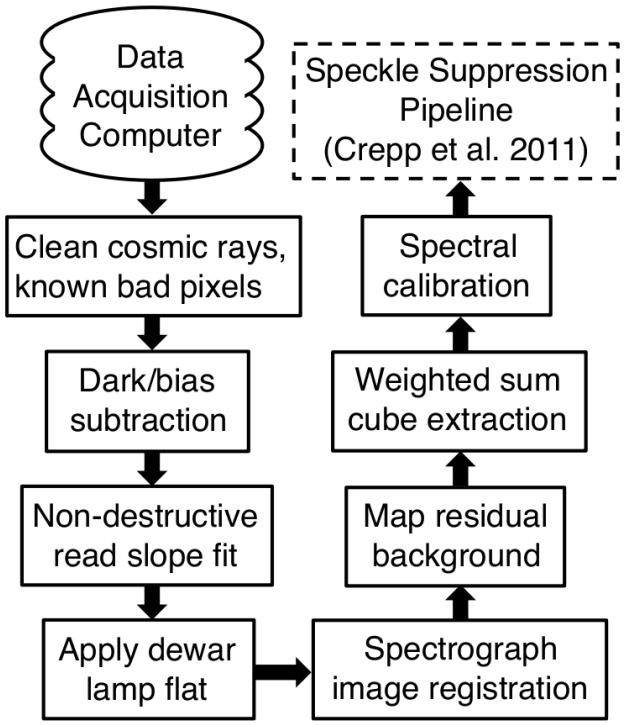

Figure 2.8 Block diagram of the Project 1640 Data Cube Extraction Pipeline (PCXP). Raw detector data are processed into reduced, registered spectrograph images (§ 2.4.1). In the second main loop, beginning with the residual background mapping, the spectrograph images are translated to data cubes with the help of the global spectrograph focal plane solution (§ 2.4.2).

2.4.1 Detector Image Processing

2.4.1.1 Cosmic Ray Removal

The pipeline identifies pixels contaminated by cosmic rays by checking for anomalous jumps in digitized count values within the NDR sequence. For each detector pixel, our algorithm determines the median increase in counts between successive reads over the course

of the exposure. A count increment greater than five times the median is flagged as a cosmic ray event. At each pixel meeting this criterion, the count contribution of the cosmic ray event is subtracted from the read corresponding to the event as well as all the following reads, canceling out its influence. We chose our threshold based on inspections of images of faint occulted stars, with relatively noisy slopes. We blinked “before” and ”after” images to check that all apparent cosmic ray events, and no starlight-dominated pixels were erroneously flagged.

This method of cosmic ray removal only works for exposures consisting of more than two reads. For a shorter exposure there is no way to take advantage of the NDR detector mode to identify cosmic rays. In this case the pipeline passes the detector image through the IRAF NOAO cosmic ray cleaning algorithm.

2.4.1.2 Bias/Dark Subtraction

During each observing run, a set of “dark” NDR sequences are obtained by taking calibration exposures with the IFU in a cryogenic state identical to the scientific data acquisition mode, except that the coronagraph beam entrance window is capped to obstruct external light. These dark exposures record the bias, thermal, dark current, and badly-behaved “hot” pixel count values of the detector array at each read interval. The median of 11 dark NDR sequences for each exposure time is added to a permanent library directory of dark exposures, marked by date and exposure time. See Figure 2.9 for an example of a dark exposure. After loading the *dat* file of a science target, the first processing step of the pipeline is to find the most appropriate dark NDR sequence and perform a readwise subtraction.

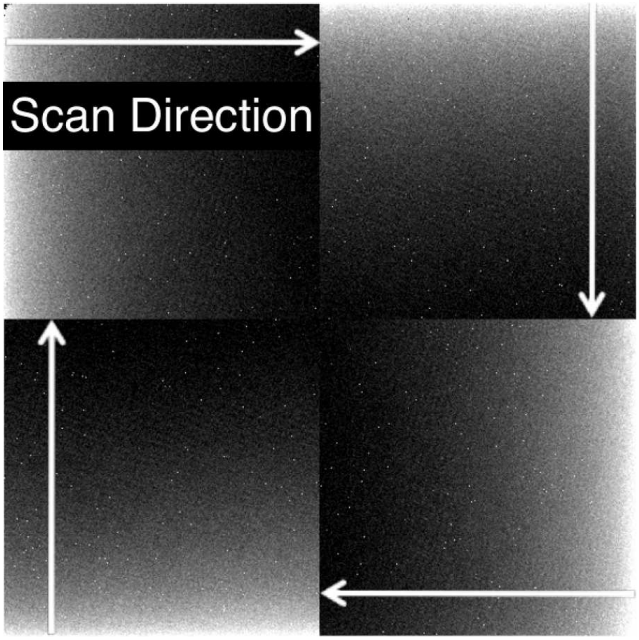

Figure 2.9 An example of a dark exposure used to subtract the bias, thermal counts, and hot pixels from science images. The "bias tilt"—the gradient in the bias pedestal—is strongest along the scan direction of each detector quadrant (each with its own read-out amplifier).

2.4.1.3 Non-destructive Read Slope Fitting

After subtracting the bias/dark component and removing the cosmic rays, the pipeline fits a slope to the ADU count versus time values recorded in the NDR sequence. This reduces the detector data for a given exposure to a single 2048×2048 pixel representation of the spectrograph image. We employ an ordinary least-squares linear regression to determine the count rate for each pixel, eventually storing the floating point values in a FITS file in units of counts/second.

The slope fitting is complicated by pixel saturation caused by bright sources. However, the NDR detector mode is advantageous for handling this. In the case where a pixel reaches saturation at some point after the first two reads, the affected reads are simply excluded from that pixel's linear regression. This approach, recommended after tests de-

scribed by Ives (2008), extends the effective dynamic range of a long exposure by a factor of $\sim N_{reads}/2$. For pixels that reach saturation before the second read, a slope computation is not possible. If this saturation occurred between the first and second reads, then the slope can at least be approximated based on the difference between the first read value and an assumed zero level from the dark NDR sequence. However, in the case of a pixels saturating before the first read, this result will not be physically meaningful. To prevent erroneous measurements from being made by investigators analyzing images affected by saturation, the pipeline sets an appropriate header variable in the reduced FITS files. This header keyword indicates whether any of the detector pixels saturated, and if so, whether that occurred at the first, the second, or a subsequent read.

2.4.1.4 Detector Flat-Fielding

A externally controlled lamp inside the dewar of the P1640 IFU can fully illuminate the detector. To counteract pixel-to-pixel variations in detector sensitivity, we constructed a detector flat field map based on the mean of 12 dewar lamp exposures. Since the lamp intensity is not uniform across the detector, we used IRAF to fit a cubic spline surface to the normalized, mean dewar lamp image. We divided by the resulting spline surface to form the final detector flat, with large-scale variations removed (see the next section for an explanation of how large-scale variations in sensitivity are corrected for during cube extraction). The standard deviation of pixel values in the detector flat field map is 0.13. After the NDR slope-fitting step, the pipeline divides the spectrograph image by the flat field map to compensate for pixel-to-pixel variations. For locations in the flat field map

with exceptionally low values (< 0.3), no division is carried out since doing so would tend to enhance the noise induced by weak, problematic pixels.

2.4.1.5 Spectrograph Image Registration

Due to flexure—varying mechanical stress on the instrument while the telescope slews—the projection of the microlens array onto the detector changes over the course of an observing period. The plot in Figure 2.10 illustrates the magnitude of this effect based on measurements from three observing runs. Between targets, the positions of the spectra on the detector can uniformly shift by up to 2 pixels in each direction. Between observing runs there is a more pronounced, systematic shift in the spectrograph-detector alignment. To accurately extract the data, the pipeline needs to register the precise offset between each spectrograph image and the focal plane model of the corresponding epoch. We accomplish this through two stages: first a crude estimate based on a cross-correlation with the downsampled spectrograph image model (array $\mathbb{I}$ in Equation 2.14), followed by a more elaborate approach to refine the offset to sub-pixel precision.

For efficiency, the initial cross-correlation is restricted to a 200×200 square pixel section of the science image $\mathbb{D}(X,Y)$. We denote this cutout box with a tilde accent on top of the original array symbol:

$$\tilde{\mathbb{D}}(x,y) = \mathbb{D}\left(X_p - 100 + x, Y_p - 100 + y\right) \quad \text{for } 0 \leq x,y < 200. \tag{2.15}$$

Likewise we use $\tilde{\mathbb{I}}$ to represent the same section from the downsampled focal plane image model. The center of the box, (X_p, Y_p), is chosen based on the average count rate computed

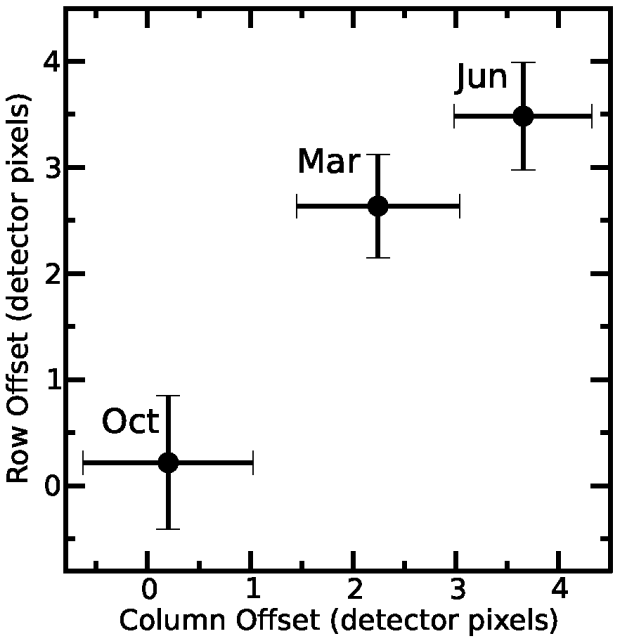

Figure 2.10 Example distributions of the spectrograph-detector alignment offsets with respect to a canonical template. The mean offsets, with bars indicating the standard deviations in each direction, are plotted for three P1640 observing runs: October 2008, March 2009, and June 2009.

within 16×16 partitions across the image, so as to enclose spectra with relatively high signal strength. In a typical science image with the star occulted by the coronagraph, this is near the center of the image, where the residual starlight is brightest.

We cross-correlate $\tilde{\mathbb{I}}$ and $\tilde{\mathbb{D}}$ to determine the *crude* offset. A given science focal plane pattern is not expected to stray more than two pixels away from the calibration exposure of the matching epoch. Furthermore, the periodicity of the spectrum pattern ensures that large lags will merely introduce degenerate solutions. Therefore, we do not compute the full two-dimensional cross-correlation array, but merely a small region bounded by horizontal and vertical lags up to 4 pixels in each direction:

$$\tilde{\mathbb{C}}_0(r,s) = \sum_{x=4}^{195}\sum_{y=4}^{195}\tilde{\mathbb{I}}(x-r,y-s)\tilde{\mathbb{D}}(x,y) \quad \text{for } -4 \leq r,s \leq 4 \tag{2.16}$$

The summation limits take the lag range into account in order to avoid the influence of non-overlapping array edges. The lag combination that maximizes $\tilde{\mathbb{C}}(r,s)$, which we denote (r_p, s_p), is our initial guess for the horizontal and vertical displacement of $\mathbb{D}$ with respect to $\mathbb{I}$.

The second stage of the registration routine determines separately the *fine X* and *Y* offsets. As apparent in Figure 2.2, the spectral dispersion is almost completely aligned with the *Y* axis of our detector image coordinate system. As a consequence, the shape of a spectrum's horizontal cross-section at a given wavelength is determined much more by the spectrograph PSF shape than by the intrinsic spectrum of the light source. It is effectively the cross-dispersion profile commonly referred to in literature on more conventional spectroscopic observations (e.g, Miskey & Bruhweiler 2003). Therefore, to measure the effect of a slight horizontal offset on the detector-sampled image, we can start with the high-resolution model of the light distribution I_M (Equation 2.13 from § 2.3.3), even though its intrinsic spectrum does not necessarily match the data. To simulate how the detector would "see" the image model for a range of small fractional-pixel offsets from the initial alignment, we downsample I_M as in Equation 2.14, but with the detector sampling array shifted by a range of horizontal sub-pixel offsets indexed by the variable integer δ:

$$\tilde{\mathbb{I}}_\delta(x,y) = \sum_{i=0}^{M-1}\sum_{j=0}^{M-1} I_M(M(X_p-100+x)+i-\delta, M(Y_p-100+y)+j)\mathcal{R}_M(i,j)$$
$$\text{for} \quad 0 \le x,y < 200 \quad \text{and} \; -\frac{M-1}{2} \le \delta \le \frac{M-1}{2}. \tag{2.17}$$

Now we reevaluate the cross-correlation peak for the M fine horizontal offsets values, with r and s fixed at r_p and s_p:

$$\tilde{\mathbb{C}}_\delta(r_p,r_s) = \sum_{x=4}^{195}\sum_{y=4}^{195}\tilde{\mathbb{I}}_\delta(x-r_p,y-s_p)\tilde{\mathbb{D}}(x,y) \quad \text{for} \; -\frac{M-1}{2} \le \delta \le \frac{M-1}{2}. \tag{2.18}$$

The fractional offset index δ that maximizes $\tilde{\mathbb{C}}_\delta(r_p,r_s)$ gives the fine horizontal displacement of the data, δ, with respect to the crude initial guess, r_p. The full horizontal offset is $r_p + \delta/M$ detector pixel widths.

We originally intended to use the same approach to determine the fine vertical offset. Unfortunately, in this case the disparity between the intrinsic spectrum of the data and the image model strongly biases the cross-correlation result. In a typical science image, the cutout box $\tilde{\mathbb{D}}$ contains $\sim$10 speckles. Their chromatic position dependence (as illustrated in Figure 2.1) causes steep brightness gradients in the spectra formed on the spectrograph focal plane, since a given microlens will collect light from a speckle over only a fraction of the passband. Whatever intrinsic spectrum is built into the image model, I_M, will significantly differ from that of most of the sample. We found that the effects of these disparities do not average out over an ensemble. Instead, they systematically push the cross-correlation result

up or down by a degree that does not reflect the actual relative wavelength alignment.

Instead of using the image model as an alignment template, we return to the fitting approach described in § 2.3.2. This time, however, rather than fitting the full spectrum parameter set, we concentrate on the region with the most information about the vertical position: the telluric water absorption trough. Therefore, we confine the least-squares fit region to a 3×11 box, aligned such that the 1.37 μm reference point is near the middle pixel on the 8th row.

We further simplify the spectrum fit by describing the local light source with merely two parameters: an amplitude and color. The other free parameters are the background light offset and the vertical position. The height and tilt are already known from the calibration image solution, and the horizontal position is fixed based on the previous step in the registration algorithm. As in Equation 2.9, the spectrum trace points with wavelengths $1.28\,\mu\text{m} < \lambda < 1.52\,\mu\text{m}$ are again tied to the transmission function plotted in Figure 2.5. The anchor points at $\lambda = 1.28$ μm and 1.58 μm are set based on the amplitude and color parameters.

To get a diverse set of spectrum shapes spanning a wide region of the speckle halo, during the fine vertical offset fitting procedure we sample 121 spectra over a 600×600 pixel box (as compared to the 200×200 pixel box used for the horizontal registration). Of the 121 fits, the median vertical offset is taken as the final value, and rounded to the nearest 1/7th of a pixel to match the quantization of the fine horizontal offset. In trial runs, we found the vertical offsets determined from the full set of sample spectra follow a Gaussian distribution, with standard deviation 0.2–0.4 pixel widths, depending on the source image.

We accept this as the uncertainty in the vertical registration.

2.4.2 Cube Extraction

2.4.2.1 The Role of the Global Spectrograph Focal Plane Solution

In order to form a data cube, the pipeline must "know" where individual spectra are positioned on the focal plane, and furthermore, which points of those spectra correspond to a given wavelength. We rely on the global spectrograph focal plane solution described in § 2.3.3 to establish the image geometry for each epoch under consideration. One of the products of the calibration image fitting procedure is a text file tabulating the positions of all 3.8×10^4 spectra alongside their corresponding microlens indices. This table, combined with the results of the registration algorithm (§ 2.4.1.5) and the maps of height and tilt parameters give all the information needed to organize the detector data for a given science image.

The amplitude map produced during the global fit (see Figure 2.6) also has an important role. It compliments the dewar lamp flat described in § 2.4.1.4 by capturing the larger-scale variations in sensitivity across the field of view. By looking up the amplitude parameter associated with a given microlens, we can appropriately scale any detector samples from that spectrum to compensate for optical effects such as vignetting.

2.4.2.2 Residual Background Map

Despite the numerous stages in the detector image processing, some minor extraneous background structure persists into the processed focal plane image. This component, su-

perimposed on the real signal, is caused by a combination of residual bias counts, scattered light within the instrument, and thermal contamination from outside the dewar (unaccounted for in the dark subtraction). In the cube extraction routine, after loading an individual focal plane image, the pipeline forms a map of background count rates based on measurements between spectra.

Figure 2.11 shows the regions used to estimate the background count rate associated with a given microlens. The upper left box is situated so that its bottom row is matched with the $\lambda = 1.28\,\mu$m point (rounded to the nearest row), and the bottom row of the lower right box is on level with $\lambda = 1.67\,\mu$m. For both background boxes, the near side is spaced three columns from the rounded center of the spectrum.

The pipeline takes the median of the sample of the pixels in both 2×5 dark regions and stores this in a residual background map. After forming the background estimates for all microlenses, the resulting map is smoothed with a box median filter and stored for use in the inner extraction loop.

2.4.2.3 Weighted Sum Extraction

Our cube extraction method is summarized in Figure 2.11. After forming the background map, the extraction routine loops through microlens indices i and j. For each microlens, we retrieve the parameters from the global spectrograph focal plane solution: position, height, tilt, and amplitude (represented by the variables $(X_{0_{ij}}, Y_{0_{ij}})$, h_{ij}, t_{ij}, and a_{ij}, respectively). An inner loop steps through 23 wavelength channels in 0.03 μm increments between $\lambda =$ 1.10 μm and 1.76 μm. We index these channels by integer values of w ($0 \leq w \leq 22$),

and determine the extraction target point for each cube element, or *spaxel*, as follows (cf. Equation set 2.4):

$$\begin{aligned} X_{c_{ij}}(w) &= X_{0_{ij}} + r_p + \delta/M + t_{ij} h_{ij} \left(\tfrac{9-w}{22}\right) \\ Y_{c_{ij}}(w) &= Y_{0_{ij}} + s_p + \varepsilon/M + h_{ij} \left(\tfrac{9-w}{22}\right) \end{aligned} \tag{2.19}$$

where r_p and s_p are the crude horizontal and vertical offsets, and δ and ε are the fine horizontal and vertical offset indices determined by the registration algorithm (§ 2.4.1.5) for the current reduced spectrograph image, $\mathbb{D}(X,Y)$. We use a hat symbol to designate the same coordinates rounded to the nearest pixel center: $\left(\hat{X}_{c_{ij}}(w), \hat{Y}_{c_{ij}}(w)\right)$.

The spaxel for each microlens and wavelength combination is based on the weighted sum over a 3×3 detector pixel square centered on $\left(\hat{X}_{c_{ij}}(w), \hat{Y}_{c_{ij}}(w)\right)$:

$$\mathcal{C}(i,j,w) = \sum_{m=-1}^{1} \sum_{n=-1}^{1} \mathbb{W}_{\alpha,\beta,w}(m,n) \left(\mathbb{D}\left(\hat{X}_{c_{ij}}(w)+m, \hat{Y}_{c_{ij}}(w)+n\right) - b_{ij}\right) / a_{ij}. \tag{2.20}$$

The weights $\mathbb{W}_{\alpha,\beta,w}(m,n)$ applied to the detector samples are based on the PSF model, downsampled and truncated to the 3×3 pixel extraction box as follows:

$$\mathbb{W}_{\alpha,\beta,w}(m,n) = \begin{cases} \Gamma_J(\alpha,\beta) \sum_{i=0}^{M-1} \sum_{j=0}^{M-1} \mathcal{P}_{J,M}\left(i+(m+4)M-\alpha, j+(n+4)M-\beta\right) \mathcal{R}_M(i,j) \\ \qquad \text{if } 0 \le w < 10 \\ \\ \Gamma_H(\alpha,\beta) \sum_{i=0}^{M-1} \sum_{j=0}^{M-1} \mathcal{P}_{H,M}\left(i+(m+4)M-\alpha, j+(n+4)M-\beta\right) \mathcal{R}_M(i,j) \\ \qquad \text{if } 10 \le w \le 22 \end{cases}, \tag{2.21}$$

defined for $-1 \le m,n \le 1$. The formulas for the *J*- and *H*-band PSFs, $\mathcal{P}_{J,M}$ and $\mathcal{P}_{H,M}$, as well as the intra-pixel response, $\mathcal{R}_M$, can be found in § 2.3.1. The integers α and β encode the offsets of the extraction target point from the extraction box center:

$$\begin{aligned} \alpha &= \mathit{Round}\left(\left(X_{c_{ij}}(w) - \hat{X}_{c_{ij}}(w)\right) M\right) \\ \beta &= \mathit{Round}\left(\left(Y_{c_{ij}}(w) - \hat{Y}_{c_{ij}}(w)\right) M\right). \end{aligned} \tag{2.22}$$

The resulting indices take on integer values in the range $-\frac{M-1}{2} \le \alpha,\beta \le \frac{M-1}{2}$ (corresponding to offsets up to $\frac{3}{7}$ of a pixel width in each direction when $M = 7$). Lastly, the Γ factor in front of each weight formula compensates for the effect that the offset between the PSF center and the extraction box center has on the sum of products in Equation 2.20. The need for this can be qualitatively understood by the fact that the overall flux in a 3×3 pixel sample of the PSF decreases when the peak is offset from the center. The Γ correction factor varies from unity at perfect alignment up to 1.09 in the worst case for extreme offsets.

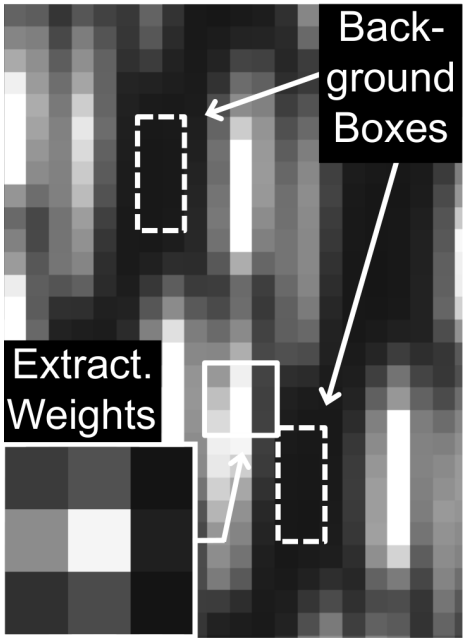

Figure 2.11 Diagram of the P1640 cube extraction method. We step down the spectrum in 0.03 μm increments, using the global focal plane solution to select a 3×3 pixel region for each *spaxel* in the cube. The sum of the extracted samples is weighted based on the fractional offset of the true extraction target point from the box center. In the example shown here, the weighting scheme (bottom left inset) captures the leftward skew of the spectrum cross section at this particular wavelength. The two dashed boxes outline the "dark" regions used to sample the local background level around each spectrum.

2.4.2.4 Spectral Calibration

For a given microlens, the separation between the extraction target points of the first and last channels—corresponding to $\lambda = 1.10\,\mu$m and $1.76\,\mu$m—is typically about 24 detector pixels. Since we use 3×3 pixel boxes to extract a signal for each of 23 channels spanning that length, the footprints of adjacent channels necessarily overlap. We have examined the effect of this by extracting data cubes directly from the laser calibration images (discussed in § 2.3.1). From these cubes, we compared the mean flux in neighboring cube channels. The results, plotted in Figure 2.12 for 1.25 μm and 1.58 μm emission, reveal the effective

filter shape of an individual data cube channel.

The cube channel filters exhibit a full width half-maximum value of ~ 70 nm at both J and H band. Knowledge of this profile is essential for comparisons between P1640 data and existing astronomical spectra. We cannot simply bin a reference spectrum to the channel spacing; we must also convolve it with the cube channel filter before comparing it to data cube measurements. Suppose an object appears in a data cube, and we carry out channel-wise photometry to find a spectrum $\mathcal{A}(w)$, $0 \leq w \leq 22$. To compare this meaningfully to an established spectrum, $\mathcal{B}(\lambda)$, acquired by some other instrument with wavelength bin width $\Delta\lambda$, requires two steps. First, we re-bin $\mathcal{B}(\lambda)$ to the cube channel interval, 0.03 μm, to form an intermediate-resolution spectrum $\mathcal{B}'(w)$:

$$\mathcal{B}'(w) = \begin{cases} \sum\limits_{\lambda=1.085+0.03w\,\mu\mathrm{m}}^{1.115+0.03w\,\mu\mathrm{m}} \mathcal{B}(\lambda)\Delta\lambda & 0 \leq w \leq 22 \\ 0 & \text{otherwise.} \end{cases} \tag{2.23}$$

We then convolve the intermediate-resolution spectrum $\mathcal{B}'$ with the cube channel filters $\mathfrak{F}_J(z)$ and $\mathfrak{F}_H(z)$. The filter functions are defined to follow the profiles shown in Figure 2.12 for $-3 \leq z \leq 3$ (so that $z = 0$ corresponds to the central peak of the filter), and are zero-valued outside that range.

$$\mathcal{B}''(w) = \begin{cases} \dfrac{\sum\limits_{z=-3}^{3} \mathfrak{F}_J(z)}{\sum\limits_{z=-w}^{3} \mathfrak{F}_J(z)} \sum\limits_{z=-3}^{3} \mathcal{B}'(w+z)\mathfrak{F}_J(z) & 0 \leq w < 10 \\ \dfrac{\sum\limits_{z=-3}^{3} \mathfrak{F}_H(z)}{\sum\limits_{z=-3}^{22-w} \mathfrak{F}_H(z)} \sum\limits_{z=-3}^{3} \mathcal{B}'(w+z)\mathfrak{F}_H(z) & 10 \leq w \leq 22 \end{cases} \tag{2.24}$$

The ratios in front of each convolution sum compensate for the effect of the spectrograph passband edges on the filtering (they are unity when w is at least three channels from both passband edges). The resulting spectrum, $\mathcal{B}''(w)$, is smoothed to the same resolution as the cube-derived spectrum $\mathcal{A}(w)$. If $A(w)$ has been corrected for the P1640 spectral response, then the two spectra can be directly compared, apart from some scale factor. If on the other hand, $\mathcal{A}(w)$ is a "raw" cube spectrum, with undetermined spectral calibration, and $\mathcal{B}''(w)$ refers to the same source, then it can be used to correct $\mathcal{A}(w)$—and, in general, any P1640 data cube, as described next.

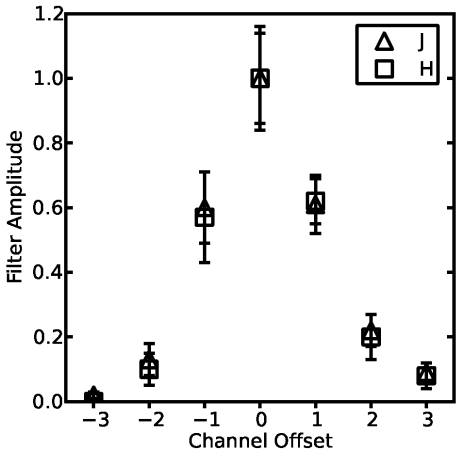

Figure 2.12 Normalized response of the P1640 cube extraction to 1.25 μm and 1.58 μm laser sources. These are the effective filter profiles assumed for cube channels in J and H band, respectively. The error bars indicate the standard deviation of the 100×100 spaxel measurement sample.

We characterize the wavelength-dependent sensitivity of P1640, or spectral response function, by comparing the "raw" data cube count values of an unocculted reference star (observed off-axis from the coronagraph focal plane mask) with its established near-infrared spectrum. In practice, we have chosen stars with spectra archived in the NASA Infrared Telescope Facility (IRTF) Spectral Library to calibrate our response (Rayner et al. 2009).

The spectral response function is determined by dividing the re-binned, smoothed reference spectrum ($\mathcal{B}''(w)$, in the notation above) by the spectrum of the same source derived from a P1640 data cube.

We measure the signal of the observed reference star by carrying out aperture photometry on each channel image making up the data cube, enclosing the third Airy ring. To capture the wavelength-dependent scaling of the coronagraph PSF, we linearly increased the photometric aperture radius from 13 to 20 spaxels across the passband. The resulting response curve for one calibration star, HD 75555 ($V = 8.1$; spectral type F5.5III-IV), is shown in Figure 2.13. The response curve shows the expected roll-off at the edges of the operating range due to telluric water absorption features. The valley centered near 1.4 μm is likewise due to water absorption between *J* and *H* band. The overall climb in the response towards longer wavelengths is caused by the wavelength-dependence of three effects in combination: the energy per photon as dictated by the Plank relation, $E = \frac{hc}{\lambda}$; detector quantum efficiency; and the transmission of the blocking filter at the IFU entrance.

We normalize the spectral response function to its mean value before storing it for general application to data cubes. The cube extraction pipeline loads one of these mean-normalized spectral response functions into memory before beginning the cube extraction routine. If the appropriate switch is set by the user, the pipeline will divide the spaxel values in each channel image by the corresponding response function value.

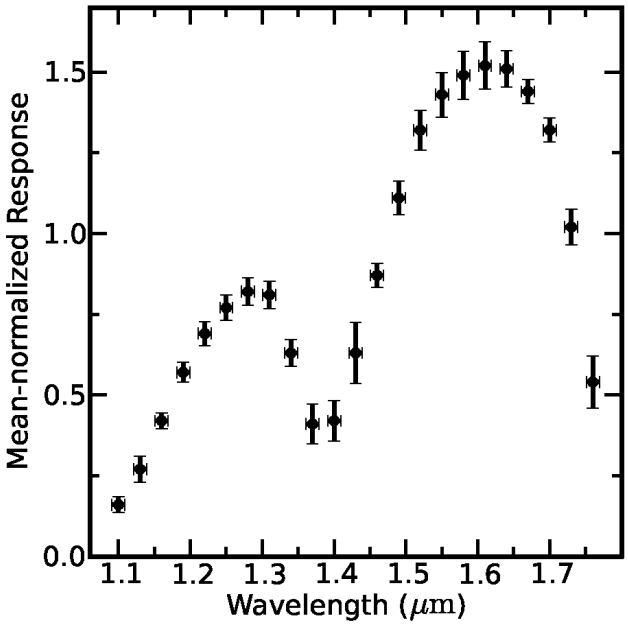

Figure 2.13 P1640 response curve, determined through a comparison between photometry on an unocculted star's data cube (HD 75555, in this case) with the established spectrum of the star archived in the Infrared Telescope Facility Spectral Library.

2.4.2.5 Error Sources

Uncertainty in the global spectrograph focal plane solution, the image registration, and the weighting function combine to contribute a pseudo-random error to each cube point, at a level of $\sim$ 5% of the spaxel value. We extracted cubes from the Moon calibration images to estimate the magnitude of this error. Since spatial amplitude variations are compensated for during extraction, ideally any given spatial cross-section of a cube extracted from a calibration image would appear flat. Instead, we observe a standard deviation of 3%, with some variation between channels and areas of the image.

There are also systematic errors caused by light from adjacent microlenses overlapping on the focal plane, which we refer to as cross-talk. The horizontal space between spectra on the focal plane is 3.3 detector pixels, and yet we know from the spectrograph

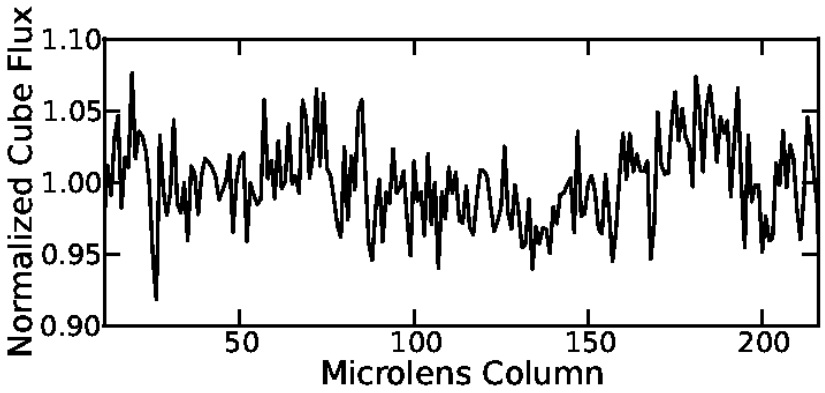

Figure 2.14 A row in a data cube extracted from a June 2009 Moon calibration image, with flux values normalized to unity. The scatter in flux across the row (here the standard deviation is 3%) reveals flux-proportional errors in the cube extraction.

PSF model (Figure 2.3) that about 10% of the downsampled PSF flux falls outside the central three columns. As a result, a small fraction of light from one microlens is inevitably counted during the extraction of a neighboring spectrum. Consider the spectrograph image cutout shown in Figure 2.11. For each channel of a given spectrum, you can attribute the dominant contamination to a different channel belonging to the neighboring spectrum positioned either above or below along the microlens column. We know from examining the laser calibration data cubes that the upper limit of the flux incorrectly extracted into a cube point is $\sim$ 5% of the cube value in a neighboring spectrum. In other words, suppose $\mathcal{C}(i_0, j_0, w_0)$ is the cube point whose contamination we are trying to assess. Based on our spectrum model, we can determine that some channel w_1 of microlens $(i_0, j_0 - 1)$ is the dominant contamination source for channel w_0 of microlens (i_0, j_0). Therefore, we estimate the cross-talk error $0.05\mathcal{C}(i_0, j_0 - 1, w_1)$, added in quadrature with the uncertainty described earlier. Using a table of established cross-talk channel pairs, we can repeat this error estimate for each channel of a spectrum of interest. The spectral response function

plotted in Figure 2.13 and the source spectrum plotted in Figure 2.15 reflect this analysis.

2.4.3 Pipeline Data Products

The PCXP stores the reduced data output in FITS files, and organizes them in a directory tree by object and date. Three channels from an example cube based on an occulted star observation are displayed in Figure 2.1. In addition to the normal cube extraction described in § 2.4.2, there are several other products the pipeline derives from the raw data. From the brightest stars, there is enough signal recorded in a single 7.7 second read to form a cube without using the full exposure time. One option of the pipeline takes advantage of this, checking if the V-band magnitude is less than 2.0, and if so then making cubes from each pair of consecutive reads in the NDR sequence. The resulting "read-wise" cubes have a speckle pattern resolved to a higher time resolution, which may eventually be exploited to improve speckle suppression. At the opposite time scale, the pipeline can form cubes from the mean of all spectrograph images acquired on the same data of a given target. The pipeline also forms "collapsed" images by summing all the channel images of a cube, as well as the subsets of channels corresponding to the J and H bands.

2.5 Example Spectrum Retrieval: Titan

To demonstrate the efficacy of our data extraction and calibration procedures, we apply them here to an observation of Saturn's moon Titan acquired on 2009 March 15. After locking the AO system on Titan, its image was positioned off-axis from the focal plane mask so that no part of the $1''$ disk was occulted by the coronagraph. We used the pipeline

to generate a data cube from a single 138 s exposure, calibrating the relative channel fluxes with the response function shown in Figure 2.13. Next, we averaged 1900 spaxels inside the resolved disk of Titan. After normalizing the disk-averaged spectrum to the mean channel flux, we compared it to unpublished data obtained by Emily Schaller two days earlier using the SpeX near-infrared spectrograph (Rayner et al. 2003) at the NASA Infrared Telescope Facility (IRTF). Following the procedure in § 2.4.2.4, we re-binned and smoothed the IRTF spectrum to match the resolution of the data cube (Equations 2.23–2.24). The resulting spectra are plotted in Figure 2.15. The near-infrared spectrum of the moon is marked by a series of broad CH_4 absorption troughs (Fink & Larson 1979). At the two albedo peaks in our passband, 1.3 μm and 1.6 μm, Titan's atmospheric opacity is low enough for the direct reflection of sunlight off the water ice surface to constitute the observed flux, rather than diffuse scattering in its stratospheric haze (Griffith et al. 1991).

We expect the disk-averaged spectra acquired on these two dates to be similar. As Titan rotates over a 16-day period, in synchronicity with its orbit around Saturn, the near-infrared albedo observed from Earth (through the 1.3 μm and 1.6 μm methane "windows") varies in a cycle with an amplitude on the order of 10%. This variation is caused by a change in surface features between the leading and trailing hemispheres (Lemmon et al. 1995). However, despite the 45 degree rotation of Titan with respect to Earth between the IRTF and P1640 observations, previous monitoring by several investigators indicates no significant albedo change between our specific pair of planetographic longitudes (197° and 243°) (Griffith et al. 1998). Furthermore, long-term monitoring of Titan's albedo only occasionally reveals deviations from predicted reflectivity due to transient cloud features (e.g.

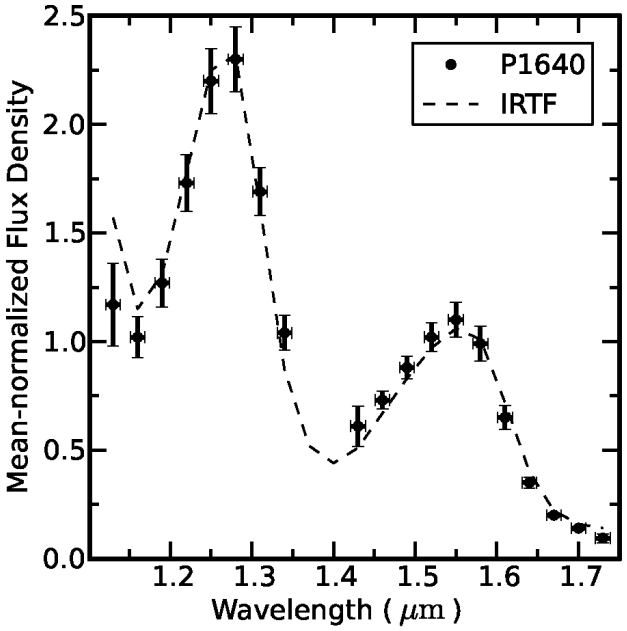

Figure 2.15 Disk-averaged spectrum of Titan extracted from a P1640 data cube, calibrated using the spectral response function in Figure 2.13. For comparison, a near-infrared spectrum of Titan acquired with IRTF/SpeX by Schaller is plotted alongside the P1640 data, after being binned and smoothed to the P1640 cube resolution. The IRTF/SpeX and P1640 Titan data were acquired two days apart, on 2009 March 13 and 15, respectively. Each spectrum is normalized to the mean of the points included in the plot. Channels 1, 10, 11, and 23 ($\lambda = 1.10\,\mu$m$, 1.37\,\mu$m$, 1.40\,\mu$m, and $1.76\,\mu$m, respectively) were excluded due to varying telluric water absorption.

Griffith et al. 1998; Schaller et al. 2009). The anticipated resemblance of the two spectra is confirmed in Figure 2.15: the average absolute difference between the IRTF and P1640 Titan data over the 19 channels used in Figure 2.15 is 7% of the mean flux, and most flux points agree within the error bars of the P1640 data. The only channel flux showing significant disparity with the IRTF data, centered at 1.13 μm, is located near the edge of a telluric water absorption trough, and therefore is more susceptible to calibration errors than most channels on the plot. For examples of M dwarf stellar spectra that have been measured from P1640 data cubes, see Zimmerman et al. (2010) and Hinkley et al. (2010).

2.6 Discussion

Starting from the economic constraint of limited detector area, the design of any integral field spectrograph must reach compromises between the competing parameters of spatial resolution, field of view, spectral resolution, and spectral range. For Project 1640, the need to Nyquist-sample the starlight speckle pattern inside the angular extent of the adaptive optics system "control radius" largely determined the balance of these tradeoffs. The other major factor was the overarching science goal of distinguishing astrophysically interesting features in the spectral energy distributions of young giant exoplanet atmospheres. Based on these considerations, the P1640 collaboration concluded on an IFU design that strongly favored a high density of spatial elements over spectral resolution, to a greater extreme than previous microlens-based integral field spectrographs. For example, the broadband mode of the TIGER IFU had 572 spatial elements dispersed at spectral resolution $R \sim 370$, and the broadband mode of the OSIRIS IFU has 1024 spatial elements dispersed at $R \sim 3400$ (Bacon et al. 1995; Larkin et al. 2006). P1640, by comparison, has 38,000 spatial elements with $R \sim 40$, corresponding to over a factor of 30 increase in spatial elements, and a similarly substantial reduction in spectral resolution. Only two other IFUs will join P1640 in this operating regime in the next year: GPI and VLT-SPHERE—both designed for exoplanet imaging.

Since the properties of P1640 data are unusual even in the context of preceding IFUs, the instrument commissioning has required development of novel extraction and calibration approaches. Consider that each detector pixel width spans approximately 27.5 nm in spectral dispersion—4% of the instrument passband—and that the physical length of an in-

dividual microlens spectrum's footprint is merely 0.5 mm at the focal plane. As such, great care has been required to accurately map the spectrograph focal plane data, in a manner that is resilient to subtle long-term changes in optical alignment. We described an answer to this problem in § 2.3, using a hierarchical fitting procedure to build a comprehensive, epoch-specific model of the full spectrograph focal plane. The last obstacle to securing the layout of the data, instrument flexure, must be dealt with individually for each exposure. Therefore, unlike the case of building the spectrograph focal plane model, we register each science spectrograph image "on the fly" inside the data pipeline, as explained in § 2.4.1.5.

The relatively long execution time required to build the spectrograph focal plane solution ($\sim$ 12 hours on a single high-performance workstation) means that it is sometimes necessary to rely on an outdated solution to extract data. Such will be the case, for example, during the first night of an observing run when the calibration Moon/sky image has not yet been acquired and fit. We know from the geometric evolution illustrated in Figure 2.7 that consequent errors in the positions of the spectra, along with other properties, will inevitably degrade the quality of the cube. However, for a preliminary inspection of data, and to check on instrument performance, the result will usually be acceptable. Recall that the spectrograph image registration uses a region of the image with the strongest signal to align the model. Therefore, under circumstances where the solution is old, the extraction will still tend to be fairly accurate near the brightest region of the image, but will progressively worsen towards the outskirts of the focal plane.

The main advantages of our weighted sum approach to IFU spectrum extraction, described in § 2.4.2.3, are simplicity and speed. Our reasoning behind using the spectrograph

PSF itself to shape the weighting function is that it mimics the cross-dispersion profile of the spectrum. This way, along the middle horizontal row of the 3×3 extraction box, we weight the detector samples by an estimate of their relative intensity (see Figure 2.11 for an example). Horne (1986) originally devised this strategy for extracting coarsely-sampled CCD spectra. He demonstrated that matching the weights to the expected cross-dispersion profile optimizes the fidelity of the extraction in the case where read noise is prevalent. This makes sense intuitively because we want detector samples with high count rates to have more influence than weak, noisy ones. Unlike the case of Horne's spectrograph, however, we are dealing with many closely packed spectra, and so we are forced to truncate our weighting area to a region smaller than the actual extent of the PSF. We attempt to account for this in the weighting formula in Equation 2.21. Since this correction depends not just on the shape of the PSF but also the target spectrum, it is necessarily only an estimate, and can contribute errors on the order of a few percent to the spaxel value.

As compared to the cross-dispersion axis, for the dispersion axis there is more freedom in the choice of extraction weights. The tradeoffs here are signal-to-noise ratio per channel versus spectral resolution. Ultimately, for any weighted sum approach, the spectral resolution is limited by the width of the monochromatic IFU response along the dispersion axis. The spectrograph PSF fitting result plotted in the right-hand panel of Figure 2.3 shows this is about 2 detector pixels for P1640, which translates to ~ 50 nm in the dispersion direction. For simplicity, we chose to remain with the PSF again to set the weights; the resulting cube spectra have a resolution of about 70 nm ($R \sim 20$). In the future, it would be worthwhile to experiment with a hybrid weighting function that combines the cross-

dispersion profile of the PSF with a different vertical profile, to investigate how much the spectral resolution can be improved. As one example of an alternative, Maire et al. (2010) propose extracting spectra from the GPI IFU by summing strictly along a single row/column of pixels in the cross-dispersion direction.

Another possible improvement to our data pipeline is a completely different extraction approach based on deconvolution or fitting. A well-designed fitting algorithm might disentangle the flux contributions of wavelengths with overlapping footprints. We have done a few experiments in this direction—for example, we applied the same MPFIT-based algorithm we used to model the microlens spectra in the Moon/sky calibration image (§ 2.3.2) to a science image. The results were of significantly poorer quality than our normal data cubes, partly as a consequence of not having the luxury to average the fit spectra over many microlenses, as we do with calibration images. In another program, two of our co-authors created a program that fits each spectrum cutout as a train of scaled PSFs, each one representing a different channel. While its implementation is not complete, this method shows promise of forming data cubes with slightly higher spectral resolution than the existing extraction. Since any fitting approach is inherently much slower than a weighted sum translation, one can imagine two cube extraction algorithms co-existing for different purposes: one as an offline procedure reserved for images of the greatest interest, and the other program applied to all P1640 data.

2.7 Conclusions

We have developed a collection of algorithms to reduce the data acquired by P1640, a coronagraphic integral field spectrograph designed for high contrast imaging. Our aim has been to describe our data pipeline software in enough detail that upcoming microlens-based imaging spectrograph projects can take advantage of our experience in treating closely packed, coarsely sampled spectra.

An essential element of our approach is an empirical model of the spectrograph focal plane image, based on calibration exposures in which the entire microlens array is illuminated, in turn, by broadband and monochromatic light. To derive a solution specific to each observation epoch, we fit a set of parameters describing each microlens spectrum (position, tilt, height, and overall signal amplitude). We use the resulting table of solved parameters to determine the extraction location on the focal plane for any given combination of microlens and wavelength, and hence build the data cube.

We implement the cube extraction with a weighted sum that optimizes the signal-to-noise ratio by mimicking the expected cross-dispersion profile, as constrained by the sub-pixel spectrograph image registration. Sources of error in the final data cube are cross-talk between adjacent microlens spectra, uncertainty in the spectrograph focal plane model, uncertainty in sub-pixel registration, and uncertainty in the determination of extraction weights. Nevertheless, based on an observation of Saturn's moon Titan, we have demonstrated our ability to retrieve strong-featured near-infrared spectra to $\sim 5\%$ accuracy. As our methods for handling this new form of data evolve, we expect P1640 to continue its pioneering role in high contrast astronomy.

Chapter 3

Parallactic Motion for Companion Discovery: An M-Dwarf Orbiting Alcor[†]

Neil Zimmerman, Ben R. Oppenheimer, Sasha Hinkley, Douglas Brenner, Ian R. Parry, Anand Sivaramakrishnan, Lynne Hillenbrand, Charles Beichman, Justin R. Crepp, Gautam Vasisht, Rick Burruss, Lewis C. Roberts Jr. David L. King, Rémi Soummer, Richard Dekany, Michael Shao, Antonin Bouchez, Jennifer E. Roberts & Stephanie Hunt

ABSTRACT

The A5V star Alcor has an M3-M4 dwarf companion, as evidenced by a novel astrometric technique. Imaging spectroscopy combined with adaptive optics coronagraphy

[†]Published in ApJ, Vol. 709, Issue 2, pp. 733-740 (2010)

allowed for the detection and spectrophotometric characterization of the point source at a contrast of $\sim$6 J- and H-band magnitudes and separation of $1''$ from the primary star. The use of an astrometric pupil plane grid allowed us to determine the projected separations between the companion and the coronagraphically occulted primary star to ≤ 3 milliarcsecond precision at two observation epochs. Our measurements demonstrate common parallactic and proper motion over the course of 103 days, significantly shorter than the period of time needed for most companion confirmations through proper motion measurements alone. This common parallax method is potentially more rigorous than common proper motion, ensuring that the neighboring bodies lie at the same distance, rather than relying on the statistical improbability that two objects in close proximity to each other on the sky move in the same direction. The discovery of a low-mass ($\sim$0.25 $M_{\odot}$) companion around a bright ($V = 4.0^{m}$), nearby ($d = 25$ pc) star highlights a region of binary star parameter space that to date has not been fully probed.

3.1 Introduction

High-contrast imaging is a technique being developed for the study of faint objects in the vicinity of the closest stars to the Sun, to advance our understanding of binary stars, substellar companions, exoplanets, and circumstellar disks. For a recent discussion of this subject, see Oppenheimer & Hinkley (2009). In general, the detection of a point source next to a bright star is insufficient evidence to establish a physical association. Over the years, a number of claims of companion detection relying only on single epoch observations, and a measurement of color have subsequently been disproved through astrometric measure-

ments. For example, the companion reported in the McCarthy et al. (1985) study of VB 8 was subsequently shown to actually be a background star (Perrier & Mariotti 1987). As a result, researchers in this area have been careful to confirm through astrometry that any putative companion found shares the proper motion of the primary star, with orbital motion generally measured after several years of observations.

In fact, most of the stars in surveys for faint companions exhibit appreciable parallactic motion in addition to their proper motion. For example, over the course of one year, a star at a distance of 100 pc will appear to trace an ellipse in the sky with a circumference of roughly 60 mas. The segment of the curve traversed by this star over an observation baseline of ~ 3 months provides an opportunity to discriminate against background stars in the same manner enabled by common proper motion analysis over longer time scales (e.g., Mugrauer & Neuhäuser 2005). If the supposed companion maintains the same offset from the primary star over the duration of time between the observation epochs—to within an appropriate tolerance set by the upper limit of hypothetical orbital motion—then a strong argument can be made for the physical association of the two objects.

We note that the use of parallactic motion discrimination requires higher precision astrometry than has typically been possible in high contrast imaging. For example, Thalmann et al. (2009) achieved a 10 mas level of precision and managed a detection of common parallax. Here we achieve a factor of three better precision to confirm an object's physical association. Other coronagraphs have not yet demonstrated similar levels of relative astrometry, with tens to hundreds of milliarcsecond astrometry being typical. This is particularly true when no other stars with well-established astrometric parameters lie in the field

of view—a common situation that most high-contrast imaging devices face into the future (we note that with the aid of a fixed background star, Neuhäuser et al. (2008) measured a common parallax for GQ Lupi and its companion).

We have used the common parallax method to discover and confirm a companion orbiting the star Alcor (also known as HD 116842 and HIP 65477; J2000 coordinates $\alpha = 13^{h}25^{m}13.538^{s}, \delta = +54^{\circ}59'16.65''$ in Perryman et al. (1997)). Independently, Mamajek et al. (2010) imaged this same companion in the infrared M band, though their single epoch of data did not permit them to confirm the physical association with Alcor through astrometry. See the Appendix for a discussion of Alcor's rich role in the early stage of modern astronomy. While our astrometry measurements alone permit concrete affirmation of companionship, we also obtained low-resolution spectra and photometry in the *J* and *H* bands, completing the portrait and identifying the companion as an M3-M4 main sequence star of roughly 0.25 $M_{\odot}$. Although Alcor has been surveyed for possible companions in the past with speckle interferometry, the dynamic range of this technique at angular separations beyond several times the instrument's Rayleigh resolution limit is inferior to that obtainable with adaptive optics coronagraphy, as used in this study. For example, when McAlister et al. (1993) conducted speckle interferometry observations of Alcor with the 3.6 m Canada-France-Hawaii Telescope, their dynamic range was limited to 3 magnitudes at separations $> 0.04''$, and consequently could not have detected the object we describe in this article. On the other hand, Lyot coronagraphs coupled with adaptive optics systems can routinely attain dynamic ranges of ~ 10 magnitudes at a separation of $1''$ from the target star (Oppenheimer & Hinkley 2009). Although few low-mass stellar companions to A stars like Alcor have

been imaged, with the increasing prevalence of high contrast imaging surveys, recently other systems of similar nature have been found (e.g. Hinkley et al. 2010; Kouwenhoven et al. 2005).

Alcor is a member of the nucleus of the Ursa Major (UMa) moving group. With a spectral type of A5V, it is one of seven main sequence A stars with high confidence association to the group, based on kinematic and spectroscopic indicators (King et al. 2003). Despite the long history of studies of the UMa group, there remains a considerable uncertainty in the age of these stars. After compiling the photometry of a kinematically selected sample and comparing the resulting color-magnitude diagram with stellar evolution models, King et al. (2003) arrive at an age estimate of 500 ± 100 Myr for the group. Another recent study found that the color-magnitude diagram of the UMa group was best fit with an isochrone corresponding to an age of 400 Myr (Castellani et al. 2002). It should be noted that both of these age estimates are greater than the 300 Myr ages obtained from earlier work (e.g. Soderblom & Mayor 1993).

For several reasons, Alcor is an attractive target for high contrast imaging surveys. First, the combination of close distance from the Sun, 24.9 ± 0.4 pc (Perryman et al. 1997), and its relatively young age (as mentioned above) increases the probability of detecting a previously unknown substellar companion: stars closer to the Sun have companions with larger angular separations on average, and, because substellar objects cool as they age, younger objects are easier to detect. (See, for example, the cooling characteristics in Burrows et al. (1998).) Furthermore, theoretical models of fragmentation in circumstellar disks suggest an abundance of low mass companions around A stars (Kratter et al. 2010). Indeed,

recent direct imaging discoveries of substellar companions support this hypothesis (Marois et al. 2008b; Kalas et al. 2008).

The high apparent brightness of Alcor ($V = 4.0^{\mathrm{m}}$) relative to other nearby stars is yet another agreeable feature. High contrast imaging surveys rely on the wave front correction provided by adaptive optics (AO) systems to attain large dynamic ranges within close angular separation of the target star. When the AO system uses on-axis light rather than an artificial guide star to measure the wave front errors caused by the atmosphere—as is the case of our study—the quality of the correction depends strongly on the brightness of the target star (Troy et al. 2000). For the above reasons, we chose to include Alcor in the Project 1640 survey of nearby stars.

3.2 Observations

Project 1640 is a near-infrared, integral field spectrograph situated behind an Apodized Pupil Lyot Coronagraph (APLC) (Hinkley et al. 2011b). During operation, Project 1640 is mounted behind the PALAO adaptive optics system (Dekany et al. 1997) on the the 200" Hale Telescope at Palomar. The APLC consists of a pupil plane apodizer, a hard-edge focal plane mask, and a Lyot stop. The prolate apodization function and other masks are optimized to deliver broadband quasi-achromatic starlight suppression (Soummer 2005; Soummer et al. 2009). The APLC also includes a fine guidance system and an atmospheric dispersion corrector. In addition to the apodizer, another novel feature present in the pupil plane of the APLC is an astrometric grid that serves to indicate precisely the position of the star when it is occulted by the 370 milliarcsecond diameter focal plane mask.

The grid of thin opaque lines in the pupil plane produces a periodic linear array of faint images of the obscured star along the symmetry axes of the grid, with the star itself at the intersection of two the linear arrays (Sivaramakrishnan & Oppenheimer 2006; Marois et al. 2006b). These satellite spots form an array of stellar PSFs with angular spacing λ/d (d being the line spacing, as projected back to the entrance pupil, λ the wavelength of the light forming the image), and brightness approximately $(t/d)^2$ relative to the central unocculted PSF (where t is the line thickness). We arranged to have the closest four satellite PSFs miss the focal plane mask but still lie within the field of view, to provide stable astrometric fiducials visible in every coronagraphic image.

Upon exiting the coronagraph, the optical beam passes through an array of 200 x 200 lenslets in the spectrograph. A dispersing prism produces an individual spectrum corresponding to each lenslet on the 2048 x 2048 pixel infrared detector, with a spectral resolution of $\lambda/\Delta\lambda \sim 30$ between 1.10 μm and 1.76 μm (J and H bands). The detector subtends a field of view approximately $4''$ in diameter (Hinkley et al. 2011b).

Table 3.1 summarizes our observations of Alcor. On 2009 March 16 we obtained 1912 seconds of data with Alcor occulted by the coronagraph, at an airmass of 1.10, under seeing conditions near $1''$. The adaptive optics system corrected this seeing such that images at 1.65 μm exhibited a Strehl ratio of roughly 50%. The pupil plane grid used during this observation produced four astrometric spots in the image at a brightness of $\sim$8 magnitudes fainter than the target star. A point source was immediately noticeable $\sim 1''$ from Alcor in the raw data. We observed Alcor again with good atmospheric conditions on 2009 June 27, this time obtaining a total of 293 seconds of occulted data. Again the point source of

Table 3.1. Summary of Project 1640 observations of the Alcor System.

Mean UT Date	Besselian Year	τ_{exp} (s)	λ (μm)	ρ (mas)	P. A. (Deg. East of North)
2009 March 16 10:35	2009.20469	1912	1.10-1.76	1050 ± 1	206.5 ± 0.1
2009 June 27 3:51	2009.48593	293	1.10-1.76	1043 ± 1	207.1 ± 0.1

interest was visible, in roughly the same location with respect to Alcor. During the June observations we used a pupil grid with thicker reticle wire, providing brighter astrometric spots, $\sim$6 magnitudes fainter than Alcor.

3.3 Data Processing

The Project 1640 integral field spectrograph (IFS) produces information with three dimensions simultaneously: two spatial and one spectral. Therefore, the most natural way to view the data is in the form of a cube where each slice is an image of the target field in a particular wavelength channel. We devised a data pipeline to automate the process of converting the detector images—each containing a mosaic of 4×10^4 closely packed spectra—into a data cube. The complete description of the details of this technique will be published elsewhere. Here we provide a general overview of how it works.

An essential component of the cube extraction is a library of images made by illuminating the IFS with a tunable laser. Each of these laser images contains the response of the IFS to a specific wavelength: a matrix of illuminated spots corresponding to the individual lenslets of the IFS. Effectively, they are keys showing what regions of the 4×10^4 spectra landing on the detector correspond to a particular central wavelength. The data pipeline uses the laser images to extract the science data and map them onto a cube, forming twenty-

three images at wavelengths between 1100 and 1760 nm, each with a bandwidth of 30 nm. In addition to the mapping between the detector plane and the data cube, the Project 1640 data pipeline carries out numerous steps to prepare the data for analysis, including bias/dark-subtraction, bad pixel correction, and flat-fielding.

Figure 3.1 shows the 1.61μm slice of a data cube formed from our 2009 June 27 data. It is the result of 40 detector reads, each of duration 7.7 seconds, for a total integration time of 293 seconds. The four astrometric spots are visible on the peripheral of the image, while the point of source interest is detected south-west of the occulting mask. We aligned and co-added all the data from each epoch, producing one final data cube representing each epoch.

In the rest of the article we refer explicitly to "lenslet pixels" to describe the pixels comprising the data cube, to avoid ambiguity with the pixels on the detector of the IFS. Since each lenslet pixel constitutes a measurement of flux from an area element of the sky within a certain wavelength range, it can be treated in the same manner as the pixel of an ordinary digital image. Our analysis is done strictly on the data cubes that have already been extracted from the detector images, so the detector pixels are absent from further discussion.

3.4 Photometry

In each spectral channel of the 2009 March 16 data cube, we performed aperture photometry on the putative companion. The residual light from the primary star significantly contaminated our image of the source. One component of this noise is in the form of speckles,

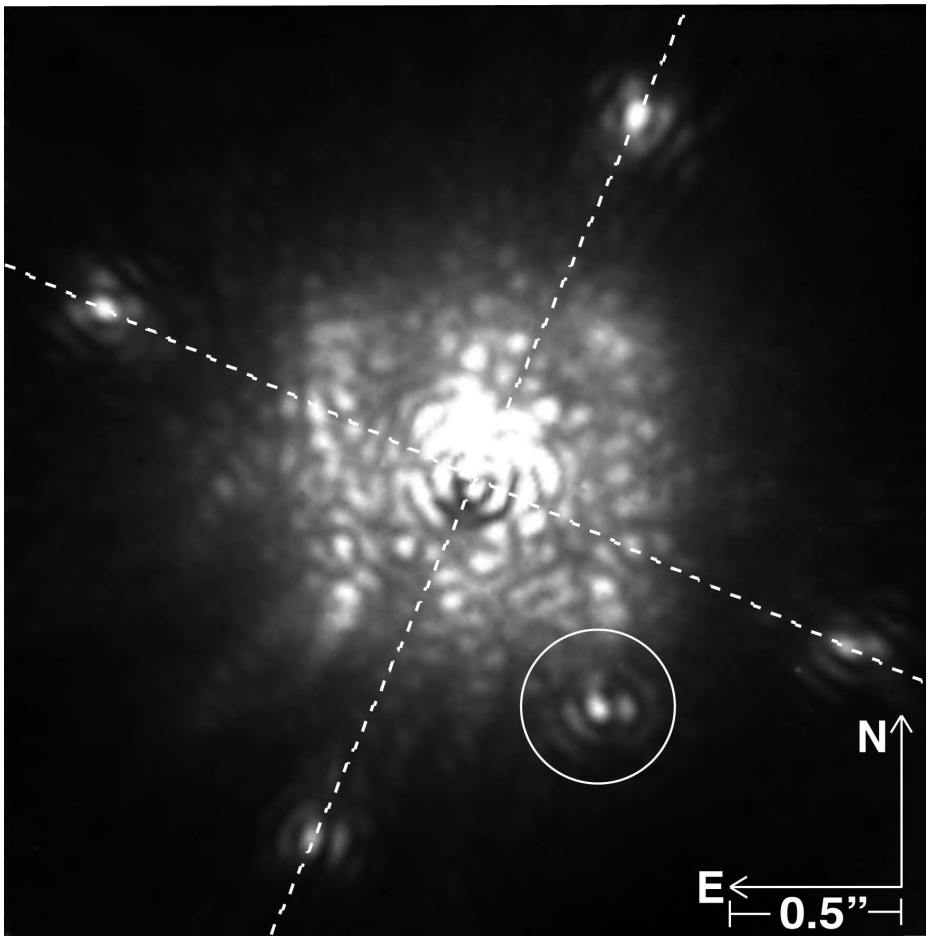

Figure 3.1 Coronagraphic image of Alcor obtained in June of 2009. This the slice of the data cube corresponding to central wavelength λ = 1.61 μm. The dashed lines illustrate the intersection of the lines between the astrometric spots, indicating the position of Alcor behind the occulting mask. Coincidentally, the astrometric spots are approximately 6 magnitudes fainter than the occulted star, similar to the brightness of the companion. The companion is the circled point source south-west of the image center.

which are not distributed in a smooth, easily modeled fashion (Racine et al. 1999; Perrin et al. 2003; Aime & Soummer 2004; Hinkley et al. 2007; Soummer et al. 2007). Numerous efforts are underway to develop algorithms that remove speckles from integral field spectrograph data by exploiting their chromatic properties (e.g. Sparks & Ford 2002). However, these speckle suppression techniques have not yet matured enough to apply to data from

an instrument such as ours without also altering the measured flux of true point sources. To minimize the effect of residual light from the primary star on our measurements, we counted the signal only in the core of the point spread function, even though up to two Airy rings of the source diffraction pattern are apparent in the data (as in Figure 3.1). Since the point spread function scales with wavelength, we used a different photometric aperture size for each half of the operating band to match the core size. For the first 11 channels (central wavelengths 1.10 μm-1.40 μm), we measured the flux in a circle of radius 3 lenslet pixels, and used a 4 lenslet pixel radius circle for channels 12-23 (central wavelengths 1.43 μm-1.76 μm).

In each channel of the data cube, the contaminating light from the primary star contributed $\sim$40-50% of the flux counts within the core photometric aperture. To account for this, we subtracted a "background" estimate formed from the median of pixel values in the annulus between 16 and 19 lenslet pixels from the center of the source. The 16 lenslet pixel inner radius of this background annulus is outside the detected diffraction pattern of the point source of interest.

The uncertainty in the assumed level of contaminating light from Alcor based on the annulus median is the dominant source of error in the photometry. We estimated the uncertainty in the assumed contamination by measuring the scatter in the median values of carefully chosen patches of the channel images. These patches were at nearly the same lenslet pixel separation from Alcor as the putative companion PSF, contained within the 16-19 pixel "background" annulus (so that they were beyond the influence of the putative companion PSF), and had the same area as our core photometric aperture. In other words,

we based our uncertainty in the subtraction of the primary star's contribution by examining the behavior of its residual light in parts of the image that are subject to similar contamination to the core photometric aperture. We find the resulting error remains $\sim$5% of the companion signal across the band.

We derived *J*- and *H*-band fluxes of the putative companion using a reference star observation to calibrate the photometry. On 2009 March 14, two days before our first epoch of Alcor data, we obtained a 7 second unocculted exposure of HD 107146/HIP 60074 (apparent magnitude V = 7.04, spectral type G2V) at an airmass of 1.05 under similar observing conditions. Even though HD 107146 has a known debris disk, it is optically thin and only detected near our instrument's wavelengths in Hubble Space Telescope data (Ardila et al. 2004). The HST data show scattered light distributed in a ring of inner radius $3''$, which is outside our field of view and far beyond our $\sim 0.1''$ photometric aperture.

We carried out aperture photometry on the point spread function in the HD 107146 data cube in an identical fashion as for the source in the Alcor image, using the same aperture and background annulus sizes. In the 2 Micron All Sky Survey (2MASS) Point Source Catalog (Cutri et al. 2003), HD 107146 has *J*- and *H*- band photometry listed as 5.87$\pm$0.02 and 5.61$\pm$0.02, respectively. We summed the core fluxes of the point source of interest and HD 107146 in the channel ranges corresponding to the 2MASS *J* and *H* filters (1.13 μm-1.34 μm, and 1.46 μm-1.73 μm, respectively). Subtracting the raw magnitudes of the HD 107146 *J* and *H* sums from the 2MASS magnitudes, we derived correction magnitudes for each filter. Applying those corrections to the channel sums of the putative companion, we arrived at the broadband fluxes listed in Table 3.2.

Table 3.2. Near-infrared photometry of Alcor B.

Band	m	M
J	9.95 ± 0.06	7.97 ± 0.06
H	9.56 ± 0.06	7.58 ± 0.06

We estimated the probability of a star with matching photometric properties unassociated with Alcor coinciding with our field of view. One way to do this is to determine the surface density of point sources that have fluxes within the two-sided 5σ confidence interval of our J- and H-band magnitudes, corresponding to flux bounds 25% above and below our stated measurements. We queried the 2MASS Point Source Catalog for the number of J and H-band point sources in the $2^\circ \times 2^\circ$ area centered on Alcor's coordinates, separated into one magnitude-wide bins extending between magnitudes 8 and 16. A linear regression fit to the logarithm of the source count as a function of magnitude yields the relations $\log_{10}(J\text{-band sources deg}^{-2}) = -1.764 + 0.284 m_J$ with a r.m.s. residual of 0.167, and $\log_{10}(H\text{-band sources deg}^{-2}) = -1.604 + 0.284 m_H$ with a r.m.s. residual of 0.090. Integrating these point source surface density relations between the 5σ flux boundaries of the supposed companion, $9.71 \leq m_J \leq 10.26$ and $9.32 \leq m_H \leq 9.87$, we arrive at J-band and H-band point source surface densities 3.9 deg^{-2} and 4.2 deg^2, respectively. Taking the larger of these two surface densities, 4.2 deg^{-2}, and multiplying by our $4'' \times 4''$ field of view, we expect 5.2×10^{-6} sources matching the photometric characteristics of the supposed companion in a given $4'' \times 4''$ field of view in this part of the sky. Multiplying this by 100 to roughly account for the number of stars we have surveyed so far with null detections of stellar companions, we arrive at a posteriori probability of 0.05% that the source is unas-

sociated with Alcor. Later in this article we will demonstrate how our astrometry reduces this probability to an even less significant quantity. With that knowledge in hand, we hereafter refer to the point source of interest as Alcor B, following the traditional nomenclature of directly imaged companions.

The parallax distance modulus of Alcor is 1.98^m, so to place Alcor B at the same distance implies it has absolute magnitudes $M_J = 7.97 \pm 0.06$ and $M_H = 7.58 \pm 0.06$. Henry & McCarthy (1993) derived empirical mass-luminosity relationships for stars with masses between $0.18M_\odot$ and $0.50M_\odot$. When we we apply these to our absolute *J*- and *H*- band magnitudes, and take into account the variance inherent to the model and our own photometric uncertainty, we calculate mass estimates of $0.26\pm^{0.10}_{0.07}$ $M_\odot$ and $0.21\pm^{0.04}_{0.03}$ $M_\odot$, from the *J*- and *H*-band luminosities, respectively. When we compare our fluxes to theoretical mass-luminosity models computed specifically for 600 Myr-old stars by Baraffe et al. (1998), similar to the published age estimates of Alcor, we find masses of $0.27M_\odot$ and $0.25M_\odot$, respectively. According to the mass-spectral class relationship for low mass stars derived by Baraffe & Chabrier (1996), a star with a mass between $0.2M_\odot$ and $0.3M_\odot$ indicates a spectral type in the range from M2V to M3.5V.

3.5 Spectroscopy

We extracted a low-resolution spectrum of the stellar companion from the IFS data. Again, we used the star HD 107146 as a reference source. As stated above, even though HD 107146 has a disk, it is faint and outside our field of view. Furthermore, the star lacks the excess emission that some disk hosts possess at 10 μm (Metchev et al. 2004), so to the best

of our knowledge, the spectrum is ordinary for a star of its class in our wavelength regime.

We began the spectral calibration by determining channel-wise corrections for the wavelength-dependent transmission of the atmosphere and instrument. To do this, we made the assumption that at the spectral resolution of our data cube ($\lambda/\Delta\lambda \sim 30$), and within our photometric errors, the spectrum of HD 107146 matches that of a typical G2V star. We compared our raw spectrum of HD 107146 with the measurement by (Rayner et al. 2009) of the near-infrared spectrum of HD 76151, another G2V star. The HD 76161 data is part of a suite of reference stellar spectra collected at NASA's Infrared Telescope Facility (IRTF). We binned the publicly archived HD 76151 spectrum to our spectrograph's resolution, divided it into our raw HD 107146 spectrum, and mean-normalized the result to obtain our response vector.

We obtained our raw spectrum of Alcor B by carrying out aperture photometry on the reduced data cube in the same manner as described in the Photometry section: counting the signal in an aperture containing the core of the PSF and subtracting the median of an annulus around the source multiplied by the aperture area. As before, our photometric errors were dominated by the uncertainty in the annulus estimate of Alcor's residual light in the companion photometric aperture, which includes a smooth halo and a speckle component.

We divided our raw Alcor B spectrum by the response vector to obtain the calibrated spectrum of the companion plotted in Figure 3.2. In our plot we omit the five channels of our spectral range that are strongly subjected to variable telluric absorption, those with central wavelengths 1.10 μm, 1.37 μm-1.43 μm, and 1.76 μm. The spectrum data points are normalized to the mean of the included channels.

We compared the spectrum of Alcor B with a broad range of examples of M-dwarf spectra from the IRTF Spectral Library (Rayner et al. 2009). In addition, we compared our companion spectrum with that of the giant star in the IRTF Spectral Library with the closest $J-H$ color, HD 108477, a G4III star with a 2MASS $J-H$ color of 0.34. After re-binning all of these comparison spectra to our data cube's spectral resolution, we normalized them and calculated the root mean square differences from the Alcor B spectrum. The spectra of three of these reference spectra are plotted alongside the Alcor B data in Figure 3.2. Of all of the spectra compared, the two closest matches to Alcor B are the M3.5V star Gl 273 and the M4V star Gl 213, both with root mean square residuals of 4%. Although the shape of the G4III giant spectrum is qualitatively different from the Alcor B data, particularly in terms of the slope across H band, its fit has a r.m.s. residual of only 5%. This serves to indicate that at this spectral resolution there is ambiguity in discriminating between G-giant and M-dwarf stars of similar color.

3.6 Astrometry

In each channel of the data cube, the intersection of the two perpendicular lines formed by the four astrometric grid spots determines the location of Alcor on the lenslet array (Figure 3.1). We compared these locations with the directly measured position of the companion in the data to measure the relative offset at each epoch. Due to a slight residual atmospheric dispersion causing an apparent drift in the position of the star by $\sim$2 lenslets over the wavelength range in the data cube, we only compared the spot intersection with the position of the companion measured within the same channel. The companion and the

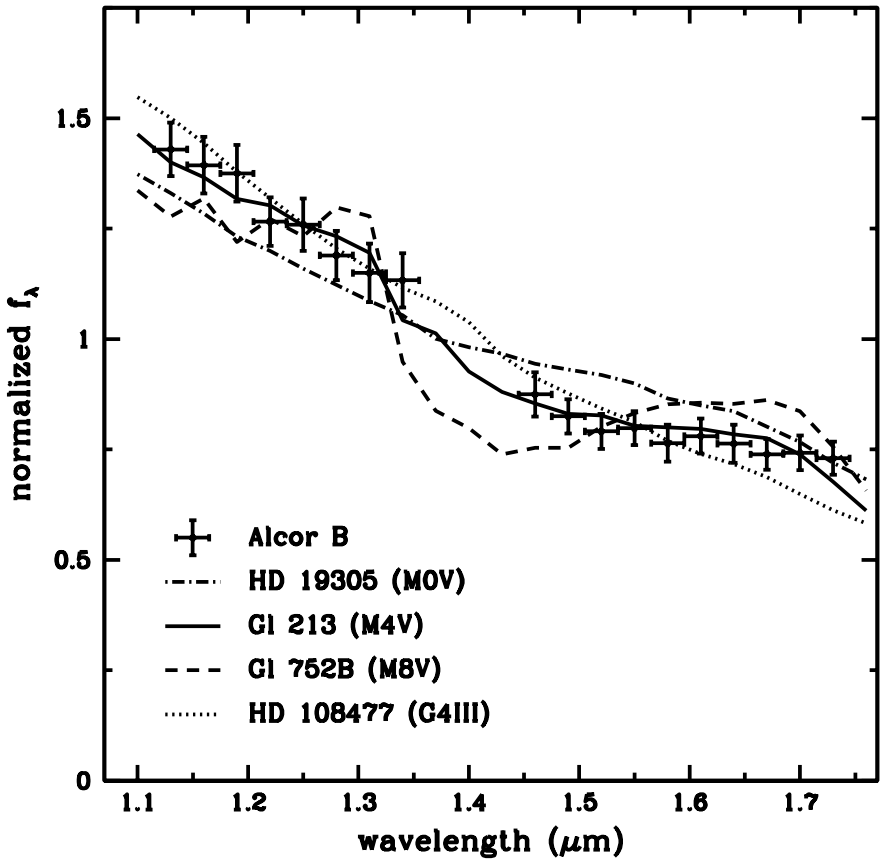

Figure 3.2 Spectrum of Alcor B extracted from the 2009 March data, compared with three examples of M-dwarf spectra and a giant spectrum whose $J - H$ color matches the photometry of the companion.

grid spots have strongest detections in a subset of cube channels in the *H* band, enabling the most accurate position determination at those wavelengths. These are also the wavelengths at which the atmospheric dispersion corrector is optimized. In addition, as is generally the case, the wave front correction of the AO system is better at *H* band than in *J* band. Therefore, we used only the five channels from 1.55 μm to 1.67 μm—those spanning the H-band transmission peak—to deduce the relative offsets at each epoch. We measured the positions of the companion and the grid spots in the data cubes by fitting Gaussian profiles

to the point spread functions. For each epoch, we took the mean of the offsets between the grid spot intersection and the companion PSF in the five aforementioned channels to arrive at our final estimates. We then applied the Student's t distribution (as appropriate when estimating a mean from a sample of five measurements—see Dean & Dixon (1951)) to derive 68% confidence intervals based on the standard deviation of the offset components between the channels.

To convert the lenslet pixel offsets into angular offsets oriented with equatorial coordinates, we applied our plate scale of 19.2 ± 0.1 mas/lenslet, and compensated for the rotation of our detector (the columns of the extracted data cubes are oriented $70.6 \pm 0.1^{\circ}$ counter-clockwise with respect to north). Both the plate scale and rotation were derived from a series of observations of calibration binary systems with Grade 1 orbit solutions in the USNO Sixth Orbit Catalog (Hartkopf et al. 2001) between July 2008 and March 2009. Standard errors were propagated through all calculations to reflect 68% confidence intervals in the error bars. In Table 3.3 we list the resulting offset components between Alcor B and its host star.

As described in the Photometry section, if we consider only our photometric measurements of the putative companion, we are left with a small possibility ($\sim 0.05\%$) that it is an unassociated star coinciding with our line of sight. Now, with our astrometry, we can rule out this possibility to a stronger degree, in order to affirm the physical association with Alcor.

First, as illustrated in Figure 3.3, we can rule out the simple notion that the supposed companion is actually a distant background star lacking significant proper or parallactic

motion—one that is, for our purposes, fixed on the sky. For example, one could imagine a luminous star at a distance of $\sim$1 kpc, whose parallactic motion between our two observations is only $\sim$1.5 mas, and whose projected space motion also happens to be near or below our astrometric precision. By contrast, over our 103-day baseline, the parallactic and proper components of Alcor's motion (see Table 3.4) resulted in a displacement with a magnitude of 34 mas. Because our two images remained centered on Alcor over the course of its motion, a fixed background star in our data would appear to shift about 34 mas relative to Alcor. More specifically, since the overall apparent motion of Alcor between our observations was 22.7 mas west and 25.2 mas south, a fixed background star lying south-west of Alcor would have shifted 22.7 mas east relative to Alcor (decreasing the magnitude of its offset from Alcor in Right Ascension), and 25.2 mas north relative to Alcor (decreasing the magnitude of its offset from Alcor in Declination). The arc labeled $(\mu+\pi)_{BKG}$ in Figure 3.3 represents this circumstance. Instead, we observed a westward motion of 6.0 ± 4.3 mas relative to Alcor and a relative northward motion of only 10.9 ± 2.3 mas (the two positions are labeled "March" and "June" in Figure 3.3). So the observed motion is inconsistent with a background star exhibiting a low apparent motion on the order of several milliarcseconds or less.

Now we consider the case of a distant background star that does exhibit significant apparent motion, in a such a way that matches the observed displacement of the companion star between our observation epochs. The least luminous giant with consistent $J-H$ color, a star of type G2III, would have to be at a distance of about 740 pc in order for its apparent magnitude to be consistent with our photometry. By combining our measurement of the

change in Alcor B's offset from Alcor A and our knowledge of the apparent motion of the primary star, we can deduce the absolute motion of the putative companion on the sky, decoupled from Alcor: 28.6 ± 4.3 mas west and -14.4 ± 2.3 mas south. At a distance of 740 pc, the expected parallactic motion between our observation epochs is 1.9 mas west and 0.7 mas south. Then, a proper motion of 26.7 mas west and 13.7 south is needed to make up for the difference from the observed apparent motion. We compute the space velocity from this assumed proper motion and distance using the formulas described in Johnson & Soderblom (1987). Assuming zero radial velocity, this star would need a galactic space velocity of U = -150 km s^{-1}, V = -300 km s^{-1}, and W = 130 km s^{-1} to be consistent with the apparent motion we measure. The largest component of this space velocity, V, indicates a strong retrograde galactic orbit. For more luminous giant stars, the necessary space velocities grow to even more unlikely values—a K1III giant, for example, would have need a V component of -600 km s^{-1} to be consistent with our astrometry. In that case, V is within the range of estimates of the local escape speed of the galaxy (e.g., 498 km $s^{-1} < v_{esc} <$ 608 km s^{-1} from Smith et al. (2007) and 489 km $s^{-1} < v_{esc} <$ 730 km s^{-1} from Kochanek (1996)).

The only plausible scenario remaining, that we have in fact discovered a low-mass companion to Alcor, can be checked by comparing the measured relative motion to Alcor with an estimate of the upper limit on the orbital motion a true companion would exhibit between our two observation epochs. The empirical mass-luminosity relation for intermediate-mass stars of Malkov (2007) implies a mass of $1.8 M_\odot$ for the A5V primary star, given its absolute magnitude $M_V = 2.01$. Assuming a mass of 0.25 $M_\odot$ for the com-

Table 3.3. Relative Astrometry of Alcor B

Component	2009 March 16	2009 June 27	Change
East offset (mas)	-470.3 ± 3.1	-476.3 ± 2.9	-6.0 ± 4.3
North offset (mas)	-939.1 ± 1.7	-928.2 ± 1.5	10.9 ± 2.3

[a]The equatorial coordinate offsets of Alcor B relative to its host star on 2009 March 16 and 2009 June 27 (Besselian dates 2009.2047 and 2009.4859, respectively) followed by the change between the two epochs.

panion, a circular orbit of the projected radius 26 AU ($1.05''$ at 24.9 pc) would have a period of roughly 93 years, resulting in an apparent motion of $\sim$20 mas if it were orbiting face-on. In fact, the motion we detected is smaller than this, but any inclination, eccentricity, or different semi-major axis in the orbit could change the expected orbital motion. However, most importantly, the apparent motion of Alcor B that we do detect is consistent with plausible orbital motion around Alcor. A circle illustrating the range of possible orbital motion with respect to the position of Alcor B at the first observation epoch is shown in Figure 3.3.

Table 3.4 Apparent Motion of Alcor Between Observation Epochs

Component	Change (mas)
$\Delta\text{East}_{\text{PM}}$	33.9
$\Delta\text{North}_{\text{PM}}$	-4.8
ΔEast_{π}	-56.5
ΔNorth_{π}	-20.4
$\Delta\text{East}_{\text{PM}+\pi}$	-22.7
$\Delta\text{North}_{\text{PM}+\pi}$	-25.2

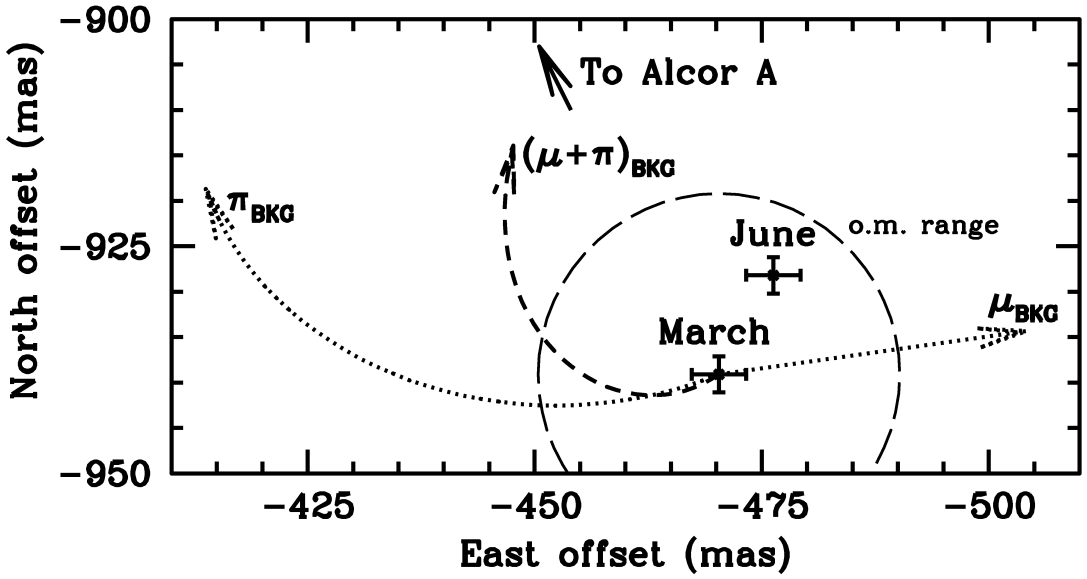

Figure 3.3 Summary of relative astrometry, plotted in terms of north and east offsets from Alcor. The two position measurements of Alcor B are plotted with their associated 1-sigma error bars, and labeled March and June, corresponding to UT epochs 2009 March 16 and 2009 June 29, respectively. The $\mu_{\rm BKG}$ and $\pi_{\rm BKG}$ arcs shows the expected change in offset of a fixed background star due to Alcor's proper and parallactic motion. The $(\mu+\pi)_{\rm BKG}$ arc is the resultant of these components over the course of our two observation epochs. We have also plotted a circle labeled "o.m. range" containing an estimate of the upper limit of orbital motion with respect to the March position.

3.7 Discussion and Conclusions

Although we observed Alcor only twice over a baseline of 103 days, the high precision ($\leq$ 3 mas) relative astrometry enabled by the pupil plane grid of Project 1640 allowed us to find common parallactic and proper motion, thereby ruling out the possibility that the newly detected point source is a background star. We expect that as we improve our techniques for interpreting data from the integral field spectrograph, we can attain yet higher astrometric precision in future studies. With sufficient sensitivity, such methods can be extended to lower mass objects, to characterize young, long period exoplanets. The rapidity of common

parallax discrimination, as opposed to observation baselines $\gtrsim 1$ year relying on proper motion analysis alone, could improve the efficiency of future high contrast imaging efforts. In particular, in the surveys that will be carried out with Project 1640 and the planned high-order adaptive optics system for Palomar, as well as the similar system planned for Gemini Observatory (Gemini Planet Imager; Macintosh et al. (2006)), repeated observations of a faint companion candidates should be scheduled $\sim$1-4 months from the initial detection epoch. This period is short enough for a typical target to remain visible in the night sky, but long enough to allow for sufficient parallactic motion for stars closer than ~ 50 pc.

Under the most favorable observation arrangements, where investigators can acquire high precision relative astrometry of a possible companion three or more times within several months of the discovery date, the common parallax technique can demonstrate physical association with yet greater rigor than we have achieved here. If the primary star traces a parallactic arc of sufficient curvature over the observation baseline, three epochs of data indicating a persistent offset vector can no longer be accounted for geometrically by a background star. In such a case, the celestial coordinate trajectory of a true companion would be seen to deviate from regular linear motion to an extent that cannot be explained by a masquerading background star, even one with the most anomalous space velocity. To thereby show that the discovered neighbor follows the arc of the host star's parallactic ellipse would demonstrate companionship most conclusively.

We note that recently Thalmann et al. (2009) also used common parallax measurements to confirm the existence of a companion to the star GJ 758. However, Thalmann et al. do not discuss the significance of this method in their article. Presumably since the

coronagraph they used lacks an astrometric grid, they were not able to attain as high a precision in the relative position of the companion as achieved in our study, reporting an uncertainty of 9.5 mas.

We acquired a low resolution ($\lambda/\Delta\lambda \sim 30$) spectrum of the companion with the Project 1640 Integral Field Spectrograph, enabling a preliminary spectral classification of M3V-M4V. We demonstrated that even with significant contamination of host starlight, a low spectral resolution integral field spectrograph can be effective in constraining the spectral type of newly discovered companions. A comparison between our broadband *J*- and *H*-band fluxes with two different mass-luminosity relationships yielded mass estimates ranging from 0.21-0.27 $M_{\odot}$. Unlike lower mass stars (e.g. Metchev & Hillenbrand 2009), few systematic surveys have been carried out with AO-equipped telescopes to characterize the frequency and mass ratio distribution of binary A stars, so it is difficult to place the significance of this discovery in the context of established binary star properties.

The object we found is relevant to the conundrum of x-ray emission from A stars. Unlike lower mass (F-M) main sequence stars and O and B stars, there is no consensus on a physical mechanism for x-ray emission from A stars. They lack the energetic winds of more massive stars, which explain the commonly seen x-ray activity of O and B stars. They also lack the convection-driven magnetic dynamos of lower mass main sequence stars, which are widely held to be the source of their x-ray emission (Pallavicini 1989). Despite this, 10-15% of A stars were detected as x-ray sources by the Röntgen Satellite (ROSAT) (Schröder & Schmitt 2007). In fact, Alcor is one of them, detected in the ROSAT All Sky Survey, with an x-ray luminosity of $L_X = 2.8 \times 10^{28}$ erg s^{-1}. It has long been proposed that un-

seen lower mass companions could account for the anomalous x-ray emission of many of these A stars (Schmitt et al. 1985). When Patience et al. (2001) surveyed A stars for stellar companions with the U.S. Air Force Advanced Electro-Optical System (AEOS), they found previously unknown companions to 8 of the 11 observed A stars with known x-ray source coincidence. Our finding lends further support to the hypothesis that hidden stellar companions explain the majority of perceived A star x-ray activity.

Appendix: History of Early Parallax Measurement Attempts with Alcor

In celestial lore, Alcor is best known for the place it shares in the sky with Mizar in the handle of the "Big Dipper" asterism. Alcor and Mizar were commonly used in ancient times as a test of visual acuity (Bohigian 2008). The fainter Alcor, at a separation of 12', cannot be discerned unless one has good natural eyesight or corrective glasses. The pair is collectively designated ζ Ursa Majoris in Johann Bayer's 1603 Uranometria star catalog. Although Alcor and Mizar share physical association in the Ursa Major moving group, it has yet to be shown conclusively whether or not they are gravitationally bound. However, Mizar itself was the first true multiple star system to be resolved with a telescope, by Benedetto Castelli, a colleague of Galileo Galilei (Fedele 1949).

Alcor and Mizar were also among the subjects of the first attempts to measure stellar parallax. Well before the invention of the telescope, stellar parallax was identified as the most conclusive way to demonstrate the Copernican assertion that the Earth orbits the

Sun (Siebert 2005). In 1897 Johannes Kepler wrote a letter to Galileo encouraging him to attempt stellar parallax measurements, hoping he would succeed where Tycho Brahe had failed. Galileo recognized that the field of view containing Mizar, Alcor and Sidus Ludoviciana (also known as HD 116798) was ideal for parallax measurements. The three stars form an approximate right triangle and they are at high declination, meaning that parallactic motion would trace an ellipse of low eccentricity. The triangle provides a position reference in two spatial directions. Galileo spent considerable effort trying to measure an actual parallactic motion (Galilei 1632) and distances to stars, but never succeeded. See Siebert's (2005) article for more detail. Although these early attempts at measuring parallax were beyond the measurement precision of the time, it is somehow poetic that a new result concerning Alcor some 400 years later relies on parallax.

Chapter 4

Spectrally-Resolved Aperture Mask Interferometry

Neil Zimmerman, Anand Sivaramakrishnan, David Bernat, Ben R. Oppenheimer, Sasha Hinkley, James P. Lloyd, Peter Tuthill, Douglas Brenner, Ian R. Parry, Lewis Roberts & John Krist

ABSTRACT

Using an observation of the binary star system β CrB, we demonstrate how the non-redundant aperture mask interferometry technique can be adapted to integral field spectrographs. Up to the present date, mask fringe patterns have been recorded in the light of a single filter. The Project 1640 integral field spectrograph, optimized for coronagraphic exoplanet surveys with the Palomar 3000-actuator adaptive optics system, facilitates recording a mask fringe pattern simultaneously in 23 channels spanning the *J* and *H* bands (1.1

μm–1.8 μm). We use this to retrieve the first low-resolution spectrum of the F3–F5 dwarf secondary component of β CrB, at angular separation 141 mas (projected physical separation $\sim$5 AU) to the A5–A7Vp primary star. In addition to providing physical information about the source, spectrally-resolved fringes have the potential to enhance detection limits over single filter observations. While the overall dynamic range of our observation suffers from large systematic calibration errors, the noise floor is reduced by a factor of 3–4 when comparing the sensitivity of the full channel range to the best single channel.

4.1 Introduction

Aperture mask interferometry is a well-established technique for overcoming the limits imposed on high-resolution imaging by wave front errors at visible and infrared wavelengths (Baldwin et al. 1986; Haniff et al. 1987; Readhead et al. 1988). In this approach, the telescope pupil is obstructed by a carefully designed mask, altering the point spread function from a classical Airy disk to an elaborate pattern of interference fringes, also called an interferogram. Certain properties of the interferogram, most notably its associated set of closure phases, are robust to perturbations that corrupt a conventional filled-aperture image. Here the sub-apertures in the pupil mask function analogously to the antennas comprising a radio interferometer. Indeed, the concept of closure phase calibration originated in that area of astronomy well before being applied at optical wavelengths (Jennison 1958). In the case of a *non-redundant* aperture mask, the baseline between each pair of subapertures is unique, and consequently there is no confusion in extracting the fringe properties. Under appropriate conditions, closure phases depend only on the geometry of the sub-aperture

layout and the intensity distribution of the target. In effect, the aperture mask observer trades a flood of degraded observables for a small number of well-calibrated ones.

Necessarily, there are trade-offs in this approach, and the gains over direct imaging are restricted to the regime of high dynamic range measurements on angular scales near the diffraction limit of the telescope. Even there, the benefits of aperture mask interferometry rest delicately on the strategy of data acquisition. The rapid, severe changes in the wave front error caused by the atmosphere set a time scale on the order of 10-100 milliseconds required for a seeing-limited aperture mask observer to "freeze" the state of the perturbations and capture the interferogram closure phases with useful accuracy (less than $\sim$1 radian). Nonetheless, by combining a large ensemble of such short exposures, major discoveries of otherwise inaccessible astrophysical sources have been made, such as the resolved structure of dust envelopes and nebulae around evolved stars (e.g., Monnier et al. 1999; Tuthill et al. 2000, 2006b), and accretion phenomena in interacting binary star systems (e.g., Ireland et al. 2007).

Over a decade of observational work by the high-contrast imaging community has shown that when using a high-order adaptive optics system under excellent seeing conditions, the dominant residual phase errors in a pupil are the long-lived, non-common path errors originating from telescope and instrument optics, rather than atmospheric distortions. In a conventional filled-aperture image, these systematic, adaptive optics (AO), correction errors result in a halo of quasi-static speckles around the target star (Racine et al. 1999; Sivaramakrishnan et al. 2002; Hartung et al. 2003; Marois et al. 2005; Hinkley et al. 2007). Aperture mask observations can take advantage of the same AO correction to boost their in-

tegration times, no longer limited by the atmospheric coherence time (Tuthill et al. 2006a). Furthermore, the closure phases should be largely immune to the non-common path errors that form speckles. In combined, AO, aperture mask observations, wave front distortions are compensated to such an extent that closure phase precision remain stable over more than ten minutes to within one degree (e.g., Lloyd et al. 2006; Pravdo et al. 2006). This is an order of magnitude improvement over what is possible with the extremely short (< 0.1 s) exposures necessary to "freeze" the fringe phase without AO under good seeing conditions (e.g., Baldwin et al. 1986; Haniff et al. 1987; Readhead et al. 1988). The longer integration times enabled by high-order AO have opened up the possibility of using the technique to search for faint companions at extremely close angular separations from nearby stars. In practice, the inner working angle of a Lyot coronagraph, the most widely used tool for high-contrast imaging, is $\sim 3\lambda/D$ (e.g., Leconte et al. 2010; Chauvin et al. 2010b). For a star at 50 pc observed at H band on a 5-meter telescope, for example, this implies that the lower limit of orbital separation that can be probed is ~ 10 AU. Therefore, aperture mask observations can take advantage of their ability to reach angular separations at the diffraction limit to compliment coronagraph surveys, probing scientifically valuable parameter space.

In recent years a number of promising results have been attained by combining non-redundant aperture mask (NRM) interferometry with AO. Besides unique resolved measurements of individual binary and multiple star systems (e.g., Ireland et al. 2008; Martinache et al. 2009), there has been one high-contrast survey of stars in the Upper Scorpius moving group (Kraus et al. 2008), and another survey for companions of L dwarfs (Bernat

et al. 2010). A large portion of the first survey and all of the latter survey were carried out at with the Palomar Hale Telescope's adaptive optics system (PALAO) in the near-infrared (Dekany et al. 1997). Both have yielded new sub-stellar companion candidates. More recently, Hinkley et al. (2011a) used *L'*-band masking with the NIRC2 camera at Keck Observatory to place constraints on planetary mass companions within the orbital radius of those already detected through direct imaging (Marois et al. 2008a, 2010).

In this investigation, we extend the NRM technique to integral field spectroscopy, thereby adding a wavelength dimension to the closure phase data set. The Project 1640 (P1640) integral field spectrograph, based at Palomar Observatory's Hale Telescope, was designed in conjunction with an apodized Lyot coronagraph to carry out a survey for young, giant, long-period exoplanets (Hinkley et al. 2011b; Soummer 2005; Sivaramakrishnan et al. 2001). The integral field spectrograph, also referred to as the integral field unit or IFU, serves two functions in P1640's standard survey mode. First, the chromatic diversity introduced by the spectrograph allows the observer to disentangle quasi-static speckles—whose positions all scale radially with wavelength—from true faint sources, and hence limit their effect on the overall dynamic range (Sparks & Ford 2002; Crepp et al. 2011). Second, the low-resolution spectrum ($\sim$ 70 nm resolution spanning the *J* and *H* bands) acquired for each spatial element, or *spaxel*, enhances the characterization of any detected source beyond conventional broadband photometry (for examples, see §3.5, §2.5, and Hinkley et al. (2010)).

We had similar motivations behind our demonstration combining NRM interferometry with the P1640 IFU. First, it was plausible that the dynamic range achieved by combining

closure phases from multi-channel interferograms would exceed that reached in the normal single-filter case. Second, as in the case of the coronagraph mode, a companion spectrum retrieved by an IFU would place useful constraints on its mass, temperature, and possibly composition. A successful example of such a spectrum extraction would provide a useful template for more ambitious targets.

We tested our approach with an observation of the well-studied 10.5 yr-period spectroscopic binary β CrB (HD 137909; $V = 3.7^{\mathrm{m}}$; J2000 coordinates $\alpha = 15^{\mathrm{h}}27^{\mathrm{m}}49.731^{\mathrm{s}}, \delta = +29^{\circ}06'20.53''$; d = 35.0 pc measured by the Hipparcos parallax; Perryman et al. 1997). The primary component of β CrB is an oscillating, chemically peculiar A star with strong magnetic features (Oetken & Orwert 1984). Its F dwarf companion was first discovered by Campbell & Moore (1907) through radial velocity measurements. Muterspaugh et al. (2010) carried out the most recent orbit determination, combining nearly one century of radial velocity data with astrometry from the Palomar High-precision Astrometric Search for Exoplanet Systems (PHASES) project and speckle imaging. The projected semi-major axis of the binary orbit is 204 mas; at our observation epoch their angular separation was 141 mas, close to twice the Hale Telescope diffraction limit in the *H* band. The contrast ratio between the primary and secondary is roughly a factor of four across the *J* and *H* bands.

4.2 Method

4.2.1 Principles of Non-Redundant Aperture Mask Interferometry

For a target consisting of two or more point sources, one can show how the interferogram created by a non-redundant mask (NRM) allows us to constrain fundamental source properties in a manner which is robust to a major class of wave front errors. Suppose we have a binary-valued pupil plane mask. The transmission function, defined over a two-dimensional Cartesian vector *u* in the telescope pupil plane (with the origin at the center of the pupil), can be specified as

$$\mathbb{M}(\mathbf{u}) = \Pi\left(\frac{\mathbf{u}'}{a}\right) * \sum_{i=1}^{N_h} \delta(\mathbf{u} - \mathbf{h}_i), \tag{4.1}$$

the convolution of some subaperture "hole" function Π of characteristic width a with a set of subapertures centered at vector positions $\boldsymbol{h}_i$. Here $\delta(\mathbf{u})$ is the Dirac delta function. For example, a circular subaperture function would be defined as follows:

$$\Pi\left(\frac{\boldsymbol{u}}{a}\right) := \begin{cases} 1 & \frac{|\boldsymbol{u}|}{2a} \leq \frac{1}{2} \\ 0 & \text{otherwise.} \end{cases} \tag{4.2}$$

Consider the case where we observe a binary star defined by Cartesian separation vector $\boldsymbol{\rho}$ on the sky, with each component in units of radians, and wavelength-dependent contrast ratio $\eta(\lambda)$. The scalar phasor representations of the ideal, unperturbed electric field due to the primary and secondary stars at the pupil are, respectively,

$$\mathbb{E}_1(\boldsymbol{u},\lambda) = 1 \quad \text{and} \quad \mathbb{E}_2(\boldsymbol{u},\lambda) = \frac{e^{i2\pi\boldsymbol{\rho}\cdot\boldsymbol{u}/\lambda}}{\sqrt{\eta(\lambda)}}. \tag{4.3}$$

Therefore, just behind the pupil mask, the electric field due to the on-axis primary star is $\mathbb{P}_1(\boldsymbol{u},\lambda) = \mathbb{M}(\boldsymbol{u})$, while that due to the fainter secondary star is $\mathbb{P}_2(\boldsymbol{u},\lambda) = \frac{e^{i2\pi\boldsymbol{\rho}\cdot\boldsymbol{u}/\lambda}}{\sqrt{\eta(\lambda)}}\mathbb{M}(\boldsymbol{u})$. By Fraunhofer diffraction, the resulting intensity pattern in the focal plane is

$$I(\boldsymbol{x},\lambda) = \mathcal{P}_1(\boldsymbol{x},\lambda)\mathcal{P}_1^*(\boldsymbol{x},\lambda) + \mathcal{P}_2(\boldsymbol{x},\lambda)\mathcal{P}_2^*(\boldsymbol{x},\lambda) \tag{4.4}$$

where

$$\begin{aligned}
\mathcal{P}_1(\boldsymbol{x},\lambda) &= \mathfrak{F}\{\mathbb{P}_1(\boldsymbol{u},\lambda)\} \\
&= \iint\limits_{\boldsymbol{u}\in\mathbf{R}^2} \mathbb{M}(\boldsymbol{u}) e^{-i2\pi\boldsymbol{x}\cdot\boldsymbol{u}/\lambda} d\boldsymbol{u} \\
&= \mathfrak{F}\left\{\Pi\left(\frac{\boldsymbol{u}}{a}\right)\right\} \sum_{i=1}^{N_h} e^{-i2\pi\boldsymbol{h}_i\cdot\boldsymbol{x}/\lambda}
\end{aligned} \tag{4.5}$$

and

$$\begin{aligned}
\mathcal{P}_2(\boldsymbol{x},\lambda) &= \mathfrak{F}\{\mathbb{P}_2(\boldsymbol{u},\lambda)\} \\
&= \frac{1}{\sqrt{\eta(\lambda)}}\mathfrak{F}\left\{\Pi\left(\frac{\boldsymbol{u}}{a}\right)\right\} \sum_{i=1}^{N_h} e^{-i2\pi\boldsymbol{h}_i\cdot(\boldsymbol{x}-\boldsymbol{\rho})/\lambda}
\end{aligned} \tag{4.6}$$

No cross terms between the fields of the individual sources appear, because those products

average to zero over any time interval average greater than $\sim 1/\Delta\nu$, the inverse of the bandwidth. At wavelengths in the infrared range and below, this intrinsic wave coherence time is far below the sample interval of a solid state detector.

Let us define $\mathcal{V}(\mathbf{u}')$ as the inverse Fourier transform of the focal plane intensity pattern. By starting from Equations 4.4– 4.6 and applying the convolution theorem and standard Fourier transform identities, we arrive at

$$\begin{aligned} \mathcal{V}(\boldsymbol{u'},\lambda) &= \mathfrak{F}^{-1}\{I(\boldsymbol{x},\lambda)\} \\ &= \left(1+\frac{e^{i2\pi\boldsymbol{\rho}\cdot\boldsymbol{u}'/\lambda}}{\eta(\lambda)}\right)\Lambda\left(\frac{\boldsymbol{u}'}{a}\right) * \left[N_h\delta(\boldsymbol{u}')+\sum_{i\neq j}\delta\left(\boldsymbol{u}'-(\boldsymbol{h}_j-\boldsymbol{h}_i)\right)\right] \end{aligned} \quad (4.7)$$

where $\Lambda\left(\frac{\boldsymbol{u}'}{a}\right)$ is the autocorrelation of the subaperture function of Equation 4.2. If the mask geometry is *non-redundant*, so that the displacement vector between each pair of subapertures is unique, then when $V(\boldsymbol{u'},\lambda)$ is evaluated at baseline $\boldsymbol{b}_{i,j}=\boldsymbol{h}_j-\boldsymbol{h}_i$, the formula reduces to

$$\mathcal{V}(\boldsymbol{b}_{i,j},\lambda) = 1+\frac{e^{i2\pi\boldsymbol{\rho}\cdot\boldsymbol{b}_{i,j}/\lambda}}{\eta(\lambda)} \quad (4.8)$$

This expression on the right hand side is identical to the spatial coherence function of the pupil plane electric field (also known as the spatial autocorrelation), evaluated at $\boldsymbol{b}_{i,j}$, since for our pair of point sources

$$\begin{aligned}\left\langle \mathbb{E}(\boldsymbol{u}+\boldsymbol{u}',\lambda)\mathbb{E}^*(\boldsymbol{u},\lambda)\right\rangle &= \mathfrak{F}^{-1}\{\mathcal{E}(\boldsymbol{x},\lambda)\mathcal{E}^*(\boldsymbol{x},\lambda)\} \\ &= 1+\frac{e^{i2\pi\boldsymbol{\rho}\cdot\boldsymbol{u}'/\lambda}}{\eta(\lambda)}. \end{aligned} \tag{4.9}$$

The equality in the first line holds due to the Wiener-Khinchin theorem, relating the auto-correlation of a function to its Fourier transform. In general, the goal of any interferometer is to sample the spatial coherence function at as many baselines as possible. The *visibility* data as expressed in Equation 4.8 comprise the necessarily incomplete recovery of this function.

We might further restrict our measurement to the phase of the visibility. For the binary star, we now express the phase associated with a particular baseline. We represent the baseline vector by $\boldsymbol{b}_{i,j}$, the sky-projected binary separation vector as ρ (in units of radians), and the wavelength-dependent phase errors at subapertures i and j by $\phi_i(\lambda)$ and $\phi_j(\lambda)$, respectively. Then the total baseline interference fringe phase, Φ, is given by

$$\begin{aligned}\Phi(\boldsymbol{b}_{i,j},\lambda) &= \tan^{-1}\left[\frac{\sin(2\pi\boldsymbol{\rho}\cdot\boldsymbol{b}_{i,j}/\lambda)}{\eta(\lambda)+\cos(2\pi\boldsymbol{\rho}\cdot\boldsymbol{b}_{i,j}/\lambda)}\right]+\phi_j(\lambda)-\phi_i(\lambda) \\ &:= \Phi_{\rm src}(\boldsymbol{b}_{i,j},\lambda)+\phi_j(\lambda)-\phi_i(\lambda). \end{aligned} \tag{4.10}$$

In the second line, we have abbreviated the arc tangent term, which is intrinsic to the source properties, as $\Phi_{\rm src}$. The "piston" phase error description used here, although merely an approximation to the actual wave front structure introduced by the turbulent atmosphere and

non-common path errors in the instrument, is particularly useful because of its algebraic properties. For any baseline triplet that forms a triangle, take the sum of the visibilities:

$$\begin{aligned}
\Psi_{i,j,k}(\lambda) &= \Phi(\boldsymbol{b}_{i,j},\lambda)+\Phi(\boldsymbol{b}_{j,k},\lambda)+\Phi(\boldsymbol{b}_{k,i},\lambda) \\
&= \Phi_{\rm src}(\boldsymbol{b}_{i,j},\lambda)+\phi_j(\lambda)-\phi_i(\lambda) \\
&\quad +\Phi_{\rm src}(\boldsymbol{b}_{j,k},\lambda)+\phi_k(\lambda)-\phi_j(\lambda) \\
&\quad +\Phi_{\rm src}(\boldsymbol{b}_{k,i},\lambda)+\phi_i(\lambda)-\phi_k(\lambda) \\
&= \Phi_{\rm src}(\boldsymbol{b}_{i,j},\lambda)+\Phi_{\rm src}(\boldsymbol{b}_{j,k},\lambda)+\Phi_{\rm src}(\boldsymbol{b}_{k,i},\lambda) \qquad (4.11)
\end{aligned}$$

The piston phase errors of all three subapertures cancel out, leaving only the sum of the terms caused by the target intensity distribution. This quantity, known as the *closure phase*, has been exploited in radio wavelength interferometry since the 1950s (Jennison 1958), and optical and infrared interferometry since the 1980s (Baldwin et al. 1986). For an interferometer with N_h elements (in our case, mask holes), there are $\binom{N_h}{2} = N_h(N_h-1)/2$ baselines, and $\binom{N_h}{3} = N_h(N_h-1)(N_h-2)/3!$ closure triangles. Of those $\binom{N_h}{3}$ triplets, however, only $(N_h-1)(N_h-2)/2$ are independent, since a given visibility phase will reappear in many closing triangles.

4.2.2 Integral Field Spectrograph Representation of NRM Data

In the case of Project 1640, the intensity pattern in Equation 4.4 is formed on the microlens array at the entrance of the spectrograph. From there, the beam from each microlens is dis-

persed by a prism and focused as a low-resolution spectrum on the detector (for more details of the IFU design, see (Hinkley et al. 2011b)). The data reduction algorithms described in Chapter 2 extract a cube from the detector image, effectively a stack of narrowband images:

$$\hat{I}[s_x, s_y, w] = \sum_{w'=w-3}^{w+3} I\left(\alpha(s_x\hat{x} + s_y\hat{y}), \lambda(w')\right) g[w' - w] \tag{4.12}$$

where s_x and s_y are integers indexing the spatial position of the three-dimensional pixel, or *spaxels* associated with individual microlenses, with origin at the target star position; $\hat{x}$ and $\hat{y}$ are Cartesian unit vectors in the image plane; the integer w indexes data cube wavelength channels ranging from 0 to $N_{\text{chan}} - 1$; $g[w]$ is a discrete function approximating the effective filter of each channel (defined for $-3 \leq w \leq 3$; see § 2.4.2.4 for further explanation); and lastly α is the angular scale of one spaxel in radians.

In analogy with Equation 4.7, we take the channel-wise inverse discrete Fourier transform of each interferogram cube $\hat{I}[s_x, s_y, w]$ to form the corresponding visibility data set:

$$\begin{aligned} \hat{V}[k_u, k_v, w] &= \text{DFT}^{-1}\left\{\hat{I}[s_x, s_y, w]\right\} \\ &= \left(\frac{1}{L}\right)^2 \sum_{s_x=-L/2+1}^{L/2} \sum_{s_y=-L/2+1}^{L/2} \hat{I}[s_x, s_y, w] e^{i2\pi(s_x k_u + s_y k_v)/L} \end{aligned} \tag{4.13}$$

Here L is the width and height of the centered interferogram cube in pixels. It can be shown that this discrete visibility cube is equivalent to the original continuous representation in Equation 4.7, when the independent units are scaled appropriately:

$$\hat{V}[k_u, k_v, w] \simeq \mathcal{V}\left(\boldsymbol{u} = \frac{k_u \lambda(w)}{\alpha L}\hat{u} + \frac{k_v \lambda(w)}{\alpha L}\hat{v}, \lambda(w)\right) \tag{4.14}$$

The equality is only approximate, due to the effects of finite channel bandwidth and sampling in the intervening stages.

Once the closure phases have been extracted from the visibility cube, we formulate a maximum likelihood problem to ask what kind of source distribution provides the best fit to the closure phase data set. A simple source like a binary star is fully described by two offset coordinates and N_{chan} values of the contrast function $\eta(\lambda)$. For any set of candidate parameters, we generate a set of model closure phases by using the expression for $\Phi_{\text{src}}(\boldsymbol{b}_{i,j}, \lambda)$ in Equation 4.10 to evaluate the closure phase formula in Equation 4.11 for all closing triangles at all channels. The goal is to find the set of source parameters which generates a closure phase model with minimum difference to the measurements.

4.3 Observations

Using design parameters similar to previous pupil masks behind PALAO, we ordered the fabrication of a nine-hole non-redundant mask pattern on a thin stainless steel disk. The mask geometry was scaled to match the first pupil plane in the P1640 coronagraph, at the position of the Lyot stop. Each subaperture in the mask is a hexagon of point-to-point diameter 0.403 mm (measured across opposing vertices), translating to 0.526 m in the telescope pupil (compared to the 5.08 meter primary mirror aperture). The shortest and longest effective baselines on the mask are 0.76 m and 4.23 m. The overall transmission of

Table 4.1. Summary of P1640 NRM observations

Target	Mean UT date	# of NDR sequences	# of reads	Total exposure time (s)
β CrB	2010 March 24 12:05	16	320	2471 s
κ CrB	2010 March 24 12:59	15	300	2316 s

the mask is 9.1% of the full telescope pupil.

We configured P1640 for NRM observations on 2010 March 24 by replacing the coronagraph Lyot stop mask with the non-redundant pupil mask. Once the pupil mask was mounted, the only change necessary from normal coronagraph data acquisition was to ensure that the target was offset from the focal plane mask, effectively a 370 mas-diameter occulting spot near the center of the IFU's 3.8″-wide field of view. With the mask in place, we acquired 16 non-destructive read (NDR) sequences of the interferogram of β CrB, the spectroscopic binary target. Each NDR sequence from our HAWAII-2 detector consisted of 20 successive 7.721 s reads, resulting in a total exposure time of 2471 s, about 41 minutes (more information on our detector read scheme can be found in §2.2).

We followed the target observation with a similar observing sequence of a nearby calibrator star κ CrB (HD 142091), with a slightly shorter integration time of 15 NDR sequences. Ten minutes separated the end of the last β CrB NDR sequence from the start of the first κ CrB NDR sequence. Both the target and calibrator stars were bright enough ($V = 3.7^{\mathrm{m}}$ and 4.8^{m}, respectively) to be acquired as natural guide stars by the Palomar AO system. Our log indicates $\sim 1''$seeing through the duration of this data set. The dates and exposure schemes of the observations are summarized in Table 4.1.

In NRM observations, it is typical to observe a single star as a calibration reference

to measure systematic errors in the closure phases. We note that κ CrB in fact hosts a giant exoplanet with projected semi-major axis 87 mas, as inferred from radial velocity and transit measurements (Johnson et al. 2008). However, given the planet's mass and and the estimated system age—1.8 $M_{\rm Jup} \sin i$ and 2.5 Gyr, respectively—it is highly unlikely that emission from this object could have produced a measurable change in the source wave front of κ CrB. Suppose the orbital inclination of the exoplanet candidate is only 1 deg, so that mass is actually 100 $M_{\rm Jup}$, placing it comfortably inside the M-dwarf range of spectral types. Then, according to the cooling curves for low-mass stars by Baraffe et al. (2003), at an age of 1 Gyr, in H band, it would appear at a contrast of ~ 10 magnitudes with respect to the host star. While 10 magnitudes of contrast is a plausible goal for high-contrast NRM observations to reach in the near future, it is well beyond the performance we achieve in this experiment, in terms of both measurement precision and calibration of systematic errors. Therefore, we confidently treat our κ CrB data as those of an ideal point source.

On the following night, with the pupil mask removed and the coronagraph returned to its normal configuration, we acquired direct images (non-occulted) of a calibration visual binary star. This data later served to establish our plate scale and orientation for the epoch. We chose the binary star HIP 55203, because its separation (1.6″) spanned a good fraction of our field of view, and its USNO Sixth Orbit Catalog ephemeris was ranked in the highest quality category (Hartkopf et al. 2001).

We used the Project 1640 Cube Extraction Pipeline (PCXP; Chapter 2) to translate our raw spectrally-resolved fringe data into cubes. This software is fully described in Chapter 2; a finished cube consists of 23 channel images spanning the 1.10 μm—1.76 μm passband.

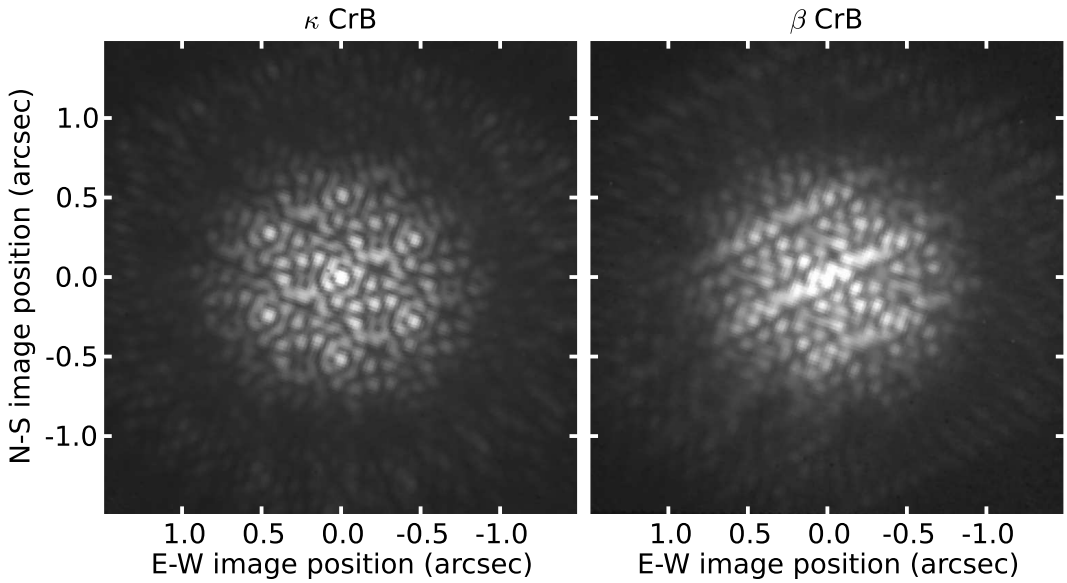

Figure 4.1 One example of an interferogram cube slice for each target: the calibrator κ CrB on the left and the spectroscopic binary β CrB on the right. Channel 21 of 23 (1.7 μm) is displayed, with a square-root stretch. For clarity, the cube channel images have each been cropped to center the brightest portion of the interferograms.

Before the cube extraction takes place, however, the PCXP has the option of preparing the raw detector data in two very different ways. In the normal case, the PCXP fits a slope to the non-destructive count samples in each detector pixel, thus producing a reduced spectrograph focal plane image in which each pixel represents the count rate over the course of the corresponding NDR sequence. In an alternative mode, the PCXP takes the differences between each pair of consecutive reads (after bias/dark subtraction, flat fielding, etc.), producing a stack of 19 short exposure spectrograph focal plane images, each with integration time 7.7 s. Ignorant of which processing mode would produce higher quality results, we generated both versions of reduced spectrograph focal plane images for the full data set. From there, the PCXP proceeded with cube extraction from all spectrograph focal plane image versions with default parameters. For brevity hereafter, we distinguish between the

two co-existing reduced data sets as follows: “short exposures” for the interferogram and visibility cubes generated from 7.7 s read differences, and “long exposures” for the slope-fit cubes with integration time 154 s. We show one example the long exposure interferograms of each target in Figure 4.1.

4.4 Closure Phase Extraction

We sent the interferogram cubes created by the PCXP through a separate customized pipeline written in Python, whose final products are the visibility data cubes. Each interferogram cube was aligned to the nearest pixel in the center of a new array, and multiplied by a super-Gaussian window function of the form $e^{-m|s|^4}$ (after Bernat et al. (2010)), where the constant m is adjusted so that the window rolls off near the first null in the subaperture diffraction envelope at the red end of the passband. The windowed interferogram was zero-padded up to array width L to avoid aliasing. Next, following Equation 4.13, we took the channel-wise inverse discrete Fourier transform (DFT) of the interferogram cubes. We stored the amplitude and phase of each resulting visibility data set in separate FITS cube files.

One of the systematic noise sources in P1640 data cubes is cross-talk, discussed in § 2.4.2.5. Due to the proximity of the interleaved microlens spectra, the wings of the IFU point spread function at one channel in a given spectrum overlap with an offset channel in a vertically neighboring microlens spectrum (to visualize, consider the diagram of the spectrograph focal plane in the right hand panel of Figure 2.2). Therefore, a small fraction of one spaxel’s light is erroneously counted in a vertically neighboring spaxel, at an offset

channel. We formulated an approximate model for the effect of cross-talk on the visibility data cube as follows. First, we expressed the cross-talk contaminated interferogram cube, $\underline{\hat{I}}$, in terms of the ideal one, $\hat{I}$ from Equation 4.12:

$$\underline{\hat{I}}[s_x, s_y, w] \simeq \hat{I}[s_x, s_y, w] + \gamma_{\uparrow}\hat{I}[s_x, s_y + 1, w_{\uparrow}] + \gamma_{\downarrow}\hat{I}[s_x, s_y - 1, w_{\downarrow}], \tag{4.15}$$

where $\gamma_{\uparrow}$ and $\gamma_{\downarrow}$ are, respectively, the cross-talk coefficients for light crossing over from the microlens spectrum above, and the microlens spectrum below the current one at spaxel (s_x, s_y). We measured the following mean cross-talk coefficients in our data:

$$\begin{aligned} \gamma_{\uparrow} &= \begin{cases} 0.077 & 0 \leq w \leq 12 \\ 0 & \text{otherwise} \end{cases} \\ \gamma_{\downarrow} &= \begin{cases} 0.075 & 10 \leq w \leq 22 \\ 0 & \text{otherwise} \end{cases} \end{aligned} \tag{4.16}$$

The offset channels for each of these cross-talk directions are symbolized by $w_{\uparrow}$ and $w_{\downarrow}$. These are determined by the pitch between interleaved neighboring microlens spectra projected onto the dispersion axis, measured in channel intervals. For the P1640 spectrograph focal plane pattern, they are: $w_{\uparrow} = w + 10$ and $w_{\downarrow} = w - 10$. The channel-wise inverse DFT of equation 4.15 gives

$$\begin{aligned} \underline{\hat{V}}[k_x, k_y, w] &= DFT^{-1}\left\{\underline{\hat{I}}[s_x, s_y, w]\right\} \\ &\simeq \hat{V}[k_u, k_v, w] + \gamma_{\uparrow}e^{-i2\pi k_v/L}V[k_u, k_v, w_{\uparrow}] + \gamma_{\downarrow}e^{i2\pi k_v/L}V[k_u, k_v, w_{\downarrow}] \end{aligned} \tag{4.17}$$

The phasor in front of each cross-talk term arises from the fact that cross-talk, as described in Equation 4.15, carries flux either down or up by exactly one spaxel, resulting in a phase shift in (k_u, k_v) space. This phase shift is fixed at a given vertical spatial frequency k_v. Most importantly, it means that in the Fourier domain, we can compensate for cross-talk by subtracting the appropriate offset channel arrays from the target channel, after multiplying them by the complex cross-talk coefficient array.

The cross-talk subtraction can be improved by cleaning the contaminating channels themselves before subtracting them from the target channel. This is in fact how we treated the κ and β CrB visibility cubes. Even more levels of recursion are possible, but since this cross-talk model is only an approximation in the first place (e.g., the cross-talk coefficients are not truly constant with image position or spatial frequency, the channel offset is not exactly 10, etc.), and the cascaded coefficient at the n^{th} recursion level γ^{n+1} quickly shrinks to an insignificant factor relative to other noise sources, we would not improve the correction. In the current algorithm with one level of recursion in the subtraction, the benefits to the closure phase accuracy, as shown in Figure 4.4, are substantial for channels with relatively weak signal.

Figure 4.2 shows one example visibility amplitude data channel for each target, after cross-talk compensation. Each peak, also known as a *splodge*, represents the fringe amplitude at a given baseline. The central peak is due to the $N_h\delta(\boldsymbol{u}')$ term in Equation 4.7, around which there are 72 splodges: one for each of the 36 baseline vectors $\boldsymbol{b}_{i,j} = \boldsymbol{h}_j - \boldsymbol{h}_i$ and their reverses, $\boldsymbol{b}_{j,i} = \boldsymbol{h}_i - \boldsymbol{h}_j$. The κ CrB visibility amplitudes are relatively flat across the spatial frequencies, as expected for a single point source, while the β CrB amplitude

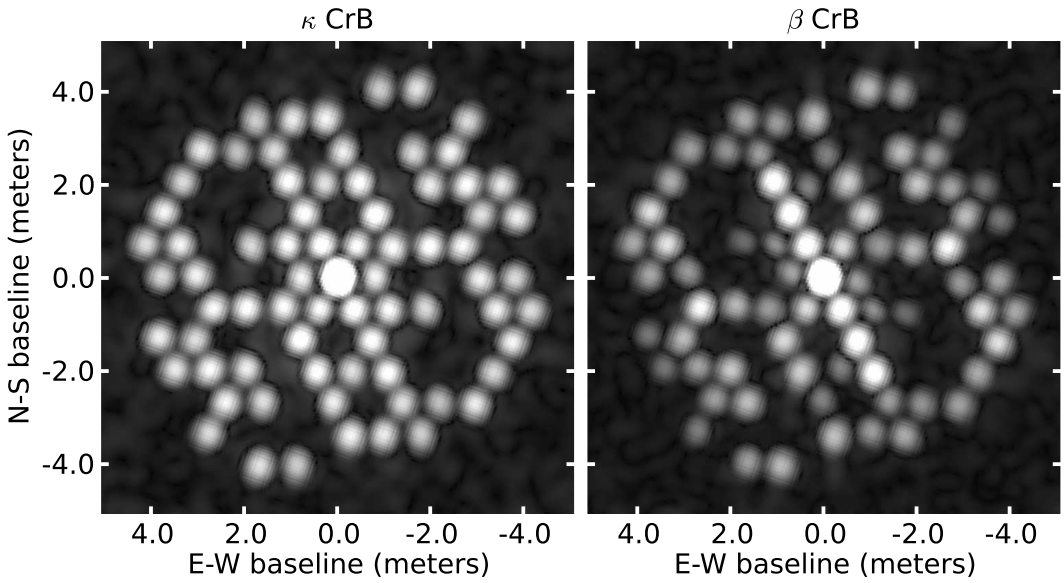

Figure 4.2 Channel 21 of 23 (1.7 μm) in two example long exposure visibility amplitude cubes. The data are displayed with a square-root stretch.

data suggest a more complicated source distribution.

We used the positions of the amplitude peaks in the long exposure calibrator visibility cubes to establish the exact spatial frequencies in each channel. From these we derived the true baselines. Although we had prior knowledge of the baselines from the mask geometry, by measuring the baselines from the data we eliminated uncertainty due to potential errors in the pupil alignment. Our extraction scripts fitted an elliptical cone to each long exposure amplitude splodge (with freely varying base ellipse shape, position, and height) to determine its spatial frequency coordinates. The measured spatial frequencies for each baseline and channel combination are in turn averaged over the entire calibrator data set.

In order to model IFU closure phase data, it is critical to establish an accurate channel-wavelength relationship in the data cube. The PCXP uses a weighted sum on the spectrograph focal plane image to determine the flux in each cube spaxel. Depending on the shape

of the microlens spectrum where the extraction occurs, the effective wavelength can be biased up to of order 10 nm. We anchored the channel-wavelength scale to the channels with peak count rate in each half of the passband, since those would have negligible bias. From here, we derived the full channel-wavelength function from the mean scaling of the fringe spatial frequencies with respect to these fiducial channels. The result, plotted in Figure 4.3, shows the *effective* wavelength of each data channel. The graph shows the expected linearity in the regions where the signal is relatively strong and even, and veers off from the ideal extraction wavelength where the IFU spectral response function (Figure 2.13) changes steeply. We note that in normal coronagraph imaging mode, similar measurements of the data cube channel-wavelength relationship can be made from the scaling of the speckle pattern, as in Crepp et al. (2011). We calculate the true, physical baseline vectors (in units of meters) from the spatial frequencies in the anchored channels as follows:

$$\boldsymbol{b}_{i,j} = \frac{k_{u_{i,j}}\lambda}{\alpha L}\hat{\boldsymbol{u}} + \frac{k_{v_{i,j}}\lambda}{\alpha L}\hat{\boldsymbol{v}}. \tag{4.18}$$

Here $k_{u_{i,j}}, k_{v_{i,j}}$ are the coordinates of the spatial frequency corresponding to baseline i, j; α is the plate scale in units of radians per spaxel, derived from our calibration observation of HIP 55203; and L is the array width of the visibility cube. We note that there is a slight foreshortening in the measured baselines as compared to those expected from the mask geometry. The foreshortening suggests there was a $\sim 10\,\mathrm{deg}$ tilt of the mask with respect to the pupil plane.

From each visibility cube we extracted the baseline phases using the spatial frequency coordinates. Since the peak spatial frequencies in general do not occur at integral pixel

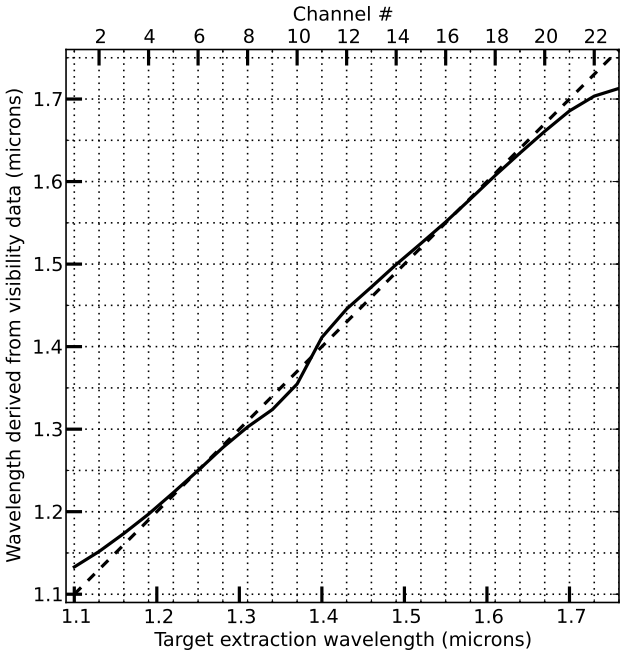

Figure 4.3 Effective channel wavelengths of the visibility data cubes. The dashed line shows the expected one-to-one relationship if there were no signal biasing during the the weighted sum cube extraction.

values, we used a two dimensional spline interpolation to estimate the phase at fractional pixel positions. Finally, we followed Equation 4.11 to calculate and store the 84 closure phases in each channel of each visibility cube.

4.5 Statistical Properties of the Spectrally-Resolved Closure Phases

The ability of NRM observations to reach high dynamic range is dependent on the stability and accuracy of the extracted closure phases. Much can be learned about our unique data set by analyzing the stochastic behavior of the calibrator closure phases alone. In Figure 4.4,

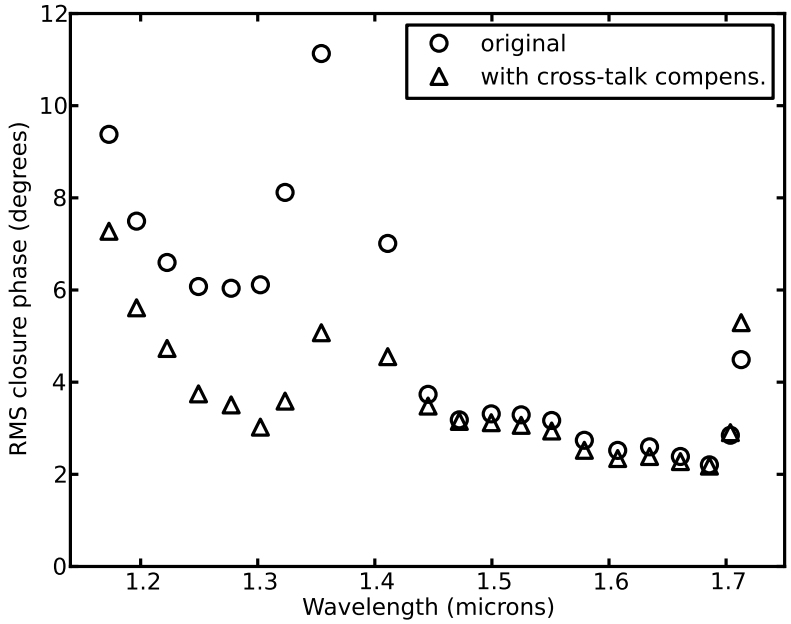

Figure 4.4 RMS closure phase values in one long calibration exposure, with and without cross-talk compensation. When we do not account for cross-talk, the visibility phasors are corrupted by scaled-down, shifted "ghost" phasors from offset channels.

we show the root mean square (RMS) value of the closure phases in one long calibrator (κ CrB) exposure as a function of wavelength. We compared the results of extraction both with and without cross-talk compensation applied to the original visibility data cube. Ideally, the closure phases for a point source would be zero. However, it is normal in AO NRM observations for systematic errors, likely due to non-common path phase errors that deviate from the piston phase error model, to cause slight offsets to individual closure phases (e.g., Kraus et al. 2008; Hinkley et al. 2011a). One of the purposes of acquiring a calibration star alongside the NRM target is to subtract this instrumental component. Since the AO wave front correction degrades towards shorter wavelengths, we expect that the errors would be slightly higher in the *J* band, which is in fact the case. Another cause of better performance

Table 4.2. Root mean square and standard deviation values of closure phase data. Each listed standard deviation is the mean of the time series standard deviations of all closure phases in the set.

Data set	Channel range	RMS (deg)	Std. dev. (deg)
κ short exp.	3–10	7.5	6.4
κ short exp.	11–22	4.3	3.4
κ long exp.	3–10	4.9	3.1
κ long exp.	11–22	3.0	1.6
β long exp.	3–10	23	7.3
β long exp.	11–22	25	3.9

at longer wavelengths is the fact that the interference fringes were oversampled at longer wavelengths, making them less susceptible to errors in cube extraction.

It is also apparent that independent of these effects, the deviations from zero closure phase are to some extent anti-correlated with interferogram signal-to-noise ratio. The water absorption trough around 1.4 μm (in between the *J* and *H* bands) coincides with a bump in κ CrB's RMS closure phase, notably attenuated by the cross-talk compensation algorithm. At channels near the edges of the passband, both water absorption and the transmission function of the instrument blocking filter lower the signal.

We tabulate RMS values and scatter of various subsets of our closure phase data in Table 4.2. Here, the column marked "Std. dev." represents the typical scatter within a closure phase measurement rather than the scatter between different closure phases. To calculate this, we determined the time series standard deviation of each closure phase. The average of these standard deviations among all closure phases within the specified channel range are tabulated. It is encouraging that the typical standard deviation is below the RMS, since that suggests that the ensemble of measurements for each closure triplet does in fact

provide a meaningful measure of the underlying systematic component.

In general, we found the short exposure closure phases had higher noise than the long exposure ones, with typical RMS and scatter both around a factor of 1.5–2 higher. This may partially be explained by anomalous detector behavior which persisted throughout the observing run (portending its eventual failure within three months of our experiment): the individual read difference focal plane images suffered from time-varying ripple structures with intensity up to a few percent of the interferogram peak, depending on the channel. Over each 20 read sequence comprising the long exposure extractions, however, those artifacts average out. It is likely that these structures contributed to much of the added noise in the short exposure versions of the fringe phases.

Although the closure phases derived from long exposures show significantly lower standard deviation, we note that they were still not quite as stable as those acquired in previous AO NRM observations at Palomar. Lloyd et al. (2006), for example, measured a typical closure phase scatter of $0.6\,\mathrm{deg}$ at H band, for a fainter star than either of our targets.

In Figures 4.5 and 4.6, we display the behavior of a typical closure phase in channel 20 as a function of time. Since the sample size of a given closure phase is 19 times larger when we consider the data broken into the short (7.7 s) exposures, that version of the data provides a more useful statistical diagnostic. Appropriately, the time series of the exhibited closure phase shows no trend, and the distribution is fairly symmetric.

We are also interested in the cross-channel correlation of the closure phases, which is an indication of the statistical independence of the data cube channels. Let us represent the closure phase with triplet index q ($0 \leq q < N_{\mathrm{trip}}$) recorded in channel index w ($0 \leq w <$

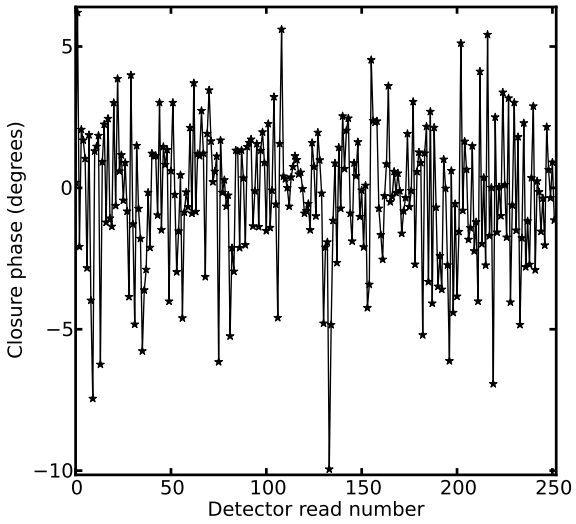

Figure 4.5 Here we plot 253 measurements of a single closure phase in data cube channel 19, extracted from the short exposure κ data set.

N_{chan}) by $\Psi_{q,w}$. The correlation coefficient between the errors in a given closure phase q at two channels w_1 and w_2 is defined as follows:

$$\text{Corr}\,(q,w_1;q,w_2) = \frac{\left\langle \left(\Psi_{q,w_1} - \overline{\Psi}_{q,w_1}\right)\left(\Psi_{q,w_2} - \overline{\Psi}_{q,w_2}\right)\right\rangle}{\sigma_{\Psi_{q,w_1}}\sigma_{\Psi_{q,w_2}}} \tag{4.19}$$

Here $\overline{\Psi}$ is the sample mean, and σ_Ψ is the sample standard deviation. Then, to quantify the independence of two channels of closure phase data w_1 and w_2, we can average $\text{Corr}\,(q,w_1;q,w_2)$ over all triplets:

$$\overline{\text{Corr}}(w_1;w_2) = \frac{\sum_{q=0}^{N_{\text{trip}}-1} \text{Corr}(q,w_1;q,w_2)}{N_{\text{trip}}} \tag{4.20}$$

To see how the cross-channel correlation behaves with respect to one channel, we held the first channel index w_1 fixed and evaluated $\overline{\text{Corr}}(w_1;w_2)$ across the passband for each

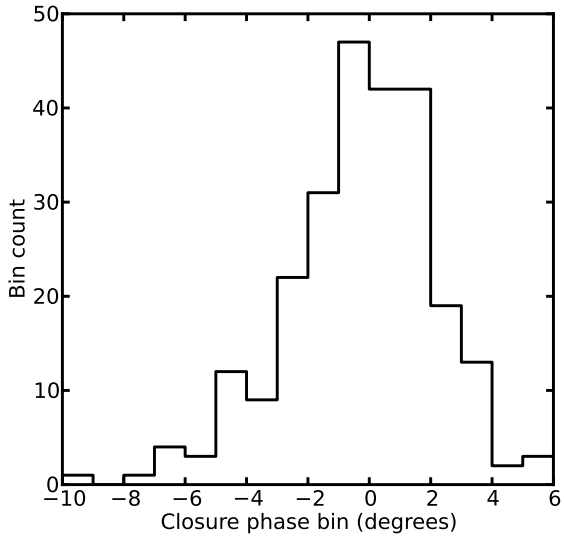

Figure 4.6 A histogram of the same 253 closure phases shown in Figure 4.5, with a bin width of one degree.

w_2. In Figure 4.7 we show the results of this calculation, first with channel 6 (1.25 μm) fixed and then channel 17 (1.58 μm). As expected, in each case the function peaks at unity in the reference channel, since in that case both the numerator and denominator of the expression in Equation 4.19 reduce to the variance of a given closure phase. What is important, however, is the high degree to which the closure phase errors are correlated across wavelength: between the middles of *J* and *H* band the correlation remains above 0.7. This is somewhat expected, since a non-common path error associated with some path length difference would perturb the phase over the entire wavelength range. We assess the impact of our measured closure phase variance and covariance values on detection limits in §4.7.

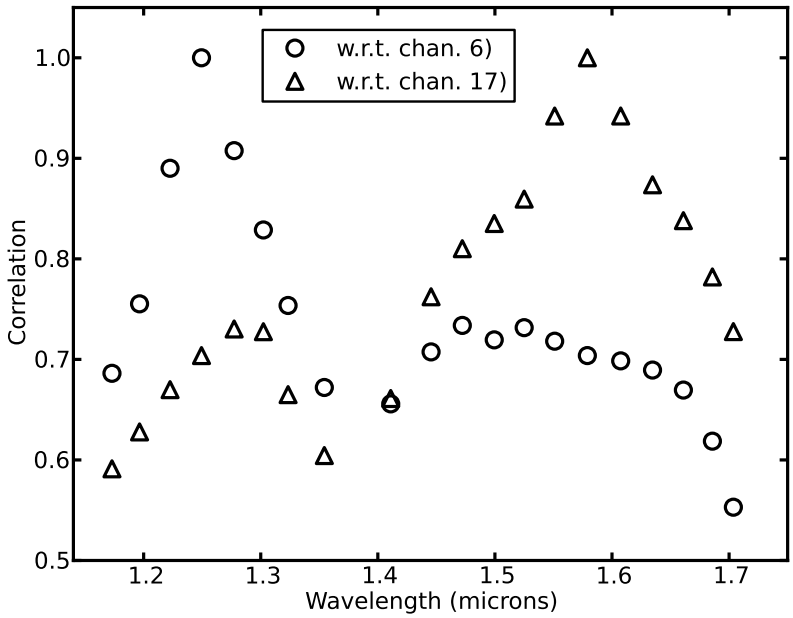

Figure 4.7 The cross-channel correlation of closure phase errors in the short exposure κ CrB data set, evaluated with respect to channel 6 and channel 17.

4.6 Results of the β CrB Closure Phase Model

For both targets, we formed a mean closure phase set by averaging the extracted long exposure closure phases over time, and discarding the end channels due to their poor quality. Next, we subtracted the mean κ CrB closure phase set from the mean β CrB closure phase set, to remove systematic errors presumably present in both data sets. From here, we fitted a binary star model to the β CrB data in two stages, following an approach similar to that of Bernat et al. (2010). First, we performed a brute force search over a coarse parameter grid. We explore a range of three parameters: radial separation (r), position angle (θ), and contrast (η). Although we expected η to vary with wavelength, for efficiency we initially treated it as a constant across the passband.

We evaluated binary star parameters using a maximum likelihood formulation (see Sivia (2006) for a helpful overview). To evaluate the misfit statistic of a given parameter combination, we took the sample covariance matrix of the closure phase data set into account, rather than treating the closure phases as statistically independent observables. This was necessary for two reasons: (i) the full set of 84 closure phases in a given channel is not linearly independent, and (ii) there are correlations in errors across channels, as shown previously in §4.5.

If we assume Gaussian noise for the closure phase errors, then the posterior probability distribution function (p.d.f.) for binary star parameter set $\boldsymbol{p}$ given a particular closure phase data set is

$$\text{prob}\left(\boldsymbol{p} \mid \boldsymbol{\Psi}, I\right) \propto \exp\left[-\frac{1}{2}\left(\widetilde{\boldsymbol{\Psi}}(\boldsymbol{p}) - \boldsymbol{\Psi}\right)^{\mathrm{T}} \mathsf{C}^{-1} \left(\widetilde{\boldsymbol{\Psi}}(\boldsymbol{p}) - \boldsymbol{\Psi}\right)\right], \tag{4.21}$$

where $\boldsymbol{\Psi}$ is a column vector representing the measured closure phases ($N_{\text{chan}} \times N_{\text{trip}}$ rows); $\widetilde{\boldsymbol{\Psi}}(\boldsymbol{p})$ is a column vector of closure phases generated from the binary model $\boldsymbol{p}$; C is the covariance matrix of the closure phase data; superscript T is the transpose operator; and I is our background knowledge, which includes how to form a model of our data from $\boldsymbol{p}$, and the covariance matrix of the data. From here we can define our misfit statistic by

$$\chi^2 = \left(\widetilde{\boldsymbol{\Psi}}(\boldsymbol{p}) - \boldsymbol{\Psi}\right)^{\mathrm{T}} \mathsf{C}^{-1} \left(\widetilde{\boldsymbol{\Psi}}(\boldsymbol{p}) - \boldsymbol{\Psi}\right). \tag{4.22}$$

We used the combination of binary star parameters which gave the lowest χ^2 in the grid search as initial conditions for a more sophisticated fitting algorithm. This stage re-

fined the position and allowed the contrast in each channel to vary independently. For this stage, we employed MPFIT, an implementation of the Levenberg-Marquardt non-linear least-squares fitting method created by Markwardt (2009). Since MPFIT does not handle observables with correlated errors, we modified a Python/NumPy adaptation of MPFIT to compute the misfit statistic using the expression in Equation4.22 rather than simply evaluating the sum of squares of the variance-normalized fit residuals.

One caveat to this method is that it requires the covariance matrix in the expressions to be positive definite. Otherwise, the inverse matrix C^{-1} required to compute the misfit statistic does not exist. In general, the covariance matrix drawn directly from a measurement sample is *not* positive definite, especially when the number of observable quantities is much higher than the number of measurement repetitions (Schfer & Strimmer 2005). For this situation, techniques exist to modify the covariance matrix so that it is well behaved. The "shrinkage" algorithm by Schafer et al. is one of them. In this solution, the off-diagonal elements (covariances) and the diagonal elements (variances) are multiplied by separate scale factors, such that the result is positive definite. We carried out their procedure for the sample covariance matrix drawn from the short exposure version of the β CrB data set (the many repetitions of measurements in this case improves the behavior of the covariance matrix), which ultimately scaled the off-diagonal elements down by a factor of 0.7.

In the first outcome, the root-mean-square level of fit residuals between the best binary model and the calibrated closure phase measurements was 8.6 degrees. We found that a small subset of closure triangles were responsible for the majority of these systematic

Table 4.3. Comparison between measured position offset of β CrB B with that predicted from the orbit by Muterspaugh et al. (2010).

	Separation (mas)	Position angle (deg. E of N)
Predicted	141.2	121.7
Measured	140.4 ± 0.6	119.22 ± 0.25

errors. We excluded the worst 15 of the 84, so that the remaining residuals in the peak *J* and *H* channels were all under 10 degrees. Repeating the full fitting procedure with the 69 retained closure phases recorded in 20 channels, the RMS fit residual decreased to 4.5 degrees. However, the change in the binary star solution was marginal, probably because the flagged closure phases had already been weighted down due to high variances.

In Table 4.3, we list the position of the companion we recovered, alongside the expected one based on the established orbit (Muterspaugh et al. 2010). The error bars on the best-fit *r* and θ values are based on the shape of the two-dimensional p.d.f. computed with the contrast ratio vector fixed. We found this p.d.f. to be nearly symmetric, and used the widest axis of 0.6 mas as the error in both the radial and azimuthal directions. The overall disparity in position is only 6.2 mas, similar to the disagreement that Bruntt et al. (2010) found in their AO-resolved direct imaging of the system (although they were comparing their position with the older orbit from Tokovinin (1984)).

To derive spectra for the two stellar components of β CrB, we combined the solved contrast ratio function $\eta(\lambda)$ with total flux measurements of the interferograms. Since a near-infrared spectrum of κ CrB is included in the IRTF Spectral Library (Rayner et al. 2009), it was straightforward to calibrate the total channel fluxes of the β CrB data. The

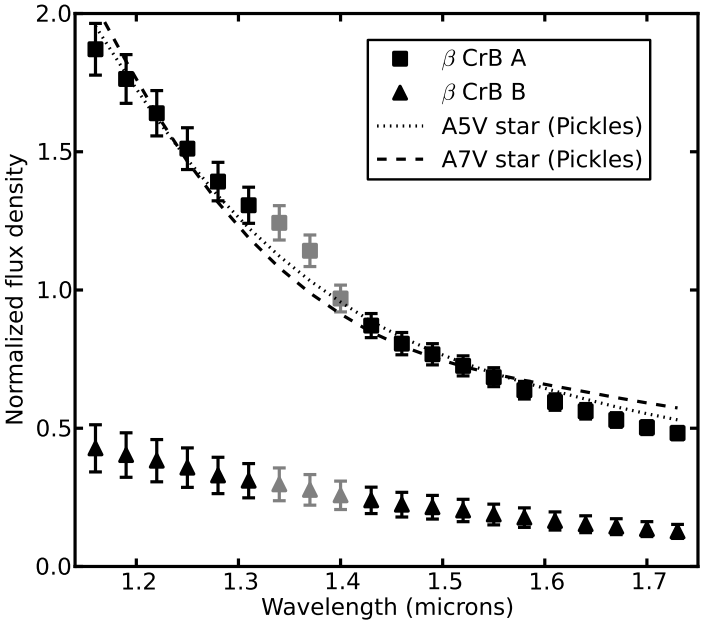

Figure 4.8 Spectra of β CrB A and β CrB B, normalized to the mean flux of β CrB A. We compare the spectrum of component A to two reference A dwarf stars from the Pickles Atlas (Pickles 1998). The gray shading indicates channels whose flux calibration was corrupted by variable telluric water absorption.

resulting pair of spectra are plotted in Figure 4.8, normalized to the mean flux density of the primary (A). We use a second plot, Figure 4.9, to clearly display the spectrum of the companion by itself. The error bars in the flux points are based on scaled parameter variances returned by the fitting algorithm, propagated through the calibration steps.

Recently, Bruntt et al. (2010) carried out a detailed investigation into the physical properties of β CrB. They measured broadband fluxes from AO imaging with VLT/NACO and stellar diameters by long baseline optical interferometry with the CHARA Array. Combining those data sets, they arrive at effective temperature estimates of 7980 ± 180 K and 6750 ± 230 K for the two stars. These temperatures imply spectral types in the range A5V–A7V and F2V–F5V (Gray et al. 2001). We overplotted reference spectra in Figures 4.8

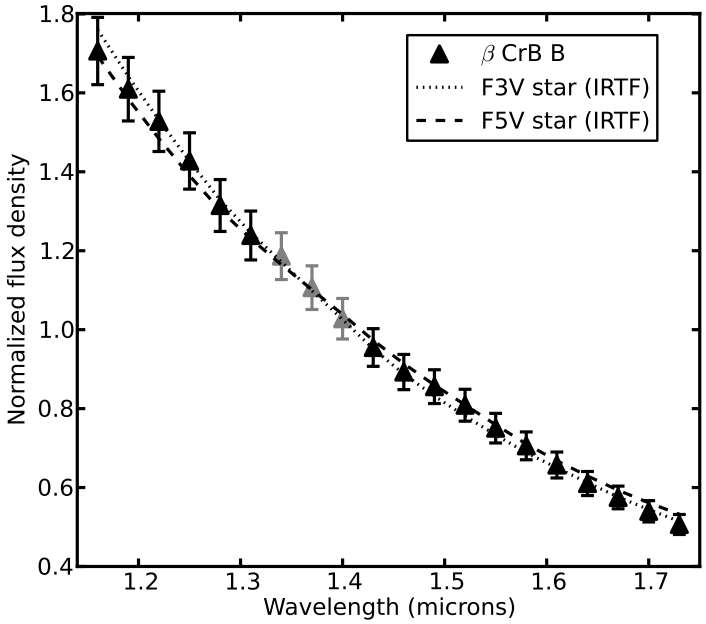

Figure 4.9 Mean-normalized spectrum of β CrB B measured from P1640 NRM data. We overplot the spectra of two F dwarf stars from the IRTF Spectral Library: HD 26015 (F3V) and HD 27524 (F5V).

and 4.9 to confirm these results in our NRM data. For the secondary, we compared F3V and F5V spectrum examples from the IRTF Spectral Library. However, due to the lack of a sample of A stars in the IRTF library, we instead collected two appropriate reference spectra from the Pickles Atlas (Pickles 1998). In each case, we smoothed the reference spectrum to the P1640 data cube resolution, using the procedure described in §2.4.2.4. In both cases we found a fair match with the spectral types of Bruntt et al. Surprisingly, the match for the secondary is closer than the primary's, even though the flux data points of the latter spectrum were less sensitive to errors in the closure phase model. Most of the disparity in the primary spectrum is in points susceptible to the telluric water absorption band between the *J* and *H* photometric bands. These points are distinguished in the plot by

gray shading. Presumably, it is by mere chance that the flux calibration errors skewed in such a way that the F-dwarf spectrum remains smooth across the telluric channels.

4.7 Dynamic Range Estimation

Commonly, the dynamic range of an optical interferometry observation is estimated by applying a Monte Carlo method to an empirical noise model (e.g., Ireland et al. 2006). In the case of AO-assisted NRM observations of relatively bright targets, detection limits are typically set by systematic errors in closure phase calibration rather than measurement scatter (e.g., Kraus et al. 2008; Hinkley et al. 2011a). Therefore it is not surprising that in our experiment the uncalibrated systematic error components dominated the uncertainty in our deduction of the target source distribution. We know this is the case because the binary model fit residuals exceeded the uncertainties in the closure phase means implied by the statistics listed in Table 4.2.

In order to build a complete model of the systematic noise, we would need to observe multiple calibrator stars to reveal the variances and covariances associated with this error component within and across the spectrograph channels. The correlations seen in Section §4.5 among the stochastic closure phase variations suggest that there are also strong correlations between underlying systematic errors, which would ultimately affect the detection limits. Since we were only able to observe one calibrator star for this data set, we assess our sensitivity with an alternative approach.

Rather than measuring detection limits from simulated data sets, we treat the amplitudes of spurious χ^2 valleys in the β CrB source model as proxies for dynamic range.

Assuming no true tertiary sources in the field are detectable in our β CrB data data set, the brightest false alarm revealed by a three source parameter grid search provide a measure that we expect to be roughly proportional to the detection limit. Although this does not provide a conventional detection limit, it at least allows us to quantitatively grasp how the sensitivity improves with the ensemble of spectrograph channels versus the single filter case.

We carried out a three source grid search on the calibrated β CrB closure phase data, with the parameters describing the known F-dwarf companion fixed at their best-fit values from Section §4.6. For the hypothetical tertiary source we tested a finely sampled range of positions inside two zones of separation centered on the primary star. The inner test annulus spanned separations between 33 mas and 99 mas ($0.5\lambda/D$–$1.5\lambda/D$ at 1.6 μm where D is the 5 m Hale Telescope aperture) and the outer annulus spanned angular separations 99 mas to 165 mas ($1.5\lambda/D$–$2.5\lambda/D$ at 1.6 μm). We determined the brightest proposed source within each annulus that *reduced* the χ^2 misfit statistic of Equation 4.22 as compared to the best-fit binary model. The misfit statistic was computed separately for the single 1.25 μm data cube channel, the 1.58 μm data cube channel, and the 20-channel closure phase ensemble. For simplicity, we fixed the tertiary source model contrast ratio across the passband when calculating the multi-channel fit.

The brightest spurious sources revealed by the grid search are tabulated in Table 4.4. The figures reveal significant improvement in dynamic range for the full NRM data cube as compared to the single channel case. In both zones, the strongest spurious signal was suppressed by a factor of 3–4 by including 20 channels spanning 1.16 μm to 1.73 μm,

Table 4.4. Contrast ratios of the strongest spurious point source signals in the β CrB NRM data.

Wavelength subset	Sep. 33 mas–100 mas	Sep. 100 mas–166 mas
1.25 μm (chan. 6)	14:1	17:1
1.58 μm (chan. 17)	10:1	19:1
1.16 μm–1.73μm (chan. 3–22)	47:1	64:1

[a]The contrast ratios are given for two zones of separation from the primary star.

[b]For reference, 66 mas corresponds to the λ/D angular resolution criterion of the Hale Telescope at 1.6 μm.

ultimately achieving a floor of contrast ratio 64:1 in the outer zone. For reference, in the case of direct AO-corrected imaging with the PHARO camera on the Hale Telescope, Metchev measured a 4σ detection limit of 10:1 at $2\lambda/D$ separation in K_s-band (Metchev & Hillenbrand 2009).

We emphasize that the dynamic range enhancement shown in Table 4.4 is not due to simply compounding the signal-to-noise ratio by summing data across cube channels. The spurious model solutions that set the noise floor are caused by systematic errors rather than signal strength-determined measurement scatter. It is the wavelength diversity enabled the IFU that enables us to reduce their influence.

4.8 Discussion of Noise Sources

Although we find that the wavelength dimension provided by the IFU improves the dynamic range of our NRM data, our contrast limit remains over one order of magnitude worse than the best performance of AO-assisted aperture mask observations published to date (e.g., Kraus et al. 2008; Hinkley et al. 2011a). We attribute this largely to uncalibrated

systematic closure phase errors. Earlier, when we considered the fit residuals of the binary star β CrB model, we found that in the 1.58 μm channel (one with relatively high signal-to-noise ratio) there were 15 closure phases with residuals above 10 degrees, and when they were excluded from the fit the RMS across all the residuals was still 4.5 degrees. By comparison, Hinkley et al. (2011a) controlled these errors to under one degree.

There are two main categories of systematic errors we can imagine in our experiment: those originating from the instrument, and those introduced during the data extraction. On the instrument side there is potential corruption of closure phases from optical misalignments and aberrations. We carried out simple Fresnel diffraction simulations with PROPER, the IDL software package created by Krist (2007), to examine the influence of these effects.

First we considered the effect of the pupil mask inclination, one of the problems we noticed in our data. In a PROPER simulation we tested the closure phase accuracy of a simple three-hole mask. We set the geometric scale of the pupil mask and the focal length of the focusing optic (600 mm) to be the same as in our instrument. We found that for a perfect, on-axis, monochromatic ($\lambda = 1.6$ μm) wave front, the closure phase deviates less than half a degree from zero for a mask inclination as high as 15 degrees. Similarly, shifting the entire mask by several millimeters along the optical axis produced no significant closure error. Therefore, we do not consider mask alignment to be a major systematic noise source in our instrument.

Using the same model in PROPER, we tested the effect of phase and amplitude aberrations. We found that a Zernike phase mode of defocus alone, up to a realistic magnitude

(0.25 μm), had negligible effect on the closure error. However, when combined with amplitude gradients of order 20% across each mask subaperture, a defocus mode of scale 0.25 μm generates a 2-degree closure error. Since amplitude gradients alone contributed no errors, it appears that the combination of phase and amplitude aberrations, at levels plausible in an AO-corrected beam, can mutually reinforce to produce significant closure errors.

Due to the numerous steps required to extract data from the focal plane image of an integral field spectrograph, we must contend with error sources that exist in neither conventional imaging nor spectroscopy. Several of these are described in Section§ 2.4.2.5. For the case of closure phase measurement, our accuracy depends on the ability to discriminate the position and spatial frequencies of the fringes composing the interferogram. Cross-talk is one of the error sources that directly degrades this measurement, by confusing the fringe signals from different baseline and wavelength combinations. While we have mitigated the effect of cross-talk on visibility extraction to a large extent with our method described in § 4.4, for some closure triangles we would expect it to remain a concern.

Also in § 4.4, we described how the weighting of the focal plane signal used to determine the flux in a cube spaxel is sensitive to the profile of the raw microlens spectrum on the detector in the dispersion direction. Although the dispersion-direction profile of the raw microlens spectrum has a fairly predictable mean shape determined by the target star's spectrum, it also varies strongly between neighboring microlenses due to the inherently sharp interferogram structures occurring on a scale of 2–4 spaxels. It is conceivable that the resulting corruption in extracted visibility data was enough to contribute significant systematic errors. Future experiments with different cube extraction weighting schemes could

isolate the magnitude of this effect.

4.9 Conclusions

We have carried out the first observation combining non-redundant aperture mask (NRM) interferometry with integral field spectroscopy. The added wavelength dimension of our closure phase data set enabled us to retrieve the low-resolution near-infrared spectrum of the F-dwarf secondary component of β CrB, a well-studied spectroscopic binary star. To our knowledge, such an accurate spectrum retrieval at $\sim 2\lambda/D$ angular separation is out of reach of other existing high contrast techniques. Our result is consistent with a long history of radial velocity, astrometry, photometry, and long baseline optical interferometry measurements of the binary system.

The implementation of NRM with an integral field spectrograph (IFU) requires special care to mitigate systematic error sources unique to closely packed IFU data, in particular cross-talk between neighboring focal plane spectra. We have outlined a simple solution to compensate for this effect which offers significant improvement in closure phase accuracy for channels with relatively low signal strength. Another calibration aspect that is more critical with spectrally-resolved NRM than the case of direct/coronagraph IFU imaging is the accurate determination of the channel-wavelength relationship.

Despite our efforts, relatively large systematic calibration errors persisted in our closure phase data, severely limiting the overall dynamic range of the observation. Although we investigated several possible causes, we were unable to settle on a satisfactory explanation for the large residual errors present in our β CrB binary model fit (∼9 degrees RMS

across all closure triangles and channels). However, we did confirm an anticipated boost in contrast limits for spectrally-resolved closure phase data set as compared to a single filter observation. In our case this improvement reduces the noise floor down by a factor of 3–4 at angular separations between $0.5\lambda/D$ and $2.5\lambda/D$. Future experiments are needed to determine if NRM observers can take advantage of this enhancement without suffering from net losses in sensitivity due to the complex noise properties of IFU data.

Chapter 5

Related Work

5.1 The Project 1640 Phase I Survey of Young, Nearby Stars

Neil Zimmerman, Ben R. Oppenheimer, Sasha Hinkley, Justin Crepp, Ian R. Parry, Stephanie Hunt, Charles Beichman, Lynne Hillenbrand

Between July 2008 and July 2010, the Project 1640 collaboration carried out a survey of young, nearby stars at the Hale Telescope. The primary goal was to probe the new parameter space in contrast and angular separation enabled by the coronagraphic IFU to detect and acquire low-resolution spectra of faint companions. We note that since the instrument was designed for a newer AO system that will not begin full operation until 2012, we did not expect to reach optimal performance.

High priority targets were drawn from two main categories. First, bright, nearby stars

of all spectral types exhibiting some form of published youth indicator. Second, particularly towards the end of Phase I observations, we focused on a volume-limited A-dwarf sample.

In total, we had 27 useable nights on the sky, and acquired useful data on 128 stars. We graded our data either 'good', 'fair', or 'poor' based on subjective assessment of speckle clarity. Under the best seeing conditions and AO performance, resulting in 'good' data, the speckles are sharp and well-defined across all channels of the data cube (Figure 1.3 is an example of this level of data quality). In 'fair' data cubes, the speckles are slightly blurry at the blue end of the passband. In 'poor' data, which we do not consider useful for faint companion detection, the residual starlight forms a bright, smooth halo around the coronagraph mask, as a consequence of severe wave front errors.

5.1.1 Young Stars

The youngest stars (age $<\sim 1$ Gyr) are the likeliest to host luminous exoplanets within our detection limits (after full reduction, a 5σ contrast limit of 2×10^{-5} at 1" in the *H* band for the best data; Crepp et al. 2011). At this stage in their evolution, gas giant planets radiate thermal energy derived from the release of gravitational potential energy (e.g., Burrows et al. 1995; Beichman et al. 2010). Therefore, throughout our Phase I observations, we preferentially targeted younger stars. Besides using published youth indicators to select this subset of the catalog, we required the star to be accessible as a natural guide star for the Hale Telescope AO system. This sets boundaries in brightness ($V_{mag} < 13$) and Declination ($-13 < \delta < 78$).

Table 5.1 gives a summary of the 197 stars in the young star subset of the Phase

Table 5.1. Summary of young stars in the Project 1640 target catalog.

Association	Number	Distance Range (pc)	Age range (Myr)
unassociated	117	< 80 [a]	< 1000
Ursa Major	32	$9 - 80$	~ 300
AB Doradus	21	$20 - 55$	~ 50
Taurus-Auriga	16	~ 140	pre-main sequence
β Pictoris	9	$25 - 45$	~ 10
Tucana-Horologium	2	~ 50	~ 30

[a]In the 'unassociated' category, we included three exceptional debris disk stars at distances beyond 80 pc.

I target catalog. As stellar kinematics and stellar age-determination are active areas of research, there are without a doubt numerous new stars that could be added to this sample today. Of all the stars in Table 5.1, 25 have resolved circumstellar disks. Besides the stars in moving groups (see Zuckerman & Song (2004)), other stars with young age estimates have been gathered from the documents related to the Spitzer telescope's Formation and Evolution of Planetary Systems (FEPS) survey (Meyer et al. 2006), and studies of mid-IR excess from A stars (Morales et al. 2009).

We succeeded in acquiring 75 stars in the young star subset of the target catalog. Of these, 55 have at least one 'good' data quality set while the rest are of 'fair' grade.

5.1.2 A-Star Survey

Stars in the A spectral class are attractive for high-contrast imaging surveys for several reasons. First, if their spectral type confidently identifies them as main-sequence, then we know they are younger than ~ 1 Gyr. Second, they are relatively luminous, so that they

can function as natural guide stars for AO acquisition, out to relatively large distances as compared to stars of lower mass. Beyond this, strong evidence has accumulated in the last several years for a positive correlation between stellar mass and planet frequency, mass, and orbital scale (Johnson et al. 2010). Based on these trends, Monte Carlo simulations of high-contrast imaging survey yields suggest that at a given contrast limit (e.g., 10^{-6}), A-stars will have the highest planet detection rate per star out of any spectral class (Crepp & Johnson 2011).

Although there have been numerous high-contrast imaging surveys in the last five years, most have targeted either solar-type stars and young stars across all spectral types (e.g., Lafrenière et al. 2007; Metchev & Hillenbrand 2009; Chauvin et al. 2010b; Liu et al. 2010). The published surveys that have targeted A-stars either exclusively observed stars at Austral declinations (Ehrenreich et al. 2010) or had relatively shallow detection limits ($\sim 5 \times 10^{-4}$ contrast at $1''$; de Rosa et al. 2011).

A table summarizing the P1640 A-star targets is reproduced in Figures 5.1 and 5.2. At the end of Phase I, 18 of the 71 selected A stars within 45 pc were acquired with 'fair' or better data quality. So far, the only new object found in the A-star data subset is Alcor's M-dwarf companion (see Chapter 3). However, the data reduction with the speckle suppression pipeline Crepp et al. (2011) is incomplete, so further work is needed to determine if other, fainter sources were detected. Although 18 stars is not enough to warrant general conclusions of substellar companion frequency, we do plan to share our methods and the resulting detection limit curves with the wider community.

P1640 A Star Survey

last updated 2011 June 13

original Hipparcos query: **DEC(ICRS): "-13 & <78"\ AND (Plx: ">10") AND (SpType: "A*")**
manually excluded results with Vmag > 7 (from AQ, an FOV star at 50 pc would have m_V = 6.2)
manually excluded double/multiple systems having an unocculted component in the P1640 F.O.V. (0.15" < rho < 3")
2009 Nov 20: set 45 pc parallax distance cutoff => 86 stars total
Special entries were made for Castor A and B, since the two were treated as a single star by Hipparcos.

The target count and the amount acquired with Fair or better data quality, binned by survey radius:

dist:	<10	<15	<20	<25	<30	<35	<40	<45
count:	2	3	5	8	9	10	12	15	18
excl:	2	3	5	8	16	30	39	53	71

The mult. column contains a multiplicity flag:
D = entry in the Washington Double Star catalog
SB = entry in the 9th Catalogue of Spectroscopic Binary Orbits (Pourbaix et al 2009)
The rho column indicates the most recent separation measurement in the W.D.S. catalog of the closest component in the system.
The spectral types were taken from the Hipparcos catalog. Giants manually filtered out based on V-band absolute mag.

The qual column indicates the quality of the data obtained, rating by speckle definition:
G = good, F = fair, P = poor
The re-obs column indicates "Y" if the star has been flagged for a repeat observation.

P1640 #	name	HIP	RA (J2000)	Dec (J2000)	Vmag	Jmag	Hmag	pi (mas)	dist (pc)	Abs Vmag	Spec Type	age (Gyr)	young	exopl.	mult.	rho (")	date1	date2	date3	date4	date5	qual	re-obs.	notes
60068	HD 5448	4436	00 56 45.212	+38 29 57.64	3.86	3.62	3.65	23.9	41.8	0.8	A5V		0	0	D	28.5								
30057	HD 1404	1473	00 18 19.657	+36 47 06.81	4.51	4.35	4.42	23.1	43.3	1.3	A2V	0.3	1	0										Morales A star
30002	HD 11636	8903	01 54 38.409	+20 48 28.93	2.64	2.34	2.35	54.7	18.3	1.3	A5V...	0.78	1	0	SB		10/08					F		
60036	HD 6961	5542	01 11 06.162	+55 08 59.64	4.34	4.45	4.28	23.7	42.1	1.2	A7Vvar		0	0	D	130.0								
60069	HD 14055	10670	02 17 18.867	+33 50 49.90	4.03	3.8	3.86	27.7	36.1	1.2	A1Vnn		0	0			09/09					P		
60154	HD 20320	15197	03 15 50.025	-08 49 11.03	4.80	4.42	4.26	27.2	36.8	2.0	A5m		0	0	SB									
60125	HD 23281	17395	03 43 33.834	-10 29 08.38	5.59	5.21	5.17	23.3	42.9	2.4	A5m		0	0										
60047	HD 19107	14293	03 04 16.516	-07 36 03.09	5.26	4.87	4.83	23.2	43.1	2.1	A8V		0	0										
30207	HD 27045	19990	04 17 15.661	+20 34 42.93	4.93	4.79	4.58	34.9	28.7	2.6	A3m	0.193	1	0	D	180.0								
30205	HD 31295	22845	04 54 53.728	+10 09 03.00	4.64	4.85	4.52	27.0	37.0	1.8	A0V	0.01	1	0	D	39.7								
30203	HD 25490	18907	04 03 09.380	+05 59 21.50	3.91	3.75	3.84	25.2	39.6	0.9	A1V	0.25	1	0			09/09					F		
60049	HD 27946	20641	04 25 25.015	+22 11 59.99	5.27	5.09	4.92	22.7	44.2	2.0	A7V		0	0	D	108.0	12/09					G		
60156	HD 28546	21039	04 30 38.890	+15 41 30.77	5.47	5.46	4.97	22.6	44.3	2.2	Am		0	0	D,SB	162.0								
60051	HD 27819	20542	04 24 05.761	+17 26 38.87	4.80	4.56	4.51	22.4	44.7	1.5	A7V		0	0	D	146.0								
60057	HD 37594	26624	05 39 31.151	-03 33 52.94	5.99	5.42	5.36	24.2	41.4	2.9	A8Vs		0	0			09/09					F		
60060	HD 48097	32104	06 42 24.327	+17 38 43.09	5.20	5.03	5.07	23.4	42.7	2.0	A2V		0	0										
60175	CASTOR A		07 34 35.885	+31 53 18.20	1.88		63.3	15.8	0.9	A1V		0	0	D,SB	4.7									
60176	CASTOR B		07 34 35.98	+31 53 18.5	2.96	1.33	1.29	63.3	15.8	2.0	A2Vm		0	0	D,SB	4.7								
60061	HD 56537	35350	07 18 05.579	+16 32 25.38	3.58	3.54	3.5	34.6	28.9	1.3	A3V...		0	0	D	9.7								
60129	HD 56963	35643	07 21 17.498	+45 13 41.52	5.74	5	4.97	29.0	34.5	3.1	A7s		0	0										
30200	HD 71155	41307	08 25 39.632	-03 54 23.13	3.91	4.12	4.09	26.1	38.3	1.0	A0V	0.169	1	0			03/09					G		
60131	HD 78209	44901	09 08 52.256	+51 36 16.73	4.46	4.15	4.04	34.1	29.3	2.1	Am		0	0			03/10					P		
60044	HD 79439	45493	09 16 11.328	+54 01 18.69	4.80	4.48	4.35	27.6	36.3	2.0	A5V		0	0										
60159	HD 78362	45075	09 10 55.061	+63 30 49.08	4.67	4.07	3.93	26.8	37.3	1.8	Am		0	0	D,SB	52.0								
60160	HD 85376	48390	09 51 53.038	+24 23 43.33	5.29	4.86	4.72	24.9	40.2	2.3	A5IV		0	0			12/09	03/10				F		
30211	HD 87696	49593	10 07 25.762	+35 14 40.90	4.49	4.27	4.05	35.8	27.9	2.3	A7V	0.39	1	0			03/09					G		
30031	DENEBOLA	57632	11 49 03.578	+14 34 19.42	2.14	1.85	1.92	90.2	11.1	1.9	A3Vvar	0.05	1	0	D	39.7	03/09					G		
30029	ZI 877	54872	11 14 06.501	+20 31 25.38	2.56	2.24	2.19	56.5	17.7	1.3	A4V	0.71	1	0	D	46.5								
30027	MERAK	53910	11 01 50.477	+56 22 56.74	2.34	2.27	2.36	41.1	24.3	0.4	A1V	0.51	1	0										
60046	HD 103287	58001	11 53 49.847	+53 41 41.14	2.41	2.38	2.49	39.0	25.6	0.4	A0V SB		0	0										
60074	HD 102124	57328	11 45 17.040	+08 15 29.23	4.84	4.63	4.54	27.3	36.6	2.0	A4V		0	0										
60132	HD 95608	53954	11 02 19.775	+20 10 47.43	4.42	4.32	4.32	26.4	37.9	1.5	A1m		0	0			12/09					P		

Figure 5.1 Phase I A-star survey, page 1 of 2.

| | | |

5.2 Solinascope: a New Concept for Starlight Rejection

Neil Zimmerman, Ben R. Oppenheimer, Rémi Soummer, Laurent Pueyo &

Richard G. Lyon

5.2.1 Introduction

The solinascope (name derived from the Greek word for “pipe”) is a novel instrument concept that exploits the properties of near-field diffraction to enhance the isolation of a faint companion signal. By suppressing light outside a small angular area centered on the target, the solinascope allows one to separate the light originating from the object of interest from that of the host star. The purity of this signal is achieved at the expense of all spatial information. Therefore, in its basic configuration it is not a survey tool, but rather an instrument well suited for follow-up spectral characterization of planet candidates. In the solinascope, rejection of off-axis starlight is accomplished through free-space propagation between a series of baffles aligned along an axis. We conducted a range of laboratory tests and optical simulations to explore the practical benefits of this concept. We found that two configurations of the solinascope were well-motivated; one provided a modest improvement in the contrast limit over a direct image, while the other did not succeed. A wide range of design parameters remain to be tested.

5.2.2 Double-Baffle Configuration

Our initial solinascope design, motivated by preliminary calculations, consisted of a single pair of aligned, identical baffles. The baffles, of diameter d, are space apart by distance

d^2/λ. Because of this separation, one baffle subtends an angle of λ/d from the position of the other as long as $d \gg \lambda$. The entrance aperture of the solinascope is positioned at the exit pupil of the telescope, after all adaptive optics and starlight suppression components. If d is matched to the exit pupil of the telescope of aperture D, then in the geometric ray approximation, only rays originating from the sky within an angle of λ/D will pass through the exit baffle of the solinascope. However, the wave-like nature of light must be taken into account to fully appreciate the nature of the device.

Significantly, the baffle separation d^2/λ is at just the length used to discriminate the near- and far-field regimes of diffraction. These regimes represent successively crude approaches to solving the scalar time-independent wave equation. To see where they arise from and what their consequences are, we start from the the integral formula expressing the scalar amplitude of the wave, u, at a point $P = (x_p, y_p, z_p)$ behind an illuminated aperture σ:

$$u(x_p, y_p, z_p) = -\frac{i}{\lambda z_p} \iint_{\sigma} e^{ikr}\, dx\, dy. \tag{5.1}$$

Here r is the distance from the observation point P to the area element on the aperture plane. For simplification, we have assumed that the plane wave incident on the aperture is of unity amplitude, that $z_p \gg d \gg \lambda$, and that the direction cosines of the vectors connecting P to the various points on the aperture plane have negligible effects on modulating the amplitude contributions of the integrand. The path differences do, however, come into effect in the complex exponential factor (Born & Wolf 1980).

Let point $Q = (x_q, y_q, 0)$ on the aperture correspond to the point on the aperture for which we are evaluating the integrand. Then r can be expressed in terms of the coordinates

of P and Q: $r = \sqrt{(x_p - x_q)^2 + (y_p - y_q)^2 + z_p^2}$, which can be rewritten as

$$r = z_p - \alpha x_q - \beta y_q + \frac{x_q^2 + y_q^2 - (\alpha x_q + \beta y_q)^2}{2z_p}, \tag{5.2}$$

where α and β are the direction cosines of the vector from the origin to P in the x and y coordinates, respectively (Sommerfeld 1954). The fraction with the quadratic terms in the numerator is negligible if the largest contributions, $\frac{x_q^2}{2z_p}$ and $\frac{y_q^2}{2z_p}$, are much less than $\lambda/2$, so that $z_p \gg x_q^2/\lambda$ and $z_p \gg y_q^2/\lambda$. Equivalently, for a circular aperture of diameter d, $z_p \gg d^2/\lambda$. This limit, where the phase can be expressed linearly in terms of the aperture coordinates, corresponds to the Fraunhofer, or far-field regime of diffraction. Conversely, at shorter distances, the quadratic terms cannot be dropped; this is the Fresnel, or near-field regime.

In the near-field, most constructive interference occurs between the axis of propagation and the geometric shadow of the illuminated aperture. Therefore, the length of the solinascope is such that beam spreading is kept favorably low. This lends some justice to the simplistic geometric ray picture of the solinascope's operation. On the other hand, if the baffle separation was at a length in the Fraunhofer regime of the aperture size, the width of the beam would expand linearly with propagation distance. At the exit pupil, such wave front spreading would lead to confusion with plane waves arriving from off-axis sources that we are trying to reject. Arguments explaining why the near-field spreading of a wave front is constrained to around the width of the aperture are available from Thorne (2004) section 7.2.2 and Klein (1970) section 8.2.C. We may also be unwittingly familiar with the acoustical analog to this phenomenon in everyday life: consider how common audio

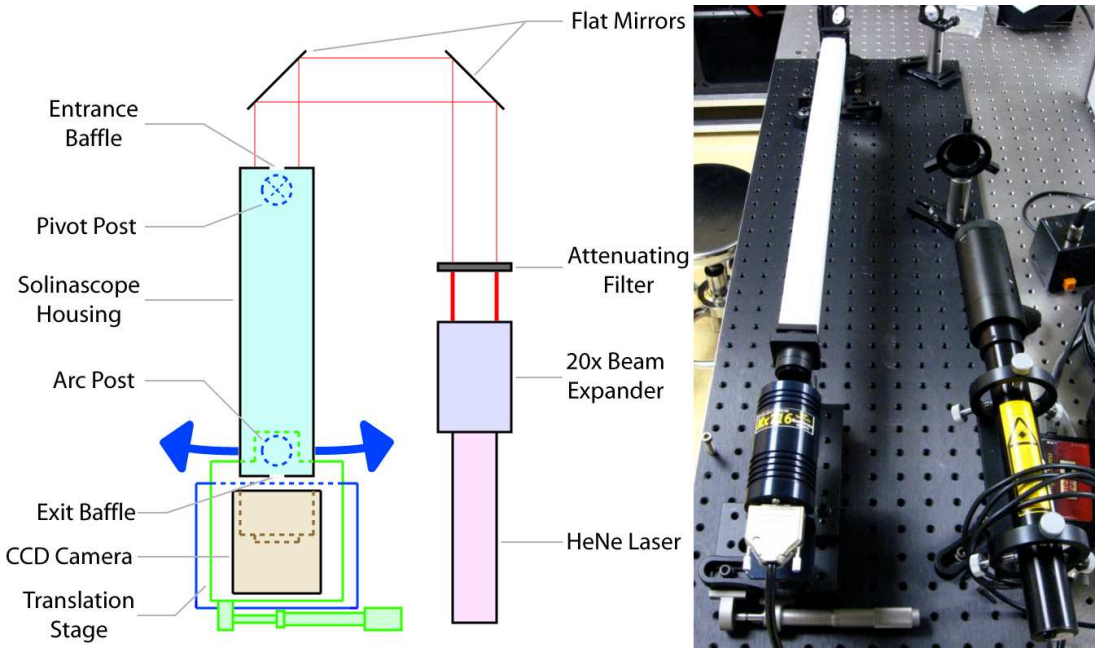

Figure 5.3 Schematic and photograph of the double-baffle solinascope experiment in the AMNH Astrophysics Laboratory. An expanded laser beam emulated an ideal plane wave source. We used a translation stage to tilt the solinascope with respect to the beam in order to examine throughput for a range of incidence angles.

speakers direct high pitches into narrower cones than low pitches. For a given speaker diameter and listener distance, the far-field approximation becomes increasingly valid for longer wavelengths (Blackstock 2000).

We designed an experiment to characterize the rejection of off-axis light by measuring the throughput of the double-baffle solinascope as a function of the incidence angle of a collimated, decompressed laser beam. Although we eventually found this configuration to be unsuccessful, we record the details of the experiment here for the benefit of future investigations of this kind.

The setup is shown in Figure 5.3. In our scaled-down laboratory prototype, the baffle opening (which in operation would be matched to the telescope or coronagraph exit pupil)

was 0.6 mm and the baffles were separated by a length of 56.9 cm. Given our light source, a HeNe laser operating at a wavelength of 632.8 nm, this length was equivalent to the d^2/λ spacing discussed above. We constructed the solinascope prototype by mounting precision pinholes onto an assembly of standard opto-mechanical fittings. The body of the solinascope, serving to keep the pinholes aligned, was an aluminum tube of 29 mm inner diameter. We lined the inside surface with black flocked paper to minimize reflections from stray light.

The 20$\times$ beam expander attached to the laser increased its width to 13 mm and improved its collimation. During measurements in configurations with large throughput, we found it was necessary to place a low transmission neutral density filter (T = 3×10^{-5}) in the path of the beam in order to accommodate the saturation limit of the detector. Before illuminating the entrance pupil of the solinascope, the beam was deflected by two flat mirrors on gimbal mounts. The flat mirrors served not only as a way to maximize the use of space on the workbench, but also to permit precision alignment of the beam with the solinascope. Each gimbal mount had two axes of fine manual tilt adjustment.

We mounted the back post of the solinascope and the CCD camera facing the exit aperture onto a micron-precision translation stage. In a given trial, once we had aligned the solinascope with the beam, we adjusted the translation stage to the positions corresponding to a range of incidence angles, imaging the exit pupil at each position. To enable this motion, we mounted the front end of the solinascope loosely enough on its threaded post that it would act as a pivot point. In addition, we mounted the back post coupling the solinascope to the translation stage via a slot that permits travel in the direction perpendic-

ular to the translation, accommodating the arc that it must trace out over the course of the trial. At the extreme of our measurements, this arc extended up to 2.4° from the beam axis, corresponding to an incidence angle of $40\lambda/d$.

To achieve alignment of the zero incidence angle position before each trial, we first roughly adjusted the second mirror and the translation stage so as to maximize the illumination on the CCD as perceived with the naked eye. Next, we refined the alignment by taking test exposures of the exit pupil while iteratively tuning the position until the disk showed maximum symmetry upon inspection.

Throughout our measurements, we used a 16-bit, thermoelectrically cooled, 376×290 pixel CCD camera to image the exit pupil of the solinascope. At a distance of 35 mm from the back pinhole, the 6.5×4.8 mm detector easily encompassed the detectable extent of the transmitted diffraction pattern. During the trials, at each incidence angle we set the exposure time of the CCD to the longest length possible without saturating any of the pixels, in order to maximize the dynamic range of the image. At incidence angles below $5\lambda/d$, the brightest parts of the image would saturate even for the minimum exposure time of 1 msec. Placing the neutral density filter in the beam for small incidence angle measurements solved this problem, although adding an extra step to the data calibration procedure. We processed the images using flat-field, dark, and bias frames in the same manner as in typical astronomical observations.

To measure the throughput of the solinascope at each incidence angle, the measurement we are interested in is simply the total integrated flux from the exit pupil. Therefore, on each of the final calibrated images, we carried out aperture photometry within a circle

centered on the region of illumination. The background was subtracted based on the median pixel value an the annulus surrounding the photometric aperture. In order to prevent hot pixels from systematically skewing the integrated flux measurement, we processed the images with a 3×3 pixel median filter before the photometry procedure.

Our measurements indicated that there was no significant deviation in off-axis intensity fall-off from the case of a very high-Strehl (95%) Airy disk. Later simulations confirmed that with the d^2/λ baffle separation we employed, the diffraction pattern incident on the exit baffle is, for practical purposes, identical to the far-field PSF of the aperture. Therefore, the exit baffle of the double-baffle solinascope merely masks a region from the image of angular width λ/d.

5.2.3 Spatial Filter Configuration

In a second version of the solinascope, depicted in Figure 5.4, the baffle separation is shortened to a fraction of the Fresnel length, and the exit baffle light is focused by a lens. The motivation of this configuration is to passively enhance the telescope's AO system by filtering out high spatial frequency aberrations in the pupil plane (those beyond the AO system's control).

We tested this concept using IDL PROPER simulations (Krist 2007), trying baffle separations between $d^2/(20\lambda)$ and $d^2/(2\lambda)$. To use realistic wave front perturbations at the entrance baffle, we passed Kolmogorov phase screens through high-pass filters to approximate snapshots of AO-corrected wave fronts. The residual phase errors were tuned to simulate Strehl ratios between 1% and 80%.

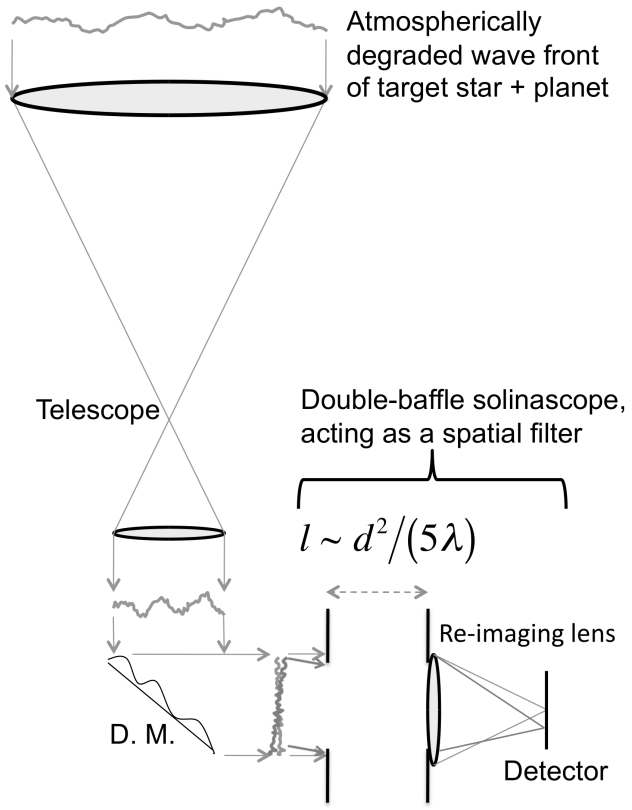

Figure 5.4 In this spatial filter configuration, the entrance baffle is matched to the exit pupil of the AO system (symbolized by the deformable mirror). After the target's light propagates through two baffles of some separation less than d^2/λ, where d is pupil diameter, a lens forms the filtered image of the star.

In this near-field regime of propagation length, the wave front exhibits strong phase structures at the exit baffle. We found that these aberrations preclude the possibility of improving any aspect of the telescope wave front. To assess the performance, for each wave front realization we compared the peak intensity of the PSF in the image after the solinascope filter to the peak intensity of the PSF if the image had been formed directly. We normalize this ratio to the overall throughput of the solinsacope filter, so that we are only evaluating the sharpness of the filtered image. We give the results for entrance wave fronts of Strehl ratio 0.8 in Table 5.2. The test star's PSF is broadened in all cases, worsening the

Table 5.2. Ratio of peak PSF intensity in filtered image to peak PSF in unfiltered image

Baffle separation (d^2/λ)	1/2	1/4	1/8	1/16	1/32
Peak intensity ratio	0.53	0.58	0.64	0.69	0.74

[a]The entrance wave front Strehl ratio was 0.8 in all of these trials.

[b]The intensity ratio is normalized to the throughput of the solinascope filter.

[c]Baffle separations are specified in multiplicative factors of d^2/λ.

dynamic range relative to the normal telescope image.

5.2.4 Multi-Baffle Configuration

Our third version of the solinascope consists of several baffles bunched together at relatively short separations, with the detector positioned out at the original Fresnel length (d^2/λ) distance. Figure 5.5 shows a diagram of this configuration. As in the case of the double-baffle solinascope, no image is formed from the exit baffle. We are mainly interested in the ratio of the energy from the on-axis planet to the energy of the off-axis star at the exit baffle, as compared to the direct image.

In the most successful arrangement, the baffles have an inverse arithmetic spacing. For example, suppose the widest gap, between the last baffle and the detector, is d^2/λ, then the preceding gap is $d^2/(2\lambda)$, preceded by $d^2/(3\lambda)$, etc. If the last gap is $d^2/(5\lambda)$ then the total solinascope propagation length is $2.28d^2/\lambda$ in this case.

With 100 phase screen realizations simulating a Strehl ratio 0.5, we evaluated the off-

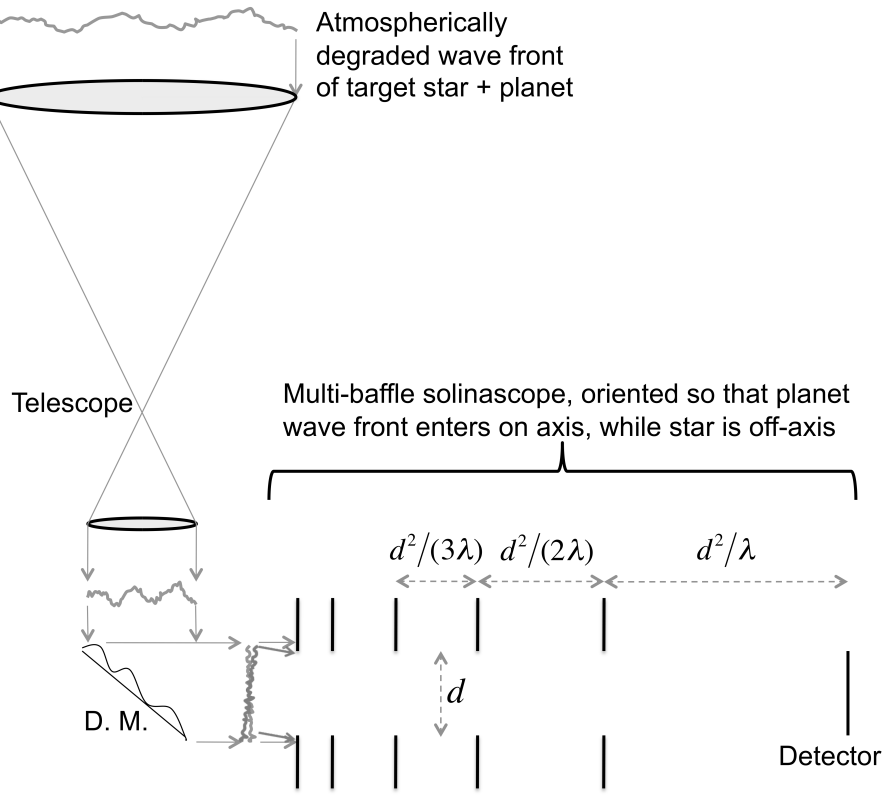

Figure 5.5 In the multi-baffle configuration of the solinascope, the baffle axis is aligned with the planet, so that the host star's off-axis light is rejected. The baffle separations are prescribed by an inverse arithmetic pattern, with the length of the final and longest stage equal to the Fresnel length (d^2/λ).

axis starlight rejection of a six-baffle solinascope. We consider the target scenario of a planet at angular separation $5\lambda/D$ from its host star. For these conditions, we found that on average, the planet-to-star signal ratio was increased by a factor of 3 over the direct image. The throughput was 6%.

Since there is a wide scatter in off-axis starlight rejection between the wave front realizations, it is necessary to average the results over a large ensemble of phase screens. Unfortunately, this means that it is computationally expensive to explore design parameters. Presently we can offer a few broad observations: including more than 6 baffles leads to only

marginal improvement in rejection, and decreases the throughput of the planet signal. The off-axis starlight rejection improves significantly with Strehl ratio (roughly a factor of 2 gain in planet-to-star signal when Strehl ratio is increased from 0.5 to 0.8). Preliminary results also indicate that changing the baffle shape to a square aperture (a square inscribed inside the circular pupil) may improve the starlight rejection, as compared to a direct image formed after either a square or circular (normal) telescope pupil.

The benefit of the multi-baffle solinascope configuration can be qualitatively understood as follows. At each successive baffle, phase aberration modes above a certain spatial frequency are attenuated. The longer the propagation distance, the lower the maximum spatial frequency that is transmitted at full strength. Therefore, each baffle is effectively a low-pass filter on the wave front phase profile with a successively lower cutoff frequency. For an off-axis star, the overall throughput is worse relative to the on-axis planet. This is because inside the second baffle opening, the star signal is already preferentially represented by higher spatial frequencies modes which will be more severely attenuated than the lower spatial frequency wave front of the on-axis planet.

5.2.5 Summary

Although no immediate practical application of the solinascope is at hand, the progress made to date is worth bringing to the attention of the larger astronomical community. The multi-baffle version is especially remarkable, providing a means to improve the rejection of the starlight contaminating an exoplanet signal by a factor of ~ 5. Further exploration of the large design parameter space—in particular, different combinations of baffle spacing—

could lead to even more compelling performance predictions.

Appendix A

A.1 Project 1640 Observation Procedures

Here we describe the procedure for observing with Project 1640, once the instrument has been cooled, mounted, and all cables and communication links for the Cassegrain cage are in place.

A.1.1 System Initialization

After the Data Acquisition workstation has been powered on, log in with the user/password p1640/p1640. Load the LabVIEW control panel (LOCATION, FILENAME?). If configured properly, the Lab View front panel will indicate the dewar temperature, which at this point should be near 78 +/- 1 Kelvin for both the detector and the plate.

Find the System Init menu tab at the lower left corner of the panel. Turn on the DAC machine with the power button. After it finishes booting, hit the Launch Camera Servers button. This will open three terminal windows and a ds9 window for displaying the most recent detector image. Unfortunately, the DAC machine may have to be rebooted many times before it initializes properly. Once it is working, the user should leave it on for the duration of the observing run. Next hit the RST, RCO, Init button to initialize the camera. Next, power on the detector.

In order to minimize the amount of charge that builds up on the detector when it is left idle, there is a mode of operation implemented in the control panel called Maintenance

Mode. Switching this on will cause the detector to be continuously read when not taking data. We recommend switching on the Maintenance Mode before beginning a night of observations, at least one hour before taking any science or calibration data. Make sure that Maintenance Mode is switched on whenever data is not being taken.

In addition to the LabView control panel, a separate application called the AO Paddle needs to be launched in order to permit small changes to the instrument pointing. To start this, open an xterm on the Data Acquisition workstation. Run the following commands:

```
$ssh X aousr@harbor.palomar.caltech.edu
(enter password ao$usr)

$idl

IDL> aopaddle
```

Now select P1640 from the instrument menu, and the AO paddle will be ready to step the instrument pointing by an adjustable angular increment in any cardinal direction. The beginning of every Project 1640 observing run requires especially close coordination with the Palomar Adaptive Optics (AO) System operator. There is a fair chance that both the beam alignment and the Zernike polynomial coefficients of the AO system will need to be tweaked, requiring the Project 1640 user to take a series of test images of a white light source built into the AO system. The user should plan to dedicate roughly one hour of the start of every observing run to optimizing the optical interface with the AO system.

Before astronomical observations begin, power on the Data Analysis workstation and log in as DataAnalysis/abaur. This machine is useful for a second observer to process and inspect incoming data. The disk drive of the Data Acquisition machine can be mounted from the Data Analysis machine over the ethernet network, facilitating rapid transfer of data. To take advantage of this capability, open a Finder window on the Data Analysis workstation, select SHARED, select p1640, and connect with user/password p1640/p1640.

A.1.2 Target Catalog

The Project 1640 target catalog will inevitably grow over the lifetime of the instrument as new objects of interest are added. Here we outline the procedure for loading a new version of the target catalog into the data acquisition interface and the Palomar Telescope Control System.

The LabVIEW control panel expects a catalog stored as a Microsoft-format .csv file. Example files are stored on the Data Acquisition workstation. The location of the current catalog file can be viewed in the LabVIEW control panel by opening the Paths tab in the lower left corner. By placing the new catalog at the same location, the user can replace the old catalog. To load the new catalog into the interface, restart the LabVIEW control panel. The user can verify that the new catalog is in place by checking for the existence of one of the new entries. To do this, enter either the HIP number or another identifier in the box in the Star Catalog area in the lower right corner of the front panel. The coordinates and other observational data of the requested star should appear.

In order to observe targets in a new version of the catalog, the AO operator needs to load his own version of the new catalog into the main telescope control system. The perl script makePal.pl takes the .csv target catalog file and produces a text file catalog in the Palomar-specific format. This is accomplished with the following command:

```
$./makePal.pl MS_format_catalog.csv
```

This will immediately produce the text file Pal1640-current date.txt in the current directory. Transfer this text file to the Palomar machine vulcan. This can be accomplished through a UNIX shell with an scp operation to vulcan.palomar.caltech.edu, using the username/password user/b34mmEU9. Be sure to tell the telescope operator the name and location of the new catalog file on vulcan, and have him check that the file is formatted correctly before observing begins.

A.1.3 Data Acquisition

Once the target catalog has been loaded, entering the HIP number or other identifying name in the object box will bring up a history of observations for that target. The history

will come up automatically when you set the image type, the number of observations, the integration time, and the number of reads. To prepare the instrument for the new target, hit the Set as Target Star button. Executing the Set as Target Star command loads the relevant target information into the appropriate .xml files that make up DAZLEs instruction set, and sets the values for the header of the FITS data files.

Tell the telescope operator the Palomar TCS number of the target, so he can slew the telescope and lock the AO system. Note that you should always switch off the atmospheric dispersion corrector (ADC) while the telescope is moving. A button on the right side of the front panel switches the ADC on or off.

Before an exposure sequence begins, the user can set the Image Type option to either CORE or OCCULTED, based on whether or not the star is currently behind the focal plane mask. The CORE and OCCULTED options are solely for the purpose of organizing the data; the focal plane mask remains physically fixed in place regardless. There is also a PUPIL option to form an image of the coronagraph pupil on the detector. Switching to and from PUPIL mode requires a few moments to allow the motors to position the optics appropriately. Monitor the indicator box underneath the Image Type switch to verify that the instrument is ready for the new exposure.

The user should carefully set the No. of Images and READS controls for each target. The camera reads occur in 7.7-second intervals. The No. of Images value dictates how many times the DAC will loop through the read sequence and produce an individual FITS file. A simple way to optimize the number of reads is to first acquire an exposure of minimum duration, two reads. Then, inspect the new image in the ds9 window. Measure the counts/sec values of the brightest pixels. Calculate how many 7.7 second reads can be accumulated without saturating (65,000 counts/sec). In practice, the P1640 team has found most occulted stars can be recorded with satisfactory count values using 5, 10, or 20 read exposures. Sticking to those exposure lengths also simplifies the data processing. After setting the number of reads, set the No of Images field to however many exposure loops are needed to reach the desired cumulative exposure time. For example, with 20 read exposures, setting the No of Images to 15 will result in a total of 7.721*15*20 = 2316 seconds (38.6 minutes) of exposure.

Hitting Expose starts image acquisition. Two indicator bars display the progress in the current exposure sequence. Once the desired number of images has been taken, the

history window changes to a note window where comments may be entered. During the acquisition of each exposure, an assortment of observational information is collected from the Palomar AO system. All relevant data (such as time, telescope position, and air mass) are written to the header of the corresponding FITS file.

After each image acquisition, the DAZLE software executes a script called `1640_export_data` in `/home/optics/ucam/bin`. This script uses FTP to move FITS files to the Data Acquisition workstation. The DAC informs the LabVIEW control panel that the file has been sent using the script `file_sent` in `/home/optics/ucam/data`. The Data Acquisition workstation listens over a designated port for the `file_sent` signal. Prior to sending the file, the Data Acquisition workstation is told that image acquisition is complete so that the software can grab the latest position settings.

After the exposure completes and the FITS file is transferred to the Data Acquisition machine, the new image appears in the ds9 window. The orientation of the image with respect to celestial coordinates is diagrammed in Figure 1, along with the relationship to the orientation of the lenslet array. Figure 2 shows an example of raw data as it appears in the ds9 window during observations.

Figure 1. Schematic showing how the data are oriented on the detector (upper left), on the lenslet array(upper right), and as it first appears in the DS9 window.

Between exposures, the observer can fine-tune the pointing with the AO Paddle (as described in section 1.1.1) in order to move the image of the target on the detector. This will be necessary, for example, to accurately occult a star with the focal plane mask or to move a stars point spread function to a favorable region of the detector. Once the observer verifies that the desired target is in the field of view, and that the AO correction is optimal, he should align the pupil of the coronagraph. This step is necessary before acquiring data on each target because the ADC prisms introduce a sky position-dependent shift in the pupil position. After switching to PUPIL mode, take a single exposure, and inspect the detector image. Ideally, the illuminated ring is round and symmetric in thickness. To adjust the pupil accordingly, change the pupil motor positions in Motor Control tab at the lower left corner of the front panel. Once the pupil is aligned, the observer can switch back to image mode to begin acquiring science data.

A.1.3.1 Acquiring Calibration Data

In order to enable useful measurements from the science data, it is necessary to acquire several pieces of calibration data during each observing run. By setting aside time for these tasks, the observer allows whoever is analyzing the data in the future to constrain the wavelength-dependent transmission of the atmosphere and the instrument, the spatially varying sensitivity of the detector, the bias/dark-current contribution to the detector signal, and the angular scale and orientation of the camera.

A.1.3.2 Core Exposures

Either before or after acquiring occulted data of every target star, the observer should record a sequence of unocculted core images. Core images are useful for photometric calibration. Before initiating the core exposure sequence, be sure that the star is well placed in the field of view. For the best quality core images, the stars image should be centered away from both the focal plane mask and the edge of the detector, preferably centered on one of the quadrants, so that a large area of the point spread function can be recorded. Keep in mind that despite the appearance of the raw focal plane data, the measurable extent of a bright stars diffraction pattern easily extends beyond a quarter of the detector diameter.

A.1.3.3 Spectrophotometric Reference Stars

In order to account for the wavelength-dependent transmission of the atmosphere and the instrument, during each observing run the observer should obtain a core exposure sequence of at least one star with a readily available reference spectrum. A suggested list of F and G stars has been compiled for this purpose, printed on a table titled IRTF Reference Stars. They are all stars that have publicly available spectra in the Infrared Telescope Facility (IRTF) Spectral Library. Also note these stars are dim enough (J mag ¿ 5.7, H mag ¿ 5.4) that the PSF core won't saturate the detector in a single read. Repeat 5 exposure loops for each spectroscopic standard star, preferably with the star centered in one quadrant of the detector.

A.1.3.4 Calibration Binary Stars

To enable high precision astrometry, it is necessary for the data analyst to constrain the plate scale and orientation of the science images. Observations of calibration binary star systems are the currently favored solution to this. It is necessary to use binary stars with well-determined orbits, so that the angular separation and orientation of the stars can be computed to adequate precision for the observation epoch. The Project 1640 team has assembled a list of binary stars (printed out on a table titled P1640 Calibration Binary Stars) that meet the criteria of (1) fitting in the field of view, (2) a brightness differences large enough so that the AO system can lock on one of the stars, and (3) an orbit well-determined and listed in the U.S. Naval Observatory Sixth Orbit Catalog. There are only a handful of binary systems meeting these criteria for a given time of the year, so the observer should acquire unocculted data of as many of these as possible on each run. Acquire 5 read sequences for each calibration binary.

A.1.3.5 Dark Frame

At some point during the run, at either the beginning or end of a night, the observer should record dark frames. Before doing this, make sure that the coronagraph window is covered. We recommend repeating 11 dark read sequences for each read length used during the run. For example, if the observer acquired science data in 10 and 20-read sequences, then they would take 11 x 10 reads and 11 x 20 reads in the dark.

A.1.4 Procedure Summary for Observing One Star

The following list summarizes the steps needed for a typical target star observation.

1. Immediately after the last exposure, switch on Maintenance Mode
2. Set the target in the control panel
3. Turn off the ADC
4. Tell the operator the slew to the chosen target

5. Switch coronagraph to Pupil configuration
6. Turn on the ADC
7. While the operator is locking the AO system, align the Pupil
8. Switch coronagraph configuration to Image mode
9. Switch exposure mode to Core and acquire Core images
10. Occult star using AO Paddle
11. Lock the tip/tilt system
12. Switch exposure mode to Occulted and expose

A.2 Project 1640 Data Reduction Procedures

A.2.1 Cube Extraction

The Project 1640 Cube Extraction Pipeline processes and calibrates the raw detector images to prepare the data for inspection and analysis. Most importantly, the pipeline extracts data cubes from the detector images (a product with two spatial dimensions, and a third in wavelength). The pipeline can run on any computer with a GNU C Compiler, the GNU Science Library, IRAF version 2.14 or newer, and a Perl interpreter for the initial configuration. For maximum efficiency during an observing run, we recommend a second observer oversee the operation of the Data Pipeline on incoming data at the Data Analysis workstation while the other observer leads the acquisition of new data with the main Project 1640 control panel. The username/password for the Data Analysis workstation is DataAnalysis/abaur, and the IP address is: 198.202.125.176

The Data Pipeline carries out the following steps:

1. Bad pixel and cosmic ray cleaning of focal plane mages.
2. Subtracts the bias, thermal and dark current from the focal plane images.

3. Flat fields the focal plane image based on dewar lamp data take in March 2010.

4. Performs a cross-correlation to align the detector plane data with the laser reference library (the projection of the lenslet array onto the detector vary with telescope pointing due to mechanical flexure).

5. Extracts a data cube from each processed focal plane.

6. Calibrates the flux in the spectral channels of the data cube to account for the transmission of the atmosphere and the response of the instrument.

7. Produces collapsed images by summing the slices of the extracted cube, facilitating the detection and photometry of faint objects.

A.2.2 Installing the Cube Extraction Pipeline

In order for the cube extraction pipeline to compile, two C libraries need to be installed: CFITSIO and GNU Science Library. CFITSIO is currently available from:
`http://heasarc.nasa.gov/docs/software/fitsio/fitsio.html`

Get the latest version of the UNIX tarball, and after unpacking it somewhere (home directory works fine), follow the standard UNIX installation described in the README (./configure, make, make install). Be sure to preface the make install command with sudo. The GNU Science Library is currently available from:
`http://www.gnu.org/software/gsl/`

After unpacking this, configure the installation with the disabled-shared option, as in: `$./configure --disable-shared` followed by `$sudo make` and
`$sudo make install`.

After obtaining the pipeline program tarball, unpack it in an appropriate location where it can reside permanently. Copy the lib subdirectory of the CFITSIO source code directory into the pipeline directory, overwriting the existing lib subdirectory. There is a subdirectory in the pipeline directory called include. Into include, copy the fitsio.h, fitsio2.h, and longnam.h header files from the CFITIO source code directory.

Next, you will need to edit a few file system paths in configure.pl, a Perl script located at the root of the pipeline source code directory. The following variables should be changed:

`$IRAF_PATH` is the file name of your IRAF interpreter (cl.e).

`$PIPELINE_PATH` is the full path to the directory where the pipeline source code and executable will reside.

`$DATA_PATH` is the directory where the processed data will be stored.

`$LIBRARY_PATH` is the directory of the pipeline library files. Initially these are located inside the pipeline directory.

`$IRAFSCRIPTS_PATH` is the directory of the IRAF scripts. Initially these are located inside the pipeline directory.

After those are set, run the Perl script on the command line:

```
$./configure.pl
```

This will produce a customized Makefile. By default, the Makefile links to an Intel Mac version of the CFITSIO library included in the pipeline tarball. If you're not using an Intel Mac, you'll need to modify this location to your own machine's installed version of CFITISIO.

Next, to compile the pipeline, run

```
$make
```

The program should compile with no errors or warnings. Last, to allow the IRAF scripts called by the pipeline executable to run, do

```
$mkiraf
```

to initialize a login.cl file in the pipeline directory.

A.2.3 Using the Data Pipeline

The newest version of the pipeline on the Data Analysis workstation is in the directory `~/proj1640pipe-2010april/`. Open an xterm and change to this directory. To test that the pipeline is installed correctly, you can run a test cube extraction by simply calling the executable with no arguments:

```
$./pipeline -o
```

This will produce one example data cube from a detector image in the library subdirectory, along with a sequence of comments directed to the terminal describing the various stages of processing. To run the pipeline on a directory called e.g. `/DATA/goodstuff`

containing a set of Project 1640 detector images, run

```
$./pipeline ../DATA/goodstuff/
```

The extracted cubes will be organized under the directory `/DATA/PROCESSED/` by target name and date. Within the date subdirectory, normal data cubes are stored in the subdirectory FITScubes or DATcubes, depending on the source file type (.fits or .dat). As an example, the full filename of one processed data cube could be `/DATA/PROCESSED/POLLUX/2008-10-25/FITScubes/POLLUX_C_2008-10-25_529.fits`.

There are a number of command line options to modify how the pipeline operates. The optional switches, placed after the input directory, are:

- -o for overwrite mode, which will overwrite data cubes that have already been made from the given raw focal planes
- -w to apply a crude spectral calibration to the data cubes
- -m to form a mean of the processed focal plane images from each exposure series and extract cubes from the results, in addition to processing the individual images
- -d for .dat file mode (which requires the .dat files corresponding to a given .fits file be in the given directory). In this mode, the pipeline forms a cube using slope fits to the individual bias/dark-subtracted .dat file reads rather than the FITS file from the camera to form a cube. If the .dat files are handy along with up-to-date dark frames, this gives significantly cleaner results, with better removal of bias tilt, hot pixels, and cosmic rays. The finished cubes are placed in a subdirectory called DATcubes rather than FITScubes.
- -n to produce a .fits cube containing the raw non-destructive read sequence in the .dat file, stored in the intermediate subdirectory. An example of an output NDR sequence cube file name is `/DATA/INTERMEDIATE/goodstuff/POLLUX_C_529-NDRseq.fits`
- -k causes the pipeline to skip the first read during the count rate slope fitting (in .dat mode only). Useful in cases of severe bias tilt/read anomaly with a moderate number of reads (5-10).

- -t causes the pipeline to use the .dat file to make a series of cubes from the difference of every pair of consecutive reads in a given exposure sequence.
- -b does the same thing as -t except only for the brightest stars, with V mag ¡ 2.0
- -a to indiscriminately process all types of images in the given directory rather than just Core (C), Occulted (O), and Other (Ot) images
- -y to process the images without doing a bias/dark-subtraction
- -p to treat the images as already processed, ready for extraction (no bias/dark subtraction, no bad pixel/cosmic ray cleaning, no alignment determination)
- -s to override the shift of the focal plane image with respect to the laser reference determined by the cross-correlation alignment algorithm. After the s option, specify two integers representing the new alignment. For example,

  ```
  $./pipeline ../DATA/goodstuff/ -s 3 -6
  ```

  instructs the program to shift the laser look up table extraction coordinates 3 pixels in x and -6 pixels in y, as opposed to using values determined by the cross-correlation algorithm. If no integers are given following the s term, the alignment defaults to 0,0.
- -a to change the anchor point in the focal plane used by the cross-correlation alignment algorithm. This is useful when there are sources of interest in the image at wide separation from the target star. To specify the new anchor point, enter two integers giving the x and y cube coordinates.
- -l to turn off the localized background subtraction in the cube extraction algorithm. By default the localized background subtraction is on. This subtracts the a median of the dark pixels around each lenslets spectrum before forming the cube value

These switches can be combined, so for example, the user can run

```
$./pipeline ../DATA/goodstuff/ -do
```

or

```
$./pipeline ../DATA/goodstuff/ -yold
```

A.2.4 Procedure Summary for Running the Cube Extraction Pipeline

1. Transfer the .fits focal plane files you want to process (e.g. `HD172648_O_127.fits`) to some directory on the Data Processing workstation (e.g. `/DATA/goodstuff/`).

2. In an xterm window, change to the pipeline directory (`~/proj1640pipe-2010april`).

3. At the command line, execute `$./pipeline /DATA/goodstuff/`

4. After the pipeline indicates the processing is complete, open the result in a ds9 window.

A.2.5 Post Processing

This is a guide to making measurements from the data cubes produced by the extraction pipeline.

A.2.5.1 Spectrum Extraction

Although the extraction pipeline produces data cubes whose fluxes are scaled to compensate for the wavelength-dependent throughput of the atmosphere and instrument, these channel scale factors are based on one epoch of one reference source (currently, the IRTF reference star HD 75555, observed 2009 Dec 3). To obtain a more accurate spectral calibration, the analyst should use reference star data obtained at a time as close as possible to that of the science object of interest.

Suppose you want to measure the spectrum of an object that appears in science image StarA, and you have found good a reference source, StarB (an unsaturated core image of a star with established spectral type, J and H photometry, and ideally an established near-infrared spectrum) acquired during the same night or observing run. Gather the relevant cubes that have NOT had the extraction pipelines built-in spectral calibration applied (these are easily identified by file names that do not end in "`_speccal.fits`"). For the StarA cubes, carry out whatever alignment and co-adding is necessary to maximize the photometric signal of the object of interest.

Now, choose a photometric aperture and background annulus. Keep in mind the PSF expands with wavelength. One approach is to use two aperture sizes: one for J band (corresponding to channels 2-9 out of 23) and another for H band (channels 13-22). For a source of interest with a large amount of contaminating light from a nearby star (such as Alcors companion), it is best to use a small aperture that just fits around the core of the PSF (3 pixels radius in J, 4 pixels radius in H). Determine the annulus-subtracted aperture counts for the 23 channels of StarA and StarB.

The combined response of the spectrograph and extraction pipeline to a monochromatic source has been measured based on extractions of the tunable laser data. These results are plotted in Figure 2.12. Whatever high-resolution near-infrared spectrum is assumed for the reference source should be binned to the cube channel spacing and convolved by these two responses (one for J and one for H band) before comparing it with the result in a P1640 data cube. After binning and filtering the assumed reference spectrum, derive the array of channel-wise flux correction factors needed to make the array of photometric counts from the StarB cube match the established spectrum. Apply the same correction factors to the raw spectrum of StarA to determine the calibrated spectrum.

Bibliography

Aime, C. & Soummer, R. 2004, ApJ, 612, L85

Alonso, R., Brown, T. M., Torres, G., Latham, D. W., Sozzetti, A., Mandushev, G., Belmonte, J. A., Charbonneau, D., Deeg, H. J., Dunham, E. W., O'Donovan, F. T., & Stefanik, R. P. 2004, ApJ, 613, L153

Angel, J. R. P. & Woolf, N. J. 1997, ApJ, 475, 373

Ardila, D. R., Golimowski, D. A., Krist, J. E., Clampin, M., Williams, J. P., Blakeslee, J. P., Ford, H. C., Hartig, G. F., & Illingworth, G. D. 2004, ApJ, 617, L147

Bacon, R., Adam, G., Baranne, A., Courtes, G., Dubet, D., Dubois, J. P., Emsellem, E., Ferruit, P., Georgelin, Y., Monnet, G., Pecontal, E., Rousset, A., & Say, F. 1995, A&AS, 113, 347

Bacon, R., Adam, G., Baranne, A., Courtès, G., Dubet, D., Dubois, J.-P., Georgelin, Y., Monnet, G., Pecontal, E., & Urios, J. 1988, in European Southern Observatory Conference and Workshop Proceedings, Vol. 30, European Southern Observatory Conference and Workshop Proceedings, ed. M.-H. Ulrich, 1185–+

Bakos, G. Á., Noyes, R. W., Kovács, G., Latham, D. W., Torres, G., Sasselov, D., Pál, A., Sipőcz, B., & Kovács, G. 2009, in IAU Symposium, Vol. 253, IAU Symposium, 21–27

Baldwin, J. E., Haniff, C. A., Mackay, C. D., & Warner, P. J. 1986, Nature, 320, 595

Baraffe, I. & Chabrier, G. 1996, ApJ, 461, L51+

Baraffe, I., Chabrier, G., Allard, F., & Hauschildt, P. H. 1998, A&A, 337, 403

Baraffe, I., Chabrier, G., Barman, T. S., Allard, F., & Hauschildt, P. H. 2003, A&A, 402, 701

Beichman, C. A., Krist, J., Trauger, J. T., Greene, T., Oppenheimer, B., Sivaramakrishnan, A., Doyon, R., Boccaletti, A., Barman, T. S., & Rieke, M. 2010, PASP, 122, 162

Bernat, D., Bouchez, A. H., Ireland, M., Tuthill, P., Martinache, F., Angione, J., Burruss, R. S., Cromer, J. L., Dekany, R. G., Guiwits, S. R., Henning, J. R., Hickey, J., Kibblewhite, E., McKenna, D. L., Moore, A. M., Petrie, H. L., Roberts, J., Shelton, J. C., Thicksten, R. P., Trinh, T., Tripathi, R., Troy, M., Truong, T., Velur, V., & Lloyd, J. P. 2010, ApJ, 715, 724

Beuzit, J.-L., Feldt, M., Dohlen, K., Mouillet, D., Puget, P., Wildi, F., Abe, L., Antichi, J., Baruffolo, A., Baudoz, P., Boccaletti, A., Carbillet, M., Charton, J., Claudi, R., Downing, M., Fabron, C., Feautrier, P., Fedrigo, E., Fusco, T., Gach, J.-L., Gratton, R., Henning, T., Hubin, N., Joos, F., Kasper, M., Langlois, M., Lenzen, R., Moutou, C., Pavlov, A., Petit, C., Pragt, J., Rabou, P., Rigal, F., Roelfsema, R., Rousset, G., Saisse, M., Schmid, H.-M., Stadler, E., Thalmann, C., Turatto, M., Udry, S., Vakili, F., & Waters, R. 2008, in Society of Photo-Optical Instrumentation Engineers (SPIE) Conference Series, Vol. 7014, Society of Photo-Optical Instrumentation Engineers (SPIE) Conference Series

Blackstock, D. T. 2000, Fundamentals of Physical Acoustics (John Wiley & Sons, Inc.)

Blandford, S., e. a. 2010, New Worlds, New Horizons in Astronomy and Astrophysics

Bohigian, G. M. 2008, Survey of Ophthalmology, 53, 536

Born, M. & Wolf, E. 1980, Principles of Optics (Pergamon Press)

Borucki, W. J., Koch, D. G., Basri, G., Batalha, N., Boss, A., Brown, T. M., Caldwell, D., Christensen-Dalsgaard, J., Cochran, W. D., DeVore, E., Dunham, E. W., Dupree, A. K., Gautier, III, T. N., Geary, J. C., Gilliland, R., Gould, A., Howell, S. B., Jenkins, J. M., Kjeldsen, H., Latham, D. W., Lissauer, J. J., Marcy, G. W., Monet, D. G., Sasselov, D., Tarter, J., Charbonneau, D., Doyle, L., Ford, E. B., Fortney, J., Holman, M. J., Seager, S., Steffen, J. H., Welsh, W. F., Allen, C., Bryson, S. T., Buchhave, L., Chandrasekaran, H., Christiansen, J. L., Ciardi, D., Clarke, B. D., Dotson, J. L., Endl, M., Fischer, D., Fressin, F., Haas, M., Horch, E., Howard, A., Isaacson, H., Kolodziejczak, J., Li, J., MacQueen, P., Meibom, S., Prsa, A., Quintana, E. V., Rowe, J., Sherry, W., Tenenbaum, P., Torres, G., Twicken, J. D., Van Cleve, J., Walkowicz, L., & Wu, H. 2011, ApJ, 728, 117

Bouchez, A. H., Dekany, R. G., Angione, J. R., Baranec, C., Bui, K., Burruss, R. S., Crepp, J. R., Croner, E. E., Cromer, J. L., Guiwits, S. R., Hale, D. D. S., Henning, J. R., Palmer, D., Roberts, J. E., Troy, M., Truong, T. N., & Zolkower, J. 2009, in Society of Photo-Optical Instrumentation Engineers (SPIE) Conference Series, Vol. 7439, Society of Photo-Optical Instrumentation Engineers (SPIE) Conference Series

Bracewell, R. N. 2006, Fourier Analysis and Imaging (Springer)

Brown, M. G. 2007, PhD thesis, University of Michigan

Bruntt, H., Kervella, P., Mérand, A., Brandão, I. M., Bedding, T. R., Ten Brummelaar, T. A., Coudé Du Foresto, V., Cunha, M. S., Farrington, C., Goldfinger, P. J., Kiss, L. L., McAlister, H. A., Ridgway, S. T., Sturmann, J., Sturmann, L., Turner, N., & Tuthill, P. G. 2010, A&A, 512, A55+

Burrows, A., Marley, M., Hubbard, W. B., Sudarsky, D., Sharp, C., Lunine, J. I., Guillot, T., Saumon, D., & Freedman, R. 1998, in Astronomical Society of the Pacific Conference Series, Vol. 154, Cool Stars, Stellar Systems, and the Sun, ed. R. A. Donahue & J. A. Bookbinder, 27–+

Burrows, A., Saumon, D., Guillot, T., Hubbard, W. B., & Lunine, J. I. 1995, Nature, 375, 299

Caldwell, D. A., van Cleve, J. E., Jenkins, J. M., Argabright, V. S., Kolodziejczak, J. J., Dunham, E. W., Geary, J. C., Tenenbaum, P., Chandrasekaran, H., Li, J., Wu, H., & von Wilpert, J. 2010, in Society of Photo-Optical Instrumentation Engineers (SPIE) Conference Series, Vol. 7731, Society of Photo-Optical Instrumentation Engineers (SPIE) Conference Series

Campbell, W. W. & Moore, J. H. 1907, Lick Observatory Bulletin, 4, 161

Castellani, V., Degl'Innocenti, S., Prada Moroni, P. G., & Tordiglione, V. 2002, MNRAS, 334, 193

Charbonneau, D., Brown, T. M., Noyes, R. W., & Gilliland, R. L. 2002, ApJ, 568, 377

Chauvin, G., Lagrange, A.-M., Bonavita, M., Zuckerman, B., Dumas, C., Bessell, M. S., Beuzit, J.-L., Bonnefoy, M., Desidera, S., Farihi, J., Lowrance, P., Mouillet, D., & Song, I. 2010a, A&A, 509, A52+

—. 2010b, A&A, 509, A52+

Colavita, M. M., Boden, A. F., Crawford, S. L., Meinel, A. B., Shao, M., Swanson, P. N., van Belle, G. T., Vasisht, G., Walker, J. M., Wallace, J. K., & Wizinowich, P. L. 1998, in Society of Photo-Optical Instrumentation Engineers (SPIE) Conference Series, Vol. 3350, Society of Photo-Optical Instrumentation Engineers (SPIE) Conference Series, ed. R. D. Reasenberg, 776–784

Colavita, M. M., Serabyn, E., Millan-Gabet, R., Koresko, C. D., Akeson, R. L., Booth, A. J., Mennesson, B. P., Ragland, S. D., Appleby, E. C., Berkey, B. C., Cooper, A., Crawford, S. L., Creech-Eakman, M. J., Dahl, W., Felizardo, C., Garcia-Gathright, J. I., Gathright, J. T., Herstein, J. S., Hovland, E. E., Hrynevych, M. A., Ligon, E. R., Medeiros, D. W., Moore, J. D., Morrison, D., Paine, C. G., Palmer, D. L., Panteleeva, T., Smith, B., Swain, M. R., Smythe, R. F., Summers, K. R., Tsubota, K., Tyau, C., Vasisht, G., Wetherell, E., Wizinowich, P. L., & Woillez, J. M. 2009, PASP, 121, 1120

Collier Cameron, A., Pollacco, D., Hellier, C., West, R., WASP Consortium, & SOPHIE & CORALIE Planet-Search Teams. 2009, in IAU Symposium, Vol. 253, IAU Symposium, 29–35

Crepp, J. R. & Johnson, J. A. 2011, ApJ, 733, 126

Crepp, J. R., Pueyo, L., Brenner, D., Oppenheimer, B. R., Zimmerman, N., Hinkley, S., Parry, I., King, D., Vasisht, G., Beichman, C., Hillenbrand, L., Dekany, R., Shao, M., Burruss, R., Roberts, L. C., Bouchez, A., Roberts, J., & Soummer, R. 2011, ApJ, 729, 132

Cutri, R. M., Skrutskie, M. F., van Dyk, S., Beichman, C. A., Carpenter, J. M., Chester, T., Cambresy, L., Evans, T., Fowler, J., Gizis, J., Howard, E., Huchra, J., Jarrett, T., Kopan, E. L., Kirkpatrick, J. D., Light, R. M., Marsh, K. A., McCallon, H., Schneider, S., Stiening, R., Sykes, M., Weinberg, M., Wheaton, W. A., Wheelock, S., & Zacarias, N. 2003, 2MASS All Sky Catalog of point sources.

de Rosa, R. J., Bulger, J., Patience, J., Leland, B., Macintosh, B., Schneider, A., Song, I., Marois, C., Graham, J. R., Bessell, M., & Doyon, R. 2011, MNRAS, 415, 854

Dean, R. B. & Dixon, W. J. 1951, Anal. Chem., 23, 636

Dekany, R. G., Wallace, J. K., Brack, G., Oppenheimer, B. R., & Palmer, D. 1997, in Society of Photo-Optical Instrumentation Engineers (SPIE) Conference Series, Vol. 3126, Society of Photo-Optical Instrumentation Engineers (SPIE) Conference Series, ed. R. K. Tyson & R. Q. Fugate, 269–+

Ehrenreich, D., Lagrange, A.-M., Montagnier, G., Chauvin, G., Galland, F., Beuzit, J.-L., & Rameau, J. 2010, A&A, 523, A73+

Fedele, U. 1949, Coelum, 17, 65

Fink, U. & Larson, H. P. 1979, ApJ, 233, 1021

Galilei, G. 1632, Dialogo sopra i due massimi sistemi del mondo (Dialogue concerning the two chief world systems), English translation by Stillman Drake published in 1967

Gaudi, B. S. 2010, ArXiv e-prints

Goodman, J. W. 1996, Introduction to Fourier optics (McGraw-Hill)

Gould, A. & Loeb, A. 1992, ApJ, 396, 104

Gray, R. O., Graham, P. W., & Hoyt, S. R. 2001, AJ, 121, 2159

Griffith, C. A., Owen, T., Miller, G. A., & Geballe, T. 1998, Nature, 395, 575

Griffith, C. A., Owen, T., & Wagener, R. 1991, Icarus, 93, 362

Guyon, O. 2009, in American Institute of Physics Conference Series, Vol. 1158, American Institute of Physics Conference Series, ed. T. Usuda, M. Tamura, & M. Ishii, 285–292

Haniff, C. A., Mackay, C. D., Titterington, D. J., Sivia, D., & Baldwin, J. E. 1987, Nature, 328, 694

Hansen, B. M. S., Shih, H.-Y., & Currie, T. 2009, ApJ, 691, 382

Hardy, J. W. 1978, IEEE Proceedings, 66, 651

Hartkopf, W. I., Mason, B. D., & Worley, C. E. 2001, AJ, 122, 3472

Hartung, M., Blanc, A., Fusco, T., Lacombe, F., Mugnier, L. M., Rousset, G., & Lenzen, R. 2003, A&A, 399, 385

Henry, T. J. & McCarthy, Jr., D. W. 1993, AJ, 106, 773

Hinkley, S., Carpenter, J. M., Ireland, M. J., & Kraus, A. L. 2011a, ApJ, 730, L21+

Hinkley, S., Oppenheimer, B. R., Brenner, D., Zimmerman, N., Roberts, L. C., Parry, I. R., Soummer, R., Sivaramakrishnan, A., Simon, M., Perrin, M. D., King, D. L., Lloyd, J. P., Bouchez, A., Roberts, J. E., Dekany, R., Beichman, C., Hillenbrand, L., Burruss, R., Shao, M., & Vasisht, G. 2010, ApJ, 712, 421

Hinkley, S., Oppenheimer, B. R., Soummer, R., Sivaramakrishnan, A., Roberts, Jr., L. C., Kuhn, J., Makidon, R. B., Perrin, M. D., Lloyd, J. P., Kratter, K., & Brenner, D. 2007, ApJ, 654, 633

Hinkley, S., Oppenheimer, B. R., Zimmerman, N., Brenner, D., Parry, I. R., Crepp, J. R., Vasisht, G., Ligon, E., King, D., Soummer, R., Sivaramakrishnan, A., Beichman, C., Shao, M., Roberts, L. C., Bouchez, A., Dekany, R., Pueyo, L., Roberts, J. E., Lockhart, T., Zhai, C., Shelton, C., & Burruss, R. 2011b, PASP, 123, 74

Hinz, P. M., Angel, J. R. P., Hoffmann, W. F., McCarthy, D. W., McGuire, P. C., Cheselka, M., Hora, J. L., & Woolf, N. J. 1998, Nature, 395, 251

Holman, M. J., Fabrycky, D. C., Ragozzine, D., Ford, E. B., Steffen, J. H., Welsh, W. F., Lissauer, J. J., Latham, D. W., Marcy, G. W., Walkowicz, L. M., Batalha, N. M., Jenkins, J. M., Rowe, J. F., Cochran, W. D., Fressin, F., Torres, G., Buchhave, L. A., Sasselov, D. D., Borucki, W. J., Koch, D. G., Basri, G., Brown, T. M., Caldwell, D. A., Charbonneau, D., Dunham, E. W., Gautier, T. N., Geary, J. C., Gilliland, R. L., Haas, M. R., Howell, S. B., Ciardi, D. R., Endl, M., Fischer, D., Fürész, G., Hartman, J. D., Isaacson, H., Johnson, J. A., MacQueen, P. J., Moorhead, A. V., Morehead, R. C., & Orosz, J. A. 2010, Science, 330, 51

Horne, K. 1986, PASP, 98, 609

Howard, A. W., Marcy, G. W., Johnson, J. A., Fischer, D. A., Wright, J. T., Isaacson, H., Valenti, J. A., Anderson, J., Lin, D. N. C., & Ida, S. 2010, Science, 330, 653

Huerta, M., Johns-Krull, C. M., Prato, L., Hartigan, P., & Jaffe, D. T. 2008, ApJ, 678, 472

Ireland, M. J., Kraus, A., Martinache, F., Lloyd, J. P., & Tuthill, P. G. 2008, ApJ, 678, 463

Ireland, M. J., Monnier, J. D., & Thureau, N. 2006, in Society of Photo-Optical Instrumentation Engineers (SPIE) Conference Series, Vol. 6268, Society of Photo-Optical Instrumentation Engineers (SPIE) Conference Series

Ireland, M. J., Monnier, J. D., Tuthill, P. G., Cohen, R. W., De Buizer, J. M., Packham, C., Ciardi, D., Hayward, T., & Lloyd, J. P. 2007, ApJ, 662, 651

Ives, D. 2008, Threshold Limited NDR Algorithm, UK Astronomical Technology Centre Technical Memo

Janson, M., Brandner, W., & Henning, T. 2008, A&A, 478, 597

Jennison, R. C. 1958, MNRAS, 118, 276

Johnson, D. R. H. & Soderblom, D. R. 1987, AJ, 93, 864

Johnson, J. A., Aller, K. M., Howard, A. W., & Crepp, J. R. 2010, PASP, 122, 905

Johnson, J. A., Marcy, G. W., Fischer, D. A., Wright, J. T., Reffert, S., Kregenow, J. M., Williams, P. K. G., & Peek, K. M. G. 2008, ApJ, 675, 784

Kalas, P., Graham, J. R., Chiang, E., Fitzgerald, M. P., Clampin, M., Kite, E. S., Stapelfeldt, K., Marois, C., & Krist, J. 2008, Science, 322, 1345

King, J. R., Villarreal, A. R., Soderblom, D. R., Gulliver, A. F., & Adelman, S. J. 2003, AJ, 125, 1980

Klein, M. V. 1970, Optics (John Wiley & Sons, Inc.)

Knutson, H. A., Charbonneau, D., Allen, L. E., Burrows, A., & Megeath, S. T. 2008, ApJ, 673, 526

Kochanek, C. S. 1996, ApJ, 457, 228

Kouwenhoven, M. B. N., Brown, A. G. A., Zinnecker, H., Kaper, L., & Portegies Zwart, S. F. 2005, A&A, 430, 137

Kratter, K. M., Murray-Clay, R. A., & Youdin, A. N. 2010, ApJ, 710, 1375

Kraus, A. L., Ireland, M. J., Martinache, F., & Lloyd, J. P. 2008, ApJ, 679, 762

Krist, J. E. 2007, in Society of Photo-Optical Instrumentation Engineers (SPIE) Conference Series, Vol. 6675, Society of Photo-Optical Instrumentation Engineers (SPIE) Conference Series

Lafrenière, D., Doyon, R., Marois, C., Nadeau, D., Oppenheimer, B. R., Roche, P. F., Rigaut, F., Graham, J. R., Jayawardhana, R., Johnstone, D., Kalas, P. G., Macintosh, B., & Racine, R. 2007, ApJ, 670, 1367

Larkin, J., Barczys, M., Krabbe, A., Adkins, S., Aliado, T., Amico, P., Brims, G., Campbell, R., Canfield, J., Gasaway, T., Honey, A., Iserlohe, C., Johnson, C., Kress, E., LaFreniere, D., Lyke, J., Magnone, K., Magnone, N., McElwain, M., Moon, J., Quirrenbach, A., Skulason, G., Song, I., Spencer, M., Weiss, J., & Wright, S. 2006, in Society of Photo-Optical Instrumentation Engineers (SPIE) Conference Series, Vol. 6269, Society of Photo-Optical Instrumentation Engineers (SPIE) Conference Series

Launhardt, R., Queloz, D., Henning, T., Quirrenbach, A., Delplancke, F., Andolfato, L., Baumeister, H., Bizenberger, P., Bleuler, H., Chazelas, B., Dérie, F., Di Lieto, L., Duc, T. P., Duvanel, O., Elias, II, N. M., Fluery, M., Geisler, R., Gillet, D., Graser, U., Koch, F., Köhler, R., Maire, C., Mégevand, D., Michellod, Y., Moresmau, J., Müller, A., Müllhaupt, P., Naranjo, V., Pepe, F., Reffert, S., Sache, L., Ségransan, D., Salvadé, Y., Schulze-Hartung, T., Setiawan, J., Simond, G., Sosnowska, D., Stilz, I., Tubbs, B., Wagner, K., Weber, L., Weise, P., & Zago, L. 2008, in Presented at the Society of Photo-Optical Instrumentation Engineers (SPIE) Conference, Vol. 7013, Society of Photo-Optical Instrumentation Engineers (SPIE) Conference Series

Lawson, P. R., Lay, O. P., Martin, S. R., Beichman, C. A., Johnston, K. J., Danchi, W. C., Gappinger, R. O., Hunyadi, S. L., Ksendzov, A., Mennesson, B., Peters, R. D., Scharf, D. P., Serabyn, E., & Unwin, S. C. 2007, in Society of Photo-Optical Instrumentation Engineers (SPIE) Conference Series, Vol. 6693, Society of Photo-Optical Instrumentation Engineers (SPIE) Conference Series

Leconte, J., Soummer, R., Hinkley, S., Oppenheimer, B. R., Sivaramakrishnan, A., Brenner, D., Kuhn, J., Lloyd, J. P., Perrin, M. D., Makidon, R., Roberts, Jr., L. C., Graham, J. R., Simon, M., Brown, R. A., Zimmerman, N., Chabrier, G., & Baraffe, I. 2010, ApJ, 716, 1551

Léger, A., Mariotti, J. M., Mennesson, B., Ollivier, M., Puget, J. L., Rouan, D., & Schneider, J. 1996, Ap&SS, 241, 135

Lemmon, M. T., Karkoschka, E., & Tomasko, M. 1995, Icarus, 113, 27

Lindegren, L. 2010, in IAU Symposium, Vol. 261, IAU Symposium, ed. S. A. Klioner, P. K. Seidelmann, & M. H. Soffel, 296–305

Liu, M. C., Wahhaj, Z., Biller, B. A., Nielsen, E. L., Chun, M., Close, L. M., Ftaclas, C., Hartung, M., Hayward, T. L., Clarke, F., Reid, I. N., Shkolnik, E. L., Tecza, M., Thatte, N., Alencar, S., Artymowicz, P., Boss, A., Burrows, A., de Gouveia Dal Pino, E., Gregorio-Hetem, J., Ida, S., Kuchner, M. J., Lin, D., & Toomey, D. 2010, in Society of Photo-Optical Instrumentation Engineers (SPIE) Conference Series, Vol. 7736, Society of Photo-Optical Instrumentation Engineers (SPIE) Conference Series

Lloyd, J. P., Martinache, F., Ireland, M. J., Monnier, J. D., Pravdo, S. H., Shaklan, S. B., & Tuthill, P. G. 2006, ApJ, 650, L131

Lyon, R. G., Clampin, M., Woodruff, R. A., Vasudevan, G., Thompson, P., Chen, A., Petrone, P., Booth, A., Madison, T., Bolcar, M., Noecker, M. C., Kendrick, S., Melnick, G., & Tolls, V. 2010, in Society of Photo-Optical Instrumentation Engineers (SPIE) Conference Series, Vol. 7731, Society of Photo-Optical Instrumentation Engineers (SPIE) Conference Series

Lyot, B. 1939, MNRAS, 99, 580

Macintosh, B., Graham, J., Palmer, D., Doyon, R., Gavel, D., Larkin, J., Oppenheimer, B., Saddlemyer, L., Wallace, J. K., Bauman, B., Evans, J., Erikson, D., Morzinski, K., Phillion, D., Poyneer, L., Sivaramakrishnan, A., Soummer, R., Thibault, S., & Veran, J.-P. 2006, in Society of Photo-Optical Instrumentation Engineers (SPIE) Conference Series, Vol. 6272, Society of Photo-Optical Instrumentation Engineers (SPIE) Conference Series

Macintosh, B. A., Graham, J. R., Palmer, D. W., Doyon, R., Dunn, J., Gavel, D. T., Larkin, J., Oppenheimer, B., Saddlemyer, L., Sivaramakrishnan, A., Wallace, J. K., Bauman, B., Erickson, D. A., Marois, C., Poyneer, L. A., & Soummer, R. 2008, in Presented at the Society of Photo-Optical Instrumentation Engineers (SPIE) Conference, Vol. 7015, Society of Photo-Optical Instrumentation Engineers (SPIE) Conference Series

Maire, J., Perrin, M. D., Doyon, R., Artigau, E., Dunn, J., Gavel, D. T., Graham, J. R., Lafrenière, D., Larkin, J. E., Lavigne, J.-F., Macintosh, B. A., Marois, C., Oppenheimer, B., Palmer, D. W., Poyneer, L. A., Thibault, S., & Véran, J.-P. 2010, in Society of Photo-Optical Instrumentation Engineers (SPIE) Conference Series, Vol. 7735, Society of Photo-Optical Instrumentation Engineers (SPIE) Conference Series

Makarov, V. V., Beichman, C. A., Catanzarite, J. H., Fischer, D. A., Lebreton, J., Malbet, F., & Shao, M. 2009, ApJ, 707, L73

Malkov, O. Y. 2007, MNRAS, 382, 1073

Mamajek, E. E., Kenworthy, M. A., Hinz, P. M., & Meyer, M. R. 2010, AJ, 139, 919

Manduca, A. & Bell, R. A. 1979, PASP, 91, 848

Markwardt, C. B. 2009, in Astronomical Society of the Pacific Conference Series, Vol. 411, Astronomical Data Analysis Software and Systems XVIII, ed. D. A. Bohlender, D. Durand, & P. Dowler, 251–+

Marois, C., Doyon, R., Nadeau, D., Racine, R., Riopel, M., Vallée, P., & Lafrenière, D. 2005, PASP, 117, 745

Marois, C., Lafrenière, D., Doyon, R., Macintosh, B., & Nadeau, D. 2006a, ApJ, 641, 556

Marois, C., Lafrenière, D., Macintosh, B., & Doyon, R. 2006b, ApJ, 647, 612

Marois, C., Macintosh, B., Barman, T., Zuckerman, B., Song, I., Patience, J., Lafrenière, D., & Doyon, R. 2008a, Science, 322, 1348

—. 2008b, Science, 322, 1348

Marois, C., Zuckerman, B., Konopacky, Q. M., Macintosh, B., & Barman, T. 2010, Nature, 468, 1080

Martinache, F., Rojas-Ayala, B., Ireland, M. J., Lloyd, J. P., & Tuthill, P. G. 2009, ApJ, 695, 1183

McAlister, H. A., Mason, B. D., Hartkopf, W. I., & Shara, M. M. 1993, AJ, 106, 1639

McCarthy, Jr., D. W., Probst, R. G., & Low, F. J. 1985, ApJ, 290, L9

McElwain, M. W., e. a. 2008, An IFS for the Subaru Observatory HiCIAO system, SPIE Astronomical Instrumentation conference poster

McElwain, M. W., Metchev, S. A., Larkin, J. E., Barczys, M., Iserlohe, C., Krabbe, A., Quirrenbach, A., Weiss, J., & Wright, S. A. 2007, ApJ, 656, 505

Meschiari, S., Laughlin, G., Vogt, S. S., Butler, R. P., Rivera, E. J., Haghighipour, N., & Jalowiczor, P. 2011, ApJ, 727, 117

Metchev, S. A. & Hillenbrand, L. A. 2009, ApJS, 181, 62

Metchev, S. A., Hillenbrand, L. A., & Meyer, M. R. 2004, ApJ, 600, 435

Meyer, M. R., Hillenbrand, L. A., Backman, D., Beckwith, S., Bouwman, J., Brooke, T., Carpenter, J., Cohen, M., Cortes, S., Crockett, N., Gorti, U., Henning, T., Hines, D., Hollenbach, D., Kim, J. S., Lunine, J., Malhotra, R., Mamajek, E., Metchev, S., Moro-Martin, A., Morris, P., Najita, J., Padgett, D., Pascucci, I., Rodmann, J., Schlingman, W., Silverstone, M., Soderblom, D., Stauffer, J., Stobie, E., Strom, S., Watson, D., Weidenschilling, S., Wolf, S., & Young, E. 2006, PASP, 118, 1690

Miskey, C. L. & Bruhweiler, F. C. 2003, AJ, 125, 3071

Monnier, J. D., Tuthill, P. G., & Danchi, W. C. 1999, ApJ, 525, L97

Morales, F. Y., Werner, M. W., Bryden, G., Plavchan, P., Stapelfeldt, K. R., Rieke, G. H., Su, K. Y. L., Beichman, C. A., Chen, C. H., Grogan, K., Kenyon, S. J., Moro-Martin, A., & Wolf, S. 2009, ApJ, 699, 1067

Mugrauer, M. & Neuhäuser, R. 2005, Astronomische Nachrichten, 326, 701

Muterspaugh, M. W., Hartkopf, W. I., Lane, B. F., O'Connell, J., Williamson, M., Kulkarni, S. R., Konacki, M., Burke, B. F., Colavita, M. M., Shao, M., & Wiktorowicz, S. J. 2010, AJ, 140, 1623

Muterspaugh, M. W., Lane, B. F., Konacki, M., Burke, B. F., Colavita, M. M., Kulkarni, S. R., & Shao, M. 2006, in Society of Photo-Optical Instrumentation Engineers (SPIE) Conference Series, Vol. 6268, Society of Photo-Optical Instrumentation Engineers (SPIE) Conference Series

Nakajima, T., Oppenheimer, B. R., Kulkarni, S. R., Golimowski, D. A., Matthews, K., & Durrance, S. T. 1995, Nature, 378, 463

Nesvorný, D. & Morbidelli, A. 2008, ApJ, 688, 636

Neuhäuser, R., Mugrauer, M., Seifahrt, A., Schmidt, T. O. B., & Vogt, N. 2008, A&A, 484, 281

Oetken, L. & Orwert, R. 1984, Astronomische Nachrichten, 305, 317

Offenberg, J. D., Fixsen, D. J., Rauscher, B. J., Forrest, W. J., Hanisch, R. J., Mather, J. C., McKelvey, M. E., McMurray, Jr., R. E., Nieto-Santisteban, M. A., Pipher, J. L., Sengupta, R., & Stockman, H. S. 2001, PASP, 113, 240

Oppenheimer, B. R. & Hinkley, S. 2009, ARA&A, 47, 253

Oppenheimer, B. R., Kulkarni, S. R., Matthews, K., & Nakajima, T. 1995, Science, 270, 1478

Oppenheimer, B. R., Kulkarni, S. R., & Stauffer, J. R. 2000, Protostars and Planets IV, 1313

Oppenheimer, B. R., Sivaramakrishnan, A., & Makidon, R. B. 2003, in Astrophysics and Space Science Library, Vol. 289, Astrophysics and Space Science Library, ed. T. D. Oswalt, 155–+

Pallavicini, R. 1989, A&A Rev., 1, 177

Patience, J., Macintosh, B. A., & Max, C. E. 2001, in Society of Photo-Optical Instrumentation Engineers (SPIE) Conference Series, Vol. 4490, Society of Photo-Optical Instrumentation Engineers (SPIE) Conference Series, ed. A. R. Pirich, P. L. Repak, P. S. Idell, & S. R. Czyzak, 178–186

Pepe, F., Mayor, M., Rupprecht, G., Avila, G., Ballester, P., Beckers, J.-L., Benz, W., Bertaux, J.-L., Bouchy, F., Buzzoni, B., Cavadore, C., Deiries, S., Dekker, H., Delabre, B., D'Odorico, S., Eckert, W., Fischer, J., Fleury, M., George, M., Gilliotte, A., Gojak, D., Guzman, J.-C., Koch, F., Kohler, D., Kotzlowski, H., Lacroix, D., Le Merrer, J., Lizon, J.-L., Lo Curto, G., Longinotti, A., Megevand, D., Pasquini, L., Petitpas, P., Pichard, M., Queloz, D., Reyes, J., Richaud, P., Sivan, J.-P., Sosnowska, D., Soto, R., Udry, S., Ureta, E., van Kesteren, A., Weber, L., Weilenmann, U., Wicenec, A., Wieland, G., Christensen-Dalsgaard, J., Dravins, D., Hatzes, A., Kürster, M., Paresce, F., & Penny, A. 2002, The Messenger, 110, 9

Perrier, C. & Mariotti, J.-M. 1987, ApJ, 312, L27

Perrin, M. D., Sivaramakrishnan, A., Makidon, R. B., Oppenheimer, B. R., & Graham, J. R. 2003, ApJ, 596, 702

Perryman, M. A. C., Lindegren, L., Kovalevsky, J., Hoeg, E., Bastian, U., Bernacca, P. L., Crézé, M., Donati, F., Grenon, M., van Leeuwen, F., van der Marel, H., Mignard, F., Murray, C. A., Le Poole, R. S., Schrijver, H., Turon, C., Arenou, F., Froeschlé, M., & Petersen, C. S. 1997, A&A, 323, L49

Phinney, E. S. & Hansen, B. M. S. 1993, in Astronomical Society of the Pacific Conference Series, Vol. 36, Planets Around Pulsars, ed. J. A. Phillips, S. E. Thorsett, & S. R. Kulkarni, 371–390

Pickles, A. J. 1998, PASP, 110, 863

Podsiadlowski, P. 1993, in Astronomical Society of the Pacific Conference Series, Vol. 36, Planets Around Pulsars, ed. J. A. Phillips, S. E. Thorsett, & S. R. Kulkarni, 149–165

Prato, L., Huerta, M., Johns-Krull, C. M., Mahmud, N., Jaffe, D. T., & Hartigan, P. 2008, ApJ, 687, L103

Pravdo, S. H., Shaklan, S. B., Wiktorowicz, S. J., Kulkarni, S., Lloyd, J. P., Martinache, F., Tuthill, P. G., & Ireland, M. J. 2006, ApJ, 649, 389

Pueyo, L. e. a. 2011, ApJ, in prep.

Racine, R., Walker, G. A. H., Nadeau, D., Doyon, R., & Marois, C. 1999, PASP, 111, 587

Rayner, J. T., Cushing, M. C., & Vacca, W. D. 2009, ApJS, 185, 289

Rayner, J. T., Toomey, D. W., Onaka, P. M., Denault, A. J., Stahlberger, W. E., Vacca, W. D., Cushing, M. C., & Wang, S. 2003, PASP, 115, 362

Readhead, A. C. S., Nakajima, T. S., Pearson, T. J., Neugebauer, G., Oke, J. B., & Sargent, W. L. W. 1988, AJ, 95, 1278

Saar, S. H. & Donahue, R. A. 1997, ApJ, 485, 319

Sahlmann, J., Lovis, C., Queloz, D., & Ségransan, D. 2011, A&A, 528, L8+

Santos, N. C., Mayor, M., Benz, W., Bouchy, F., Figueira, P., Lo Curto, G., Lovis, C., Melo, C., Moutou, C., Naef, D., Pepe, F., Queloz, D., Sousa, S. G., & Udry, S. 2010, A&A, 512, A47+

Schaller, E. L., Roe, H. G., Schneider, T., & Brown, M. E. 2009, Nature, 460, 873

Scharf, C. A. 2009, Extrasolar Planets and Astrobiology (University Science Books)

Schmitt, J. H. M. M., Golub, L., Harnden, Jr., F. R., Maxson, C. W., Rosner, R., & Vaiana, G. S. 1985, ApJ, 290, 307

Schröder, C. & Schmitt, J. H. M. M. 2007, A&A, 475, 677

Schfer, J. & Strimmer, K. 2005, Statistical Applications in Genetics and Molecular Biology, 4

Shao, M. & Colavita, M. M. 1992, A&A, 262, 353

Siebert, H. 2005, Journal for the History of Astronomy, 36, 251

Sivaramakrishnan, A., Koresko, C. D., Makidon, R. B., Berkefeld, T., & Kuchner, M. J. 2001, ApJ, 552, 397

Sivaramakrishnan, A., Lloyd, J. P., Hodge, P. E., & Macintosh, B. A. 2002, ApJ, 581, L59

Sivaramakrishnan, A. & Oppenheimer, B. R. 2006, ApJ, 647, 620

Sivia, D. S. 2006, Data Analysis: A Bayesian Tutorial (Oxford Science Publications)

Smith, M. C., Ruchti, G. R., Helmi, A., Wyse, R. F. G., Fulbright, J. P., Freeman, K. C., Navarro, J. F., Seabroke, G. M., Steinmetz, M., Williams, M., Bienaymé, O., Binney, J., Bland-Hawthorn, J., Dehnen, W., Gibson, B. K., Gilmore, G., Grebel, E. K., Munari, U., Parker, Q. A., Scholz, R.-D., Siebert, A., Watson, F. G., & Zwitter, T. 2007, MNRAS, 379, 755

Soderblom, D. R. & Mayor, M. 1993, AJ, 105, 226

Sommerfeld, A. 1954, Optics: Lectures on Theoretical Physics, Vol. IV (Academic Press Inc.)

Soummer, R. 2005, ApJ, 618, L161

Soummer, R., Ferrari, A., Aime, C., & Jolissaint, L. 2007, ApJ, 669, 642

Soummer, R., Sivaramakrishnan, A., Oppenheimer, B. R., Roberts, R., Brenner, D., Carlotti, A., Pueyo, L., Macintosh, B., Bauman, B., Saddlemyer, L., Palmer, D., Erickson, D., Dorrer, C., Caputa, K., Marois, C., Wallace, K., Griffiths, E., & Mey, J. 2009, in Society of Photo-Optical Instrumentation Engineers (SPIE) Conference Series, Vol. 7440, Society of Photo-Optical Instrumentation Engineers (SPIE) Conference Series

Sparks, W. B. & Ford, H. C. 2002, ApJ, 578, 543

Spiegel, D. S., Burrows, A., & Milsom, J. A. 2011, ApJ, 727, 57

Stamatellos, D., Hubber, D. A., & Whitworth, A. P. 2007, MNRAS, 382, L30

Stapelfeldt, K. R. 2006, in IAU Symposium, Vol. 232, The Scientific Requirements for Extremely Large Telescopes, ed. P. Whitelock, M. Dennefeld, & B. Leibundgut, 149–158

Sumi, T., Kamiya, K., Bennett, D. P., Bond, I. A., Abe, F., Botzler, C. S., Fukui, A., Furusawa, K., Hearnshaw, J. B., Itow, Y., Kilmartin, P. M., Korpela, A., Lin, W., Ling, C. H., Masuda, K., Matsubara, Y., Miyake, N., Motomura, M., Muraki, Y., Nagaya, M., Nakamura, S., Ohnishi, K., Okumura, T., Perrott, Y. C., Rattenbury, N., Saito, T., Sako, T., Sullivan, D. J., Sweatman, W. L., Tristram, P. J., Udalski, A., Szymański, M. K., Kubiak, M., Pietrzyński, G., Poleski, R., Soszyński, I., Wyrzykowski, Ł., Ulaczyk, K., & Microlensing Observations in Astrophysics (MOA) Collaboration. 2011, Nature, 473, 349

Swain, M. R., Vasisht, G., & Tinetti, G. 2008, Nature, 452, 329

Thalmann, C., Carson, J., Janson, M., Goto, M., McElwain, M., Egner, S., Feldt, M., Hashimoto, J., Hayano, Y., Henning, T., Hodapp, K. W., Kandori, R., Klahr, H., Kudo, T., Kusakabe, N., Mordasini, C., Morino, J.-I., Suto, H., Suzuki, R., & Tamura, M. 2009, ApJ, 707, L123

Thatte, N., Abuter, R., Tecza, M., Nielsen, E. L., Clarke, F. J., & Close, L. M. 2007, MNRAS, 378, 1229

Thies, I., Kroupa, P., Goodwin, S. P., Stamatellos, D., & Whitworth, A. P. 2010, ApJ, 717, 577

Thorne, K. 2004, Applications of Classical Physics

Tokovinin, A. A. 1984, Pis ma Astronomicheskii Zhurnal, 10, 293

Troy, M., Dekany, R. G., Brack, G., Oppenheimer, B. R., Bloemhof, E. E., Trinh, T., Dekens, F. G., Shi, F., Hayward, T. L., & Brandl, B. 2000, in Society of Photo-Optical Instrumentation Engineers (SPIE) Conference Series, Vol. 4007, Society of Photo-Optical Instrumentation Engineers (SPIE) Conference Series, ed. P. L. Wizinowich, 31–40

Tuthill, P., Lloyd, J., Ireland, M., Martinache, F., Monnier, J., Woodruff, H., ten Brummelaar, T., Turner, N., & Townes, C. 2006a, in Society of Photo-Optical Instrumentation Engineers (SPIE) Conference Series, Vol. 6272, Society of Photo-Optical Instrumentation Engineers (SPIE) Conference Series

Tuthill, P., Monnier, J., Tanner, A., Figer, D., Ghez, A., & Danchi, W. 2006b, Science, 313, 935

Tuthill, P. G., Danchi, W. C., Hale, D. S., Monnier, J. D., & Townes, C. H. 2000, ApJ, 534, 907

Udalski, A. 2003, Acta Astron., 53, 291

Udry, S. & Santos, N. C. 2007, ARA&A, 45, 397

Vogt, S. S., Butler, R. P., Rivera, E. J., Haghighipour, N., Henry, G. W., & Williamson, M. H. 2010, ApJ, 723, 954

Wallace, K., Hardy, G., & Serabyn, E. 2000, Nature, 406, 700

Wolszczan, A. 1994, Science, 264, 538

Wolszczan, A. & Frail, D. A. 1992, Nature, 355, 145

Zimmerman, N., Oppenheimer, B. R., Hinkley, S., Brenner, D., Parry, I. R., Sivaramakrishnan, A., Hillenbrand, L., Beichman, C., Crepp, J. R., Vasisht, G., Roberts, L. C., Burruss, R., King, D. L., Soummer, R., Dekany, R., Shao, M., Bouchez, A., Roberts, J. E., & Hunt, S. 2010, ApJ, 709, 733

Zuckerman, B. & Song, I. 2004, ARA&A, 42, 685